3-1-2018

Navigation using Vector and Tensor Measurements of the Earth's Magnetic Anomaly Field

Lauren A. Mount

NAVIGATION USING VECTOR AND TENSOR MEASUREMENTS OF THE EARTH'S MAGNETIC ANOMALY FIELD

THESIS

Lauren A. Mount, Captain, USAF

AFIT-ENG-MS-18-M-049

DEPARTMENT OF THE AIR FORCE
AIR UNIVERSITY

AIR FORCE INSTITUTE OF TECHNOLOGY

Wright-Patterson Air Force Base, Ohio

AFIT-ENG-MS-18-M-049

NAVIGATION USING VECTOR AND TENSOR MEASUREMENTS OF THE EARTH'S MAGNETIC ANOMALY FIELD

THESIS

Presented to the Faculty

Department of Electrical Engineering

Graduate School of Engineering and Management

Air Force Institute of Technology

Air University

Air Education and Training Command

in Partial Fulfillment of the Requirements for the

Degree of Master of Science in Electrical Engineering

Lauren A. Mount, B.S.E.E.

Captain, USAF

March 2018

AFIT-ENG-MS-18-M-049

NAVIGATION USING VECTOR AND TENSOR MEASUREMENTS OF THE EARTH'S MAGNETIC ANOMALY FIELD

THESIS

Lauren A. Mount, B.S.E.E.
Captain, USAF

Committee Membership:

Capt Aaron Canciani, PhD
Chair

Maj Scott Pierce, PhD
Member

Dr. John Raquet
Member

Abstract

This research explores the viability of using a navigation system that relies on measurements of the magnetic anomaly field as an alternative to GPS navigation. Previous research has been conducted on developing a navigation system using the intensity of the Earth's magnetic anomaly field as an alternative signal. This research focuses on using vector and tensor measurements, as opposed to scalar measurements of the anomaly field, as a means of obtaining accurate position and orientation solutions.

This paper presents two navigation systems. The first uses an Extended Kalman Filter (EKF) with vector measurements of the magnetic anomaly field to aid an inertial navigation system (INS), while the second uses tensor measurements.

Simulations examine the performance of both navigation systems in sixteen scenarios. The parameters evaluated in the simulations include the position and velocity of the trajectory, whether vector or tensor measurements are used, the quality of the INS paired with the filter, and the map resolution. Simulations demonstrate that the tensor measurement filter paired with a navigation-grade INS performed best out of the sixteen test cases. For a one-hour ship trajectory, the navigation system was able to demonstrate 35.94 m DRMS error when paired with a navigation-grade INS. The same navigation system was able to obtain navigation accuracies of 38.10 m DRMS when paired with a 10X-grade INS for a 25 hour ship trajectory with a lower resolution magnetic field map due to the depth of the ocean.

Table of Contents

Page

List of Figures

Figure Page

List of Tables

NAVIGATION USING VECTOR AND TENSOR MEASUREMENTS OF THE EARTH'S MAGNETIC ANOMALY FIELD

I. Introduction

This thesis focuses on using a simulation trade study to determine the viability of using vector or tensor measurements of the Earth's magnetic anomaly field to navigate. Two navigation systems are presented and their ability to obtain an accurate estimate of vehicle position and attitude throughout a trajectory is evaluated.

1.1 Problem Statement

The Global Positioning System (GPS) has become a staple in civilian and military navigation systems. The United States has become highly reliant upon the GPS signal given its high accuracy. However, GPS is not without disadvantages. GPS is not always available in environments that have features that obstruct the signal, such as in heavily wooded areas, or in cities where the user is surrounded by large structures. The GPS signal is also susceptible to jamming or spoofing. In these cases, especially during military operations, the need for high-accuracy navigation still exists, and alternative signals need to be used to achieve this.

Similar to the GPS signal, the magnetic anomaly field of the Earth is a globally available signal. The Earth's magnetic field is always available and is not as susceptible to jamming or spoofing as GPS. Maps of the anomaly field signal are also available in varying resolutions over the entire globe [31]. Additionally, the Earth's magnetic anomaly field is a vector field that provides more than one signal to use for navigation. This research explores the navigation accuracy that is possible when

using the directional components of the magnetic anomaly vector field as well as its spatial gradients (tensor) to navigate.

1.2 Research Objectives

Two navigation systems are presented in this research. One system aids an Inertial Navigation System (INS) by matching measurements of the three directional components of the magnetic anomaly field to existing maps of the directional components of the field. The second aids the INS by matching measurements of the spatial gradients, or tensor, of the magnetic anomaly field to existing anomaly field tensor component maps.

Both navigation systems are tested in this research through simulation, using actual ship and airplane trajectories. Trade-space analysis was done to determine how changing different variables affects the accuracy of the navigation systems. The variables explored include the position and velocity of the truth trajectory, the types of measurements used in map-matching, the quality of INS that was used, and the map resolution. The results of this analysis will shed light on the viability of the proposed navigation systems as alternatives to GPS navigation.

1.3 Overview

This thesis is organized as follows. Chapter II provides a basic introduction to concepts used throughout the document, such as modeling and mapping the Earth's geomagnetic field, geomagnetic measurements and the instruments used to collect them and a brief background on the prevalent navigation filters used for magnetic navigation. Chapter II also provides an overview of previous and related work done in the field of magnetic navigation.

Chapter III outlines the two specific navigation systems used in this research.

It begins by defining the full dynamics and measurement models of the navigation system that uses vector measurements of the Earth's magnetic field. It then defines the full dynamics and measuremnet models of the navigation system that uses tensor measurements. Chapter III also presents details on the simulation framework developed, such as the specific trajectories used, the magnetic maps used, and the measurements and INS data that was simulated.

Chapter IV presents the results of the simulation trade study. The navigation accuracies of the two different navigation systems were compared for each trajectory and notable results were highlighted.

Chapter V concludes the thesis by giving an overview of the simulation trade study results. Chapter V outlines how navigation system performance was affected by changing the simulation parameters. Chapter V also includes possible areas for future work to improve navigation accuracies of the filters presented in this document and to determine their viability in real-world testing.

II. Background and Literature Review

2.1 Background Introduction

This purpose of this chapter is to provide a basic background to the reader on geomagnetic mapping and modeling, geomagnetic measurements, and the filters predominantly used in geomagnetic field navigation. Topics covered include the International Geomagnetic Reference Field (IGRF) model of the Earth's core field, external sources of the Earth's magnetic field, and the magnetic anomaly field caused by the geology of the Earth's crust. Scalar, vector and gradient measurements of the Earth's magnetic field will be introduced as well as the instruments used to take these measurements. The Kalman filter (KF) and extended Kalman filter (EKF) algorithms will be presented. Finally, a method for evaluating filter performance is described.

2.2 Geomagnetic Mapping and Modeling

The Earth's magnetic field, or the geomagnetic field, is comprised of the summation of several individual magnetic fields. The source that accounts for about 98% of the Earth's total geomagnetic field is the core field which is generated by electro-magnetic currents in the outer core of the Earth [12].

International Geomagnetic Reference Field.

The IGRF is a spherical harmonic model of the Earth's core field. It is published every five years by the International Association of Geomagnetism and Aeronomy (IAGA) [31]. Measurements of the geomagnetic field collected from observatories, low-altitude aerial surveys, and satellite surveys provide the basic data for fitting the IGRF model [12]. This type of model approximately fits a periodic model onto a sphere with a set of coefficients [7]. The degree of the harmonics correspond to

a spatial wavelength [7]. Higher degree harmonics correspond to higher frequency signals and vice-versa. The IAGA is able to approximately isolate the magnetic field due to the core field of the Earth, because harmonics of the geomagnetic field of up to degree 13 (3,100 km wavelength and longer) are dominated by the core field [12] as shown in Figure 1. The IGRF models the core field by only including harmonics up to degree 13 [12]. The IGRF also includes approximations for secular variations, or long-term variations in both magnitude and direction of the core field, based on the actual rate of change from previous years [12].

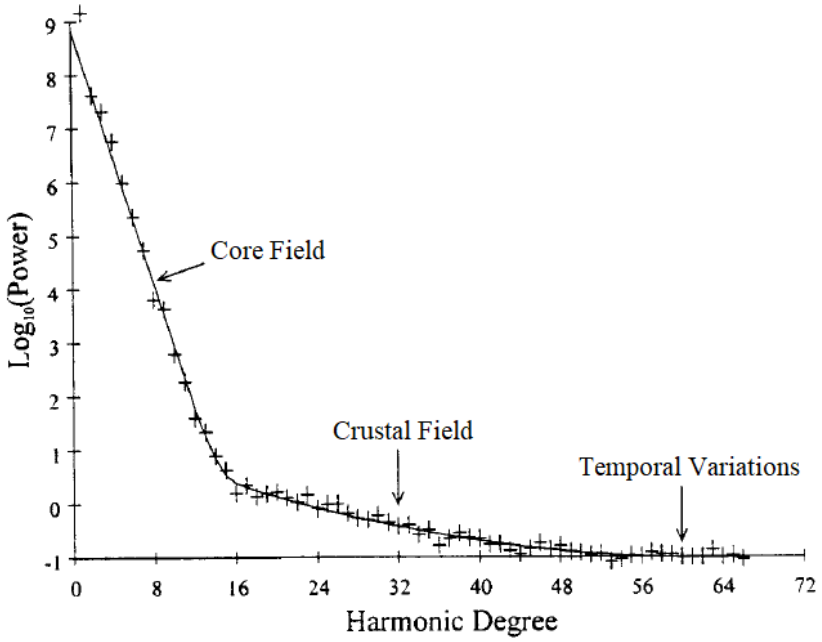

Figure 1. Power Spectral Density of Earth's Total Magnetic Field Spherical Harmonics [25]

Temporal Variations.

Variations in the total magnetic field that stem from sources external to the Earth are considered temporal variations. The strength of the magnetic field due to these external sources is weak compared to the magnetic field due to the Earth's core. Also, temporal variations are often on a much shorter time scale than secular variations,

so they can be approximately separated from the core field [25]. Because temporal variations occur in such rapid cycles, they are not captured by the IGRF.

Temporal variations can be identified for navigation purposes by their frequency. Low-frequency variations tend to look like constant biases for short-term navigation, while the higher-frequency variations look like white noise [7]. The variations that occur at a similar frequency as data used for magnetic navigation are more difficult, if not impossible, to separate from the anomaly field [7].

The Earth's ionosphere is a shell of ionized gas that reaches from about 50 km to beyond 1000 km above the Earth's surface. Movement of ions in the ionosphere result in electrical currents, which induce magnetic fields. One cause of the movement of these ions is solar heating [12]. Solar heating leads to current loops during the daytime hours, which causes a distortion in the Earth's magnetic field as the Earth completes its daily rotation [31]. This cycle, as well as the gravitational pull of the moon, creates atmospheric tidal waves, which generally result in a variation of the total geomagnetic field of less than approximately 50 nanoTeslas (nT) over the course of a day, except during periods of increased solar wind [31].

Solar wind is radiation from the sun that causes a distortion in the Earth's core field into a comet-like shape that is known as the Earth's magnetosphere as shown in Figure 2 [12]. Currents within the magnetosphere caused by the interaction of solar wind with the magnetic field are also a contributor to temporal variations.

Solar storms are characterized as a period in time where the Earth is subjected to an unusually high amount of solar wind. The timing of solar storms is unpredictable and may lead to disturbances in the magnetic field of hundreds of nT or greater when the particles interact with the Earth's magnetic field [12].

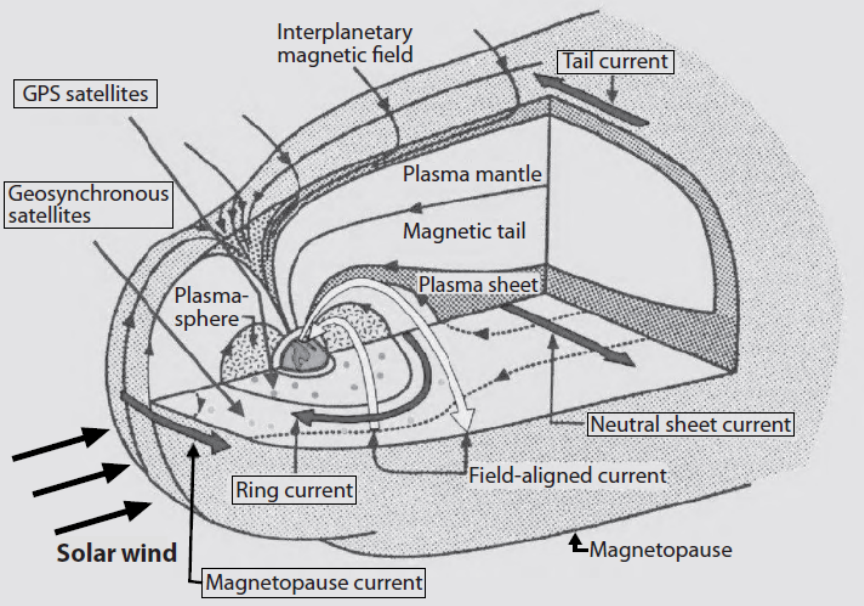

Figure 2. Earth's Magnetosphere [12]

Crustal Sources.

The final source of interest that contributes to the Earth's total magnetic field is the Earth's crust, which accounts for a small portion of the total field. The crustal field is made up of the superposition of all induced and remnant magnetization in the rocks and sediments that make up the Earth's crust. Magnetization of a material in the Earth's crust, a rock for example, consists of both induced and remnant components. The induced component of the magnetic field exists only in the presence of an external magnetic field, when the magnetic moment of the atoms that make up the material align under an external field, and adds to the total magnetization of the material [12]. Induced magnetization within a material is dependent upon the magnetic susceptibility of that material. Magnetic susceptibility is the ease with which the material is magnetized by an external field [12].

Remnant magnetization is the component of a material's total magnetization that is retained from a previous magnetic environment. The remnant component of the material's magnetization is present without an external magnetic field and adds to the

induced component to give the total magnetization of the material [12]. The direction of remnant magnetization is generally not in the same direction as the external field, as is the case with induced magnetization; However, the magnitude of a materials remnant magnetization versus its induced magnetization is generally much smaller [12].

The spatial variation of the crustal field varies at a high frequency relative to the core field. When flying over the crustal field, the frequency of the crustal field overlaps with the frequency of the temporal variations as described above, making it difficult to distinguish the two signals [7].

Magnetic Anomaly Mapping.

A magnetic anomaly is a vector deviation from a reference field. For the purposes of magnetic navigation, the reference field used is the Earth's core field, and the vector deviations, or magnetic anomaly vectors, come from the Earth's crustal field. The crustal field is relatively static and has a high spatial frequency, which makes it a good signal to use for magnetic navigation [7]. Maps have been created to capture a representation of the Earth's magnetic anomaly vectors, but a distinction must be made between the true anomaly vector at each observation point, and the scalar representation present in the magnetic anomaly maps at each corresponding observation point.

The Earth's total magnetic field vector $\mathbf{B_t}$ is approximately the vector sum of the Earth's core field ($\mathbf{B_{IGRF}}$) and the Earth's crustal field ($\mathbf{B_a}$) as shown in Equation 1. During magnetic surveys, care is taken to remove the effects of the temporal variations from the measurements, so the total field vector is an approximation of the sum of the Earth's core field and crustal field. Some of the effects from the temporal variations

remain and are included in the total anomaly field vector [7].

$$\mathbf{B_t} = \mathbf{B_{IGRF}} + \mathbf{B_a} \tag{1}$$

Figure 3 shows a visual representation of this vector summation. $\mathbf{B}_a$ is exaggerated in the figure for clarity and its intensity is more on the order of 2% of the intensity of $\mathbf{B}_{IGRF}$.

Figure 3. Earth's Total Field as a Vector Sum of Earth's Core and Crustal Field Components

Given current instrumentation limitations, only the intensity of the total field vector $\mathbf{B_t}$ is usually collected during magnetic surveys as opposed to the intensity and direction of the vector. However, the intensity and direction of the core field vector ($\mathbf{B_{IGRF}}$) is available from the IGRF model. Because we do not have the direction of the total field vector, we can not do a direct vector subtraction between the core field and the total field measurement to obtain the full anomaly vector shown in Figure 3. Instead, knowing that the intensity of the core field vector is much greater than the intensity of the anomaly field vector allows for the assumption that the anomaly field vector can not perturb the direction of the Earth's core field. Because of this, it can be assumed that subtracting the intensity of the core field vector from the intensity measurement of the total field vector gives a good approximation of the projection of the anomaly field vector in the direction of the core field. It is this approximate projection in the direction of the core field, or the amount that the anomaly vector "stretches" or "shrinks" the core field vector that is represented in the magnetic anomaly maps [7]. Figure 4 gives a visual representation of this assumption.

Figure 4. Approximated Projection Presented in Magnetic Anomaly Maps

Because $|\mathbf{B_{IGRF}}| \gg |\mathbf{B_a}|$, we assume the following:

$$|\mathbf{B_{approx}}| = |\mathbf{B_t}| - |\mathbf{B_{IGRF}}| \tag{2}$$

2.3 Geomagnetic Measurements

As described above, the Earth's magnetic field is a vector field, so at any given point the direction of the magnetic field corresponds to the orientation of the vector, and the strength of the magnetic field corresponds to the length of the vector.

Scalar Measurements.

Scalar measurements of the magnetic field only capture the magnitude, or intensity, of the magnetic field. In Figure 5, the length of the vector $\mathbf{B}$ shown corresponds to the intensity of the magnetic field at that point. With an ideal scalar intensity sensor oriented in any direction at a given point, the scalar intensity measurement will be constant.

Scalar intensity measurements include the magnitude of the Earth's total magnetic field, so care must be taken to eliminate the effects of external fields and the core field to get the magnetic anomaly value.

Vector Measurements.

Vector measurements fully capture the intensity and direction of the magnetic field. The vector $\mathbf{B}$ shown in Figure 5 can be separated into its individual components B_x, B_y and B_z. The magnitude of $\mathbf{B}$ is a scalar quantity and can be calculated with

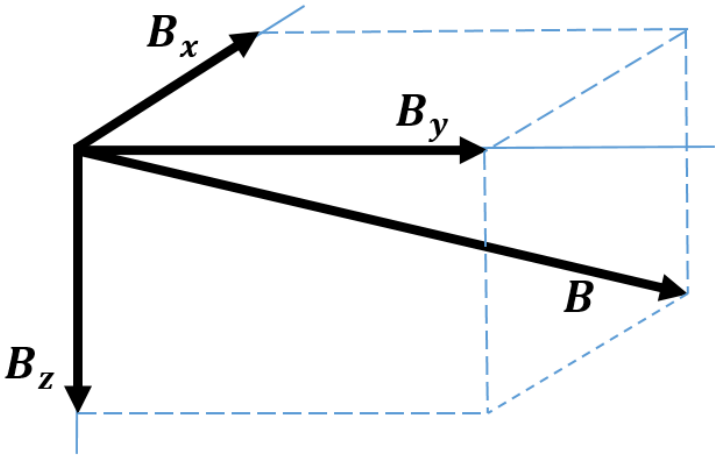

Figure 5. Magnetic Field Vector Seperated Into Vector Components

the following formula:

$$\mathbf{B} = \sqrt{B_x^2 + B_y^2 + B_z^2} \tag{3}$$

When the length of B_x, B_y and B_z are measured separately, we are able to calculate the intensity of the magnetic field vector as shown above as well as its direction. As with scalar intensity measurements, the vector $\mathbf{B}$ represents the Earth's total magnetic field including the magnetic field due to the Earth's core, the Earth's crust, and external fields. The magnitude of each directional component of the magnetic field vector is different depending on the orientation of the sensor at any given point, even if the total intensity stays constant. When using a vector sensor as opposed to a scalar sensor, more care needs to be taken to accurately track the sensor's attitude, because even the slightest error in attitude could lead to high errors when solving for the separate vector components. For example, if the green vector in Figure 6 is the true magnetic field vector, and we have 0.01 degrees of attitude error (resulting in the orange vector), we end up with 8.73 nT of error in the y-component of the magnetic field vector.

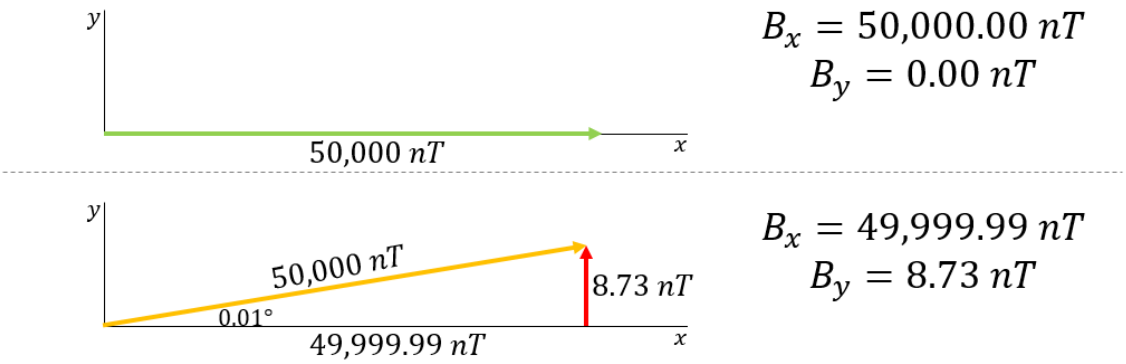

Figure 6. Vector Components with and without Attitude Error

With vector measurements, a coordinate frame transformation is required to transform the measurements from the body frame to the local or navigation (nav) frame. The body frame is aligned with the roll, pitch and yaw axes of the vehicle [39]. The x-axis points out the front of the vehicle, the y-axis points out the right side of the vehicle, and the z-axis points down. The nav frame is a local geographic frame that has its origin at the location of the vehicle. Its axes are aligned with the geographic north, east and down directions [39].

The magnetic field measurement from the sensor is in the body frame and is denoted as $\mathbf{B}_b$ and is rotated to the nav frame using Equation 4 [27].

$$\mathbf{B_n} = \mathbf{C_b^n B_b} \tag{4}$$

$\mathbf{B}_n$ is the vector measurement expressed in the nav frame and $\mathbf{C_b^n}$ is the direction cosine matrix required to transform the measurement from the body frame to the nav frame. The roll, pitch, and yaw angles (γ, θ and ψ) of the vehicle may be used to calculate the transformation matrix, $\mathbf{C_b^n}$. These calculations are shown in Equation

5 [13].

$$\mathbf{C_b^n} = \begin{bmatrix} \cos\gamma\cos\psi + \sin\gamma\sin\psi\sin\theta & -\cos\gamma\sin\psi + \sin\gamma\cos\psi\sin\theta & -\sin\gamma\cos\theta \\ \sin\psi\cos\theta & \cos\psi\cos\theta & \sin\theta \\ \sin\gamma\cos\psi - \cos\gamma\sin\psi\sin\theta & -\sin\gamma\sin\psi - \cos\gamma\cos\psi\sin\theta & \cos\gamma\cos\theta \end{bmatrix} \tag{5}$$

Gradient Tensor.

Magnetic gradient measurements provide the difference between two magnetometer readings, either scalar or vector, taken simultaneously with a constant distance between them, or the spatial derivative of the magnetic field with respect to the distance between them. For our purposes, we will focuse on vector gradients. The partial derivative of the x-component of the magnetic field vector (B_x) with respect to the x-direction is denoted as $\partial_x B_x$ or B_{xx}. If four sensors were configured on an axes as in Figure 7, $B_{xx} = B_{x1} - B_{x3}$, or the difference in the x-component of the magnetic field vector as the distance along the x-direction changes. Similarly, the partial derivative of the y-component of the magnetic field vector (B_y) with respect to the x-direction is denoted as $\partial_x B_y$ or B_{yx}. This would correspond to the difference between B_{y1} and B_{y3} in Figure 7. Gathering these partial derivatives into a 3×3 matrix produces the full nine-component magnetic gradient tensor, $\mathbf{G}$.

$$\mathbf{G} = \frac{\partial \mathbf{B}}{\partial \mathbf{R}} = \begin{bmatrix} \partial_x B_x & \partial_y B_x & \partial_z B_x \\ \partial_x B_y & \partial_y B_y & \partial_z B_y \\ \partial_x B_z & \partial_y B_z & \partial_z B_z \end{bmatrix} = \begin{bmatrix} B_{xx} & B_{xy} & B_{xz} \\ B_{yx} & B_{yy} & B_{yz} \\ B_{zx} & B_{zy} & B_{zz} \end{bmatrix} \tag{6}$$

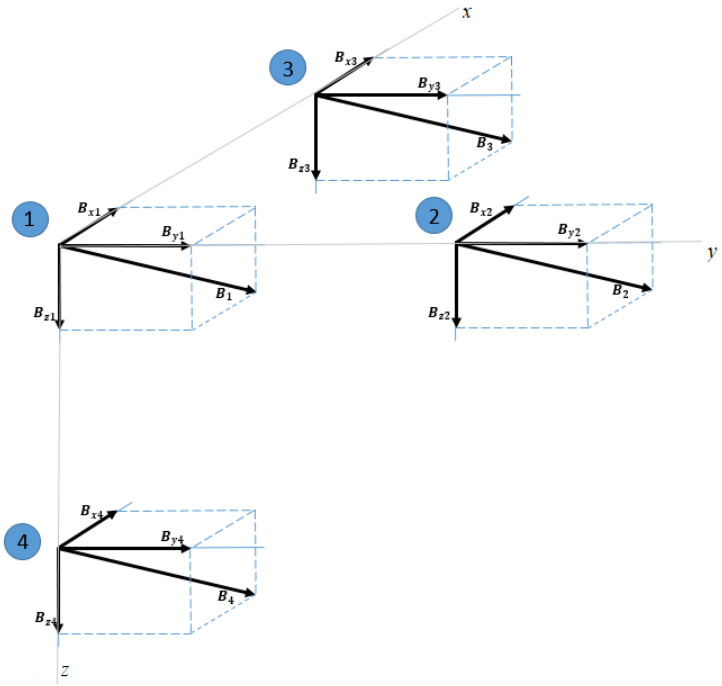

Figure 7. Configuration of Four Vector Sensors

where

$$\mathbf{B} = \begin{bmatrix} B_x \\ B_y \\ B_z \end{bmatrix}$$

$$\mathbf{R} = \begin{bmatrix} x \\ y \\ z \end{bmatrix}$$

$\mathbf{G}$ is a symmetric and traceless matrix, meaning $\mathbf{G}^T = \mathbf{G}$ and $B_{xx} + B_{yy} + B_{zz} = 0$ [19]. Because the matrix is symmetric, we know that $B_{yx} = B_{xy}$, $B_{zx} = B_{xz}$ and $B_{zy} = B_{yz}$. Because the matrix is traceless, we know that $B_{zz} = -(B_{xx} + B_{yy})$. These properties of the tensor leave us with five unique components out of the nine elements of the tensor: $B_{xx}, B_{xy}, B_{xz}, B_{yy}$, and B_{yz}.

As with vector measurements, the tensor measurements also require a transfor-

mation to put the local sensor frame measurements into the navigation frame. The equation for this transformation is below [27]:

$$\mathbf{G_n} = \mathbf{C_b^n}\,\mathbf{G_b}\,\mathbf{C_b^{n}}^T \tag{7}$$

where G_n is the tensor measurement rotated into the nav frame and G_b is the body-frame measurement.

Scalar Magnetometers.

Different instruments are used to collect magnetic field data depending on which type of measurement is desired. For scalar measurements, nuclear resonance magnetometers have sensors containing fluids or gases with properties that are sensitive to changes in the magnetic field. These are strictly scalar sensors that measure the absolute intensity of the magnetic field, but give no direction information [12]. The Geometrics airborne Cesium Resonance Magnetometer (G-823A) specifies a sensitivity of 0.004 nT/$\sqrt{\text{Hz}}$ and absolute accuracy of less than 3 nT [11]. This high sensitivity and accuracy makes the Cesium Magnetometer a good example of an instrument that is used to collect absolute intensity measurements during magnetic surveys.

Vector Magnetometers.

Fluxgate magnetometers are one type of sensor used to measure the vector components of the relative magnetic fields [7]. The fluxgate within the sensor is a transducer that converts the magnetic field in one direction into a voltage. These sensors are small, durable, reliable and do not require much power to operate [23]. A Bartington Mag-03 Fluxgate magnetometer has similar sensitivity values to that of the Cesium Magnetometer (0.006 - 0.01 nT/$\sqrt{\text{Hz}}$), but is much less accurate. With the Mag-03, if we are in an operating range of $\pm 70,000$ nT, we can get up to 350 nT of error given

the 0.5% scaling error listed in the data sheet [3]. Additional error is added when we take into account orthogonality errors in the mechanical sensor configuration.

Magnetic Gradiometers.

Using a vector gradiometer, as opposed to vector or scalar sensors as discussed above, virtually eliminates regional and temporal effects on the measurements [31]. This is due to the fact that the spatial gradient for temporal variations is nearly zero [7]. The Bartington Grad-13 consists of two Mag-03 Fluxgate Magnetometers separated by a distance of 1 m. This instrument is able to measure B_{xx}, B_{yx}, and B_{zx} and may be visualized as sensor 1 and 3 from Figure 7. The Grad-13 has sensitivities similar to the scalar and vector sensors ($0.02\,\mathrm{nT}/\sqrt{\mathrm{Hz}}/\mathrm{m}$), but with a higher accuracy than the vector sensor (± 70 nT with the 0.1% scaling error listed in the data sheet) [2]. While the accuracy is far less than the scalar sensor, the gradiometer gives us much more information about the magnetic field at each location, to include B_x, B_y, and B_z of the magnetic field at the reference sensor as well as B_{xx}, B_{yx}, and B_{zx}.

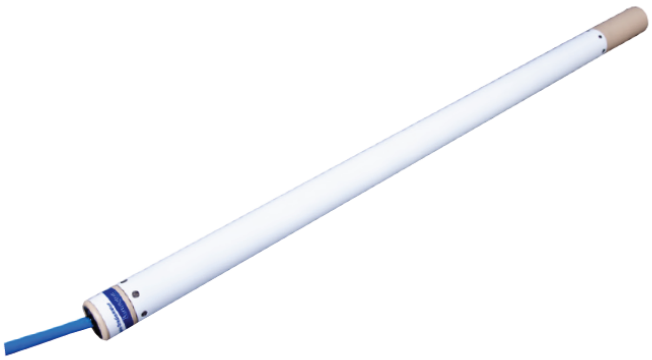

Figure 8. Bartington Grad-13 Three-Axis Gradiometer [2]

Using a Grad-13 gradiometer eliminates the need to perform the vector magnetometer calibration as described above, because the Bartington gradiometer outputs corrected three-axis data from the vector-magnetometers [2].

A magnetic tensor configuration would allow us to record the same information as the magnetic gradiometer with the addition of the two unique gradient measurements required to calculate the full tensor matrix. The required configuration is similar to that displayed in Figure 7. Figure 9 shows five Honeywell HMR2300 Vector Magnetometers arranged into a tensor configuration that was assembled at the Air Force Institute of Technology.

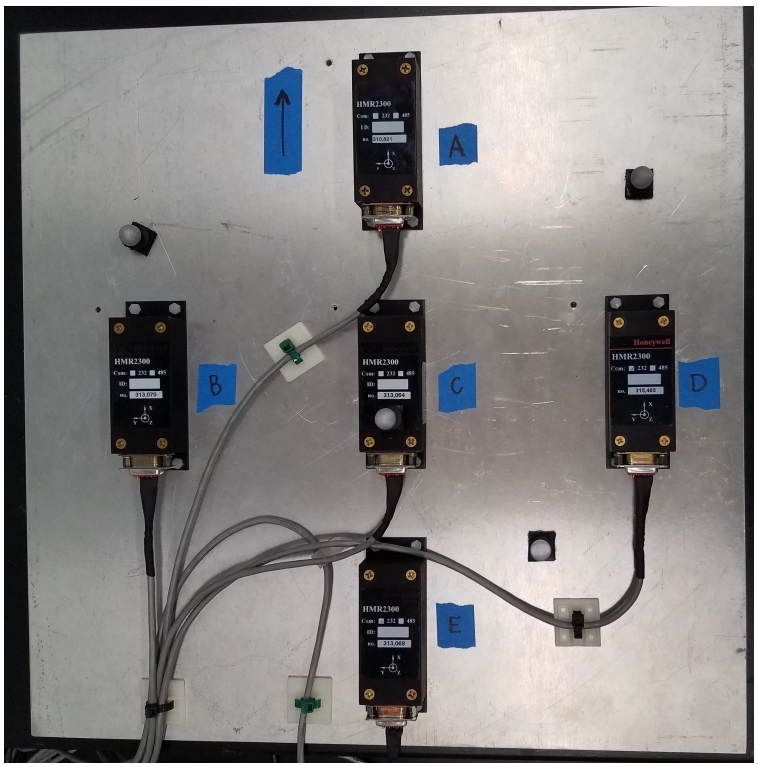

Figure 9. AFIT Tensor Measurement Assembly

2.4 Kalman Filter

Kalman filtering is one method used to process noisy measurements such as magnetometer measurements into optimal estimates of system random processes over time. In basic Kalman Filtering, the dynamics of a set of random variables can be modeled with Equation 8 for continuous-time processes or Equation 9 for discrete-time

processes.

$$\dot{\mathbf{x}}_k = \mathbf{F}_k\mathbf{x}_k + \mathbf{B}_k\mathbf{u}_k + \mathbf{w}_k \tag{8}$$

$$\mathbf{x}_{k+1} = \mathbf{\Phi}_k\mathbf{x}_k + \mathbf{w}_k \tag{9}$$

The measurement function is shown in Equation 10.

$$\mathbf{z}_k = \mathbf{H}_k\mathbf{x}_k + \mathbf{v}_k \tag{10}$$

where

$\mathbf{x}_k$ is the $(n \times 1)$ process state vector at time k

$\mathbf{\Phi}_k$ is the $(n \times n)$ state transition matrix that relates the matrix $\mathbf{x}_k$ to $\mathbf{x}_{k+1}$

$\mathbf{B}_k$ is the $(n \times n)$ control input model matrix

$\mathbf{u}_k$ is the $(n \times 1)$ input matrix

$\mathbf{w}_k$ is the $(n \times 1)$ vector that includes the additive white Gaussian noise (AWGN) contribution to the state vector for the time interval $(k+1, k)$

$\mathbf{F}_k$ is the $(n \times n)$ dynamics matrix

$\mathbf{z}_k$ is the $(m \times 1)$ measurement vector at time k

$\mathbf{H}_k$ is the $(m \times n)$ matrix that relates $\mathbf{x}_k$ to $\mathbf{z}_k$

$\mathbf{v}_k$ is the $(m \times 1)$ vector that includes the AWGN measurement error

The covariance matrices for $\mathbf{w}_k$ and $\mathbf{v}_k$ are

$$E[\mathbf{w}_k\mathbf{w}_k^T] = \mathbf{Q}_k \tag{11}$$

$$E[\mathbf{v}_k\mathbf{v}_k^T] = \mathbf{R}_k \tag{12}$$

The error in the state estimate is defined as

$$\mathbf{e}_k^- = \mathbf{x}_k - \hat{\mathbf{x}}_k^- \tag{13}$$

where $\hat{\mathbf{x}}_k^-$ is the estimate of the state at time k. This estimate is based on all prior knowledge about the process prior to k. This is the estimate of the state before the measurement update has been applied at time k.

$$\mathbf{P}_k^- = E[\mathbf{e}_k^-(\mathbf{e}_k^-)^T] \tag{14}$$

The prior estimate $\hat{\mathbf{x}}_k^-$ is improved by implementing a measurement update as shown below:

$$\hat{\mathbf{x}}_k = \hat{\mathbf{x}}_k^- + \mathbf{K}_k(\mathbf{z}_k - \mathbf{H}_k\hat{\mathbf{x}}_k^-) \tag{15}$$

where $\hat{\mathbf{x}}_k$ is the updated estimate at time k and $\mathbf{K}_k$ is the Kalman gain, which is the optimal gain that minimizes the mean-square estimation error and is computed by the following equation:

$$\mathbf{K}_k = \mathbf{P}_k^-\mathbf{H}_k^T(\mathbf{H}_k\mathbf{P}_k^-\mathbf{H}_k^T + \mathbf{R}_k)^{-1} \tag{16}$$

The error covariance matrix for the updated estimate is computed using the following formula:

$$\mathbf{P}_k = (\mathbf{I} - \mathbf{K}_k\mathbf{H}_k)\mathbf{P}_k^- \tag{17}$$

The updated estimate and the error covariance matrix are then propagated for-

ward in time using the formulas:

$$\hat{\mathbf{x}}_{k+1}^{-} = \mathbf{\Phi}_k \hat{\mathbf{x}}_k \tag{18}$$

$$\mathbf{P}_{k+1}^{-} = \mathbf{\Phi}_k \mathbf{P}_k \mathbf{\Phi}_k^T + \mathbf{Q}_d \tag{19}$$

where $\mathbf{Q}_d$ is the discretized covariance matrix for $\mathbf{w}_k$ approximated by multiplying $\mathbf{Q}$ by the time difference between successive time steps.

This process, which is considered the Kalman filter, continues recursively until estimates have been made for the entire trajectory. A complete derivation of the Kalman filter equations can be found in [6].

2.5 Extended Kalman Filter

The Kalman filter algorithm is only optimal in systems that have linear dynamics and measurement models. When either the dynamics or measurement model are non-linear, the EKF may be used. The EKF assumes that the state transition function and measurement function are governed by nonlinear functions $\boldsymbol{f}$ and $\boldsymbol{h}$ respectively.

The dynamics are modeled by the following equation:

$$\dot{\mathbf{x}}_k = \mathbf{f}[\mathbf{x}_k, \mathbf{u}_k] + \mathbf{w}_k \tag{20}$$

The measurement function follows the equation below:

$$\mathbf{z}_k = \mathbf{h}[\mathbf{x_k}] + \mathbf{v_k} \tag{21}$$

Unlike in the Kalman filter, the matrix $\mathbf{H}_k$ must be recalculated at each time step. $\mathbf{H}_k$ is the Jacobian of the measurement function $\boldsymbol{h}$ from equation 21 evaluated

at each time step. The measurement Jacobian is defined below:

$$\mathbf{H}_k \triangleq \frac{\partial \mathbf{h}(\mathbf{x}, k)}{\partial \mathbf{x}}\Big|_{\mathbf{x}=\hat{\mathbf{x}}_\mathbf{k}^-} \tag{22}$$

The prior estimate at time k, $\hat{\mathbf{x}}_k^-$ is updated using equation 23 below, while the error covariance matrix is updated using Equation 24.

$$\hat{\mathbf{x}}_k = \hat{\mathbf{x}}_k^- + \mathbf{K}_k[\mathbf{z}_k - \mathbf{h}(\hat{\mathbf{x}}_k^-, k)] \tag{23}$$

$$\mathbf{P}_k = (\mathbf{I} - \mathbf{K}_k\mathbf{H}_k)\mathbf{P}_k^- \tag{24}$$

The Kalman gain is computed using Equation 25.

$$\mathbf{K}_k = \mathbf{P}_k^-\mathbf{H}_k^T(\mathbf{H}_k\mathbf{P}_k^-\mathbf{H}_k^T + \mathbf{R}_k)^{-1} \tag{25}$$

Once the updated state estimate and error covariance matrix are calculated, they may be propagated forward using the following formulas:

$$\hat{\mathbf{x}}_{k+1}^- = \mathbf{f}[\hat{\mathbf{x}}_k, \mathbf{u}_k] \tag{26}$$

$$\mathbf{P}_{k+1}^- = \mathbf{\Phi}_k\mathbf{P}_k\mathbf{\Phi}_k^T + \mathbf{Q}_d \tag{27}$$

where $\mathbf{\Phi}_k$ is the matrix exponential of $\mathbf{F}_k$, which is the Jacobian of the function $\boldsymbol{f}$ from equation 20. Equation 28 defines the dynamics function Jacobian required to propagate the states and error covariance from time t_k to time t_{k+1}.

$$\mathbf{F}_k \triangleq \frac{\partial \mathbf{f}(\mathbf{x}, k)}{\partial \mathbf{x}}\Big|_{\mathbf{x}=\hat{\mathbf{x}}_k} \tag{28}$$

The state estimates and covariance are updated and propagated recursively until estimates have been made for the entire trajectory. A detailed derivation of the EKF

algorithm may be found in [24].

2.6 Marginalized Particle Filter

A specialized filter may be required to handle magnetic field navigation given the non-linearity of the map-matching problem. With inaccurate initial state estimates and no processing power limitations, the particle filter would be the filter of choice. The drawback of using the particle filter is its computational intensity.

A particle filter is a simulation-based estimation technique used in filtering problems to estimate the latent states of a complex dynamic statistical model, where after each observation, the state that gave rise to that observation is estimated [37].

The benefit of using a particle filter is its ability to handle highly non-linear dynamics and measurement models. As the number of particles approaches infinity, all possible values of each state can be estimated and the filter can determine the most likely state estimate.

To estimate each state accurately, a large number of particles must be used. For a system model with nearly 20 states, the processing power required to perform the particle filter computations for all states is not viable [34]. To get around this limitation, an extension of the particle filter, the marginalized particle filter (MPF), may be used that separates the states that have linear dynamics from the states that have non-linear dynamics by partitioning the state vector. The linear states are then handled by a standard KF or EKF, while the non-linear states are handled by the standard particle filter. For a navigation filter, a majority of the states are linear, so the required processing power is reasonable when the MPF is employed. The MPF algorithm may be found in [34].

2.7 Cramer-Rao Lower Bound

The Cramer-Rao Lower Bound (CRLB) is the lowest possible state covariance of an estimator, such as the filter types described above [4]. [4] derived the CRLB for a terrain-aided navigation problem and concluded that the CRLB is equivalent to the error covariance in the EKF, with the measurement function $\boldsymbol{h}$ from Equation 21 replaced with its gradient evaluated at the true state values at time k as opposed to the estimate of the state vector. This allows a comparison to be made between the CRLB and the actual filter error covariance to evaluate filter performance. A high-performing filter should have error covariances close to, but not less than, the CRLB for all states. Additionally, the CRLB sets a lower limit on the DRMS of the filter and can be used to calculate how far from optimal the filter performs [4].

2.8 Background Conclusion

In this chapter, an overview of the sources of the Earth's total magnetic field have been presented: the Earth's core field modeled in the IGRF, temporal variations due to external sources, and the Earth's crustal field. The magnetic anomaly field has been described as well as the distinction between the true anomaly field and the anomaly field value given in magnetic anomaly field maps. The difference between scalar, vector, and gradient measurements has been described and the instruments used to collect these measurements have been introduced. The Kalman filter and Extended Kalman filter algorithms were presented as well as a brief overview of the marginalized particle filter and an explanation of its benefits and limitations. The CRLB was presented to describe its merit in evaluating filter performance.

2.9 Literature Review

Abundant research has been done on the field of non-GPS navigation, some of which pertains to magnetic field navigation. Navigation using the earth's magnetic anomaly field has been investigated on several different platforms (aerial, sea-level, sub-sea-level, ground, and indoor). A majority of previous work for all platforms explored magnetic navigation using a scalar signal as opposed to the full magnetic field vector or tensor. However, other research has been done using the vector and tensor measurements of the magnetic field for UXO detection [17]. Each of these cases will be described in the paragraphs that follow.

Research by A. Canciani [7] explored improving aerial navigation using the intensity of the magnetic anomaly field. Using this scalar measurement of the anomaly field, Canciani was able to demonstrate navigation accuracy of 13 meters distance root mean square (DRMS) in real flight tests. A limitation of Canciani's research includes the use of one scalar measurement that is only able to capture the magnitude of the magnetic anomaly field. Additionally, high-accuracy results require a relatively high-velocity platform. The research may be expanded and improved upon using three measurements that capture all vector components of the anomaly field to increase navigation accuracy overall and at lower velocities (e.g. sea platforms).

Research done by J. Wilson and R. Kline-Schoder [41] provides an aerial navigation solution using a magnetically-aided dead-reckoning system. This system uses air speed to provide a dead-reckoned navigation solution, with position updates provided by the magnitude of the magnetic anomaly field. A tri-axial magnetometer was used, however, given the limitations of the magnetic anomaly map, these vector measurements were only used to calculate the scalar magnetic field strength. With this dead-reckoning system, position errors of 600 to 1200 m were achieved for flights after one hour with only moderate attempts to calibrate the magnetometers. Much

of this error could be due to aircraft noise, because the sensors were housed in the fuselage during flight.

Three-axis magnetometer measurements and magnetic field maps were used in the dissertation by J. Shockley [36] to demonstrate self-contained ground-vehicle magnetic navigation. However, Shockley did not use inertial navigation system (INS) aiding to get high-precision results. Shockley was able to demonstrate navigation accuracy of 25-34 meters using a single magnetometer in a sedan and comparing it to a map he generated by sampling the magnetic field along the roadway at known positions. All measurements are taken in the vehicle's body frame and not converted to an absolute reference frame. Because of this, the mapping platform and the measurement platform are assumed to have the same attitude at each sample point and be traveling in the same direction between sample points. This sample point technique would not suffice for aerial applications where the measurements require a coordinate frame transformation. The results may be improved upon by pairing the three-axis magnetometer with an INS for higher-accuracy results that provide both a position and heading solution.

W. Storms [38] used a three-axis magnetometer and a magnetic field intensity map for his research on indoor magnetic navigation. The heading angle was assumed to be known. The indoor navigation explored here required an INS and a previously generated map of the same indoor trajectory to be traversed by the user (taken at the same heading as the assumed user heading) for position updates. W. Storms was able to achieve position errors less than 0.2 m at all times with this method, but the solution only provided observability of the x- and y- position. This same method could be extended to estimate the heading as well.

Similarly, research has been done in an indoor environment using four orthogonally mounted three-axis magnetometers to provide observability of the velocity of a person

traversing an indoor environment. The approach presented does not require the use of a magnetic map, because the trihedron gives a direct measurement of the magnetic field spatial partial derivatives [40].

D. Jeon fused odometer data with magnetic sensor data for indoor localization of an autonomous vehicle. An unscented Kalman filter (UKF) was used for the localization system that is based on magnetic markers in an indoor environment [14]. A magnetic map was created by storing the location of magnetic markers. A sensor was used to detect a magnet and match its reading to magnetic field data on the map to obtain an estimated position. The results show that the localization system was able to attenuate the cumulative position and heading errors of the vehicle that were present when only odometer measurements were used [14].

Sub-sea-level navigation presents its own unique challenges. Underwater platform navigation solutions frequently require INS aiding by surfacing to obtain a GPS fix. This is impractical and leaves vehicles such as military submarines vulnerable to detection. Previous research has been done by T. Karlsson [15] on terrain aided underwater navigation using a narrow-beam altimeter to aid the INS with a measurement of the depth directly below the vehicle. N. Kato [16] studied underwater navigation of autonomous underwater vehicles using both geomagnetic measurements and bathymetric measurements. N. Kato concluded that underwater trajectories with a higher variation of bathymetric data gave higher accuracy navigation solutions. This is similar to aerial navigation solutions having higher accuracy when using a magnetic field map with a rich signal or traversing the magnetic field quickly leading to higher variation in magnetic field measurements [7]. Y. Huang presents a method to fully determine the attitude of an underwater vehicle to be used in underwater navigation problems [13]. The method is based on the use of full magnetic field tensor measurements. The algorithm worked successfully only when the initial angle error was less

than 20 deg and the sensor noise was less than 10 nT [13].

Minimal research has been done using magnetic underwater navigation given the challenges presented by the low velocity of a moving submarine, however the use of magnetic tensor gradiometers has been researched for underwater unexploded ordnance (UXO) detection [17].

III. Methodology

Chapter III focuses on the detailed design of the navigation systems presented in this research. First, the reasoning for using the EKF in both navigation systems is presented. Then the detailed filter design for the navigation system that uses vector measurements is presented. This is followed by the filter design of the navigation system that uses tensor measurements. After the filter designs are laid out, the features of the simulation framework are outlined.

Filter Type.

The EKF was chosen for magnetic anomaly field navigation using vector measurements. In scalar magnetic navigation, the filter estimates a vehicle's location by matching a magnetometer measurement to a location on the magnetic anomaly map that corresponds to the measurement. It is highly likely that there is more than one location with a map value closely matching the measurement. If a distribution of the possible map locations of the vehicle was generated after the filter received one measurement, this distribution of the latitude and longitude states would look highly non-Gaussian and would not fit a linearized model well. This is why the MPF was used for previous research into scalar magnetic anomaly field navigation [7].

Figure 10 shows the multi-variate distribution of the latitude and longitude states after a measurement update when a scalar measurement (B) was brought into the filter. When overlayed onto the magnetic field map, the shape of this multi-variate distribution is dependent on the shape of the contour line with a magnetic anomaly field value that matches the single measurement brought into the filter.

The benefit of bringing three measurements into the filter as opposed to one is that the shape of the distribution is no longer conforming to the shape of a contour line, but of the intersection of three contour lines, one for each separate component of

the vector field. Figure 11 shows the distribution after a measurement update when three measurements (B_x, B_y and B_z) are brought into the filter. The distribution is overlayed onto the magnetic field maps of B_x, B_y and B_z. This distribution looks more Gaussian than in Figure 10. An MPF is no longer required, because the EKF can, in theory, handle the Gaussian distribution that is created. This highly reduces the amount of processing power required.

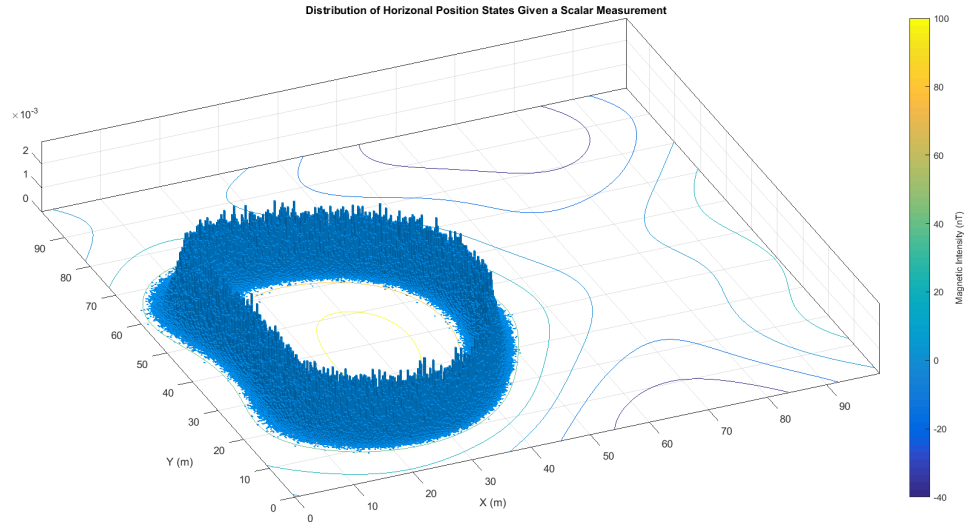

Figure 10. Probability Distribution of the Horizontal Position States Overlaid on the Scalar Magnetic Anomaly Contour Map

One drawback of the EKF in magnetic field navigation is its inability to handle multi-modal distributions. If the initial position uncertainty is large, the distribution of the latitude and longitude states after a measurement update could be multi-modal, leading to several possible position solutions. In order for the distribution to remain Gaussian and the EKF to perform well, it must be provided with accurate initial conditions. With an accurate estimate of the starting location, the distribution is not likely to be multi-modal. For this research, we operate under the assumption that the INS will be initialized using a true position from GPS, thus giving the filter accurate initial conditions.

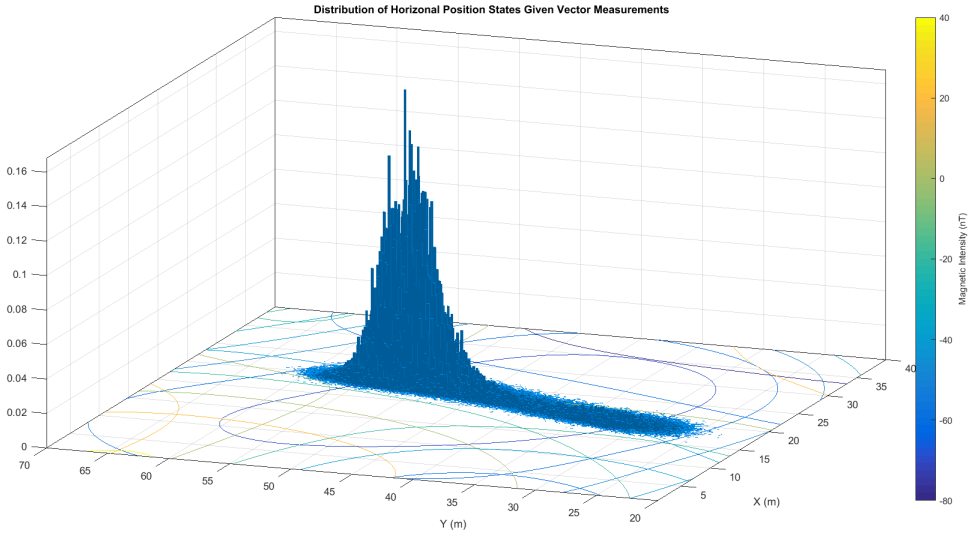

Figure 11. Probability Distribution of the Horizontal Position States Overlaid on Component Magnetic Anomaly Contour Maps

3.1 Navigation Filter Using Vector Measurements

The first navigation system will use vector measurements of the anomaly field as well as inputs from an INS to aid the INS and constrain the position and angular drift within its sensors. In this section, the filter states will be introduced as well as the dynamics model and measurement function.

Filter States.

The filter estimates twenty states. The first seventeen states estimate INS errors and the last three states estimate the strength of temporal variations in each axis of the magnetic vector field. The state vector is following:

$$\mathbf{x}_k = [lat_\epsilon \quad lon_\epsilon \quad alt_\epsilon \quad v_\epsilon^N \quad v_\epsilon^E \quad v_\epsilon^D \quad \epsilon_x \quad \epsilon_y \quad \epsilon_z \quad h_\epsilon^a$$

$$a_\epsilon \quad acc_\epsilon^x \quad acc_\epsilon^y \quad acc_\epsilon^z \quad g_\epsilon^x \quad g_\epsilon^y \quad g_\epsilon^z \quad TV_\epsilon^x \quad TV_\epsilon^y \quad TV_\epsilon^z]^T$$

where

lat_ϵ, lon_ϵ and alt_ϵ are the INS position errors

v_ϵ^N, v_ϵ^E, and v_ϵ^D are the INS velocity errors in the north, east and down directions respectively

ϵ_x, ϵ_y and ϵ_z are the INS tilt errors about the x, y and z directions respectively

h_ϵ^a is the aiding altitude error

a_ϵ is the vertical acceleration error

acc_ϵ^x, acc_ϵ^y and acc_ϵ^z are the INS accelerometer bias errors in the x, y and z axis respectively

g_ϵ^x, g_ϵ^y and g_ϵ^z are the INS gyroscope bias errors in the x, y and z axis respectively

TV_ϵ^x, TV_ϵ^y and TV_ϵ^z are the filter estimated temporal variations in the x, y and z components of the geomagnetic field respectively

System Dynamics.

The dynamics equation for the model used is a linearized function of the states. Because of the linearized dynamics in this system, the non-linear EKF dynamics function as shown in Equation 20 may be simplified to the linear dynamics function as defined in Equation 8. The dynamics matrix ($\mathbf{F}_k$) represents a linearized 15-state Pinson Error model augmented with three states to model the temporal variations in each axis of the magnetic field vector, and two states to model the barometer errors.

Variables that will appear in the dynamics matrix are following:

lat is the INS solution for latitude in radians

f_N, f_E, and f_D are the north, east, and down specific forces from the INS

v_n, v_e, and v_d are the north, east, and down velocities from the INS

τ_b is the barometer error time constant

k_1, k_2, and k_3 are barometer aiding constants used in the altitude aiding feedback loop

τ_a is the accelerometer bias error time constant

τ_g is the gyroscope bias error time constant

τ_{TV} is the temporal variation error time constant

r_e is the Earth's radius (6378135 m)

ω is the Earth's angular rate ($7.2921151467 \times 10^{-5}$ rad/sec)

The dynamics matrix is shown below and the full derivation of the Pinson error model used may be found in [39].

$$\mathbf{F} = \begin{bmatrix} \mathbf{F}_P & \mathbf{F}_C \\ \mathbf{0}_{9\times 11} & \mathbf{F}_s \end{bmatrix} \tag{29}$$

$\mathbf{F}_P$ is the 11×11 Pinson model block. $\mathbf{F}_C$ is the block containing INS rotation matrices and $\mathbf{F}_s$ represents the sensor and temporal variation bias error states.

$$\mathbf{F}_C = \begin{bmatrix} \mathbf{0}_{3\times3} & \mathbf{0}_{3\times3} & \mathbf{0}_{3\times3} \\ \mathbf{C}_{\mathbf{n}}^{\mathbf{b}} & \mathbf{0}_{3\times3} & \mathbf{0}_{3\times3} \\ \mathbf{0}_{3\times3} & \mathbf{C}_{\mathbf{n}}^{\mathbf{b}} & \mathbf{0}_{3\times3} \\ \mathbf{0}_{3\times3} & \mathbf{0}_{3\times3} & \mathbf{0}_{3\times3} \end{bmatrix}_{\mathbf{0}_{9\times9}} \tag{30}$$

$$\mathbf{F}_s = \begin{bmatrix} \frac{-1}{\tau_a} & 0 & 0 & 0 & 0 & 0 & 0 & 0 & 0 \\ 0 & \frac{-1}{\tau_a} & 0 & 0 & 0 & 0 & 0 & 0 & 0 \\ 0 & 0 & \frac{-1}{\tau_a} & 0 & 0 & 0 & 0 & 0 & 0 \\ 0 & 0 & 0 & \frac{-1}{\tau_g} & 0 & 0 & 0 & 0 & 0 \\ 0 & 0 & 0 & 0 & \frac{-1}{\tau_g} & 0 & 0 & 0 & 0 \\ 0 & 0 & 0 & 0 & 0 & \frac{-1}{\tau_g} & 0 & 0 & 0 \\ 0 & 0 & 0 & 0 & 0 & 0 & \frac{-1}{\tau_{TV}} & 0 & 0 \\ 0 & 0 & 0 & 0 & 0 & 0 & 0 & \frac{-1}{\tau_{TV}} & 0 \\ 0 & 0 & 0 & 0 & 0 & 0 & 0 & 0 & \frac{-1}{\tau_{TV}} \end{bmatrix} \tag{31}$$

$$\mathbf{F}_P = \begin{bmatrix} \mathbf{F}_{P1} & \mathbf{F}_{P2} \end{bmatrix}_{\mathbf{0}_{11\times11}} \tag{32}$$

$$\mathbf{F}_{P1} = \begin{bmatrix} 0 & 0 & \frac{-v_n}{r_e^2} & \frac{1}{r_e} & 0 \\ \frac{v_e \tan(lat)}{r_e \cos(lat)} & 0 & \frac{-v_e}{r_e^2 \cos(lat)} & 0 & \frac{1}{r_e \cos(lat)} \\ 0 & 0 & -k_1 & 0 & 0 \\ -v_e(2\omega \cos(lat) + \frac{v_e}{r_e(\cos(lat))^2}) & 0 & \frac{v_e^2 \tan(lat) - v_n v_d}{r_e^2} & \frac{v_d}{r_e} & -2(\omega \sin(lat) + \frac{v_e \tan(lat)}{r_e}) \\ 2\omega(v_n \cos(lat) - v_d \sin(lat)) + \frac{v_n v_e}{r_e(\cos(lat))^2} & 0 & \frac{-v_e(v_n \tan(lat) + v_d)}{r_e^2} & 2\omega \sin(lat) + \frac{v_e \tan(lat)}{r_e} & \frac{v_n \tan(lat) + v_d}{r_e} \\ 2\omega v_e \sin(lat) & 0 & \frac{v_n^2 + v_e^2}{r_e^2 + k_2} & \frac{-2v_n}{r_e} & -2(\omega \cos(lat) - \frac{v_e}{r_e}) \\ -\omega \sin(lat) & 0 & \frac{-v_e^2}{r_e^2} & 0 & \frac{1}{r_e} \\ 0 & 0 & \frac{v_n}{r_e^2} & \frac{-1}{r_e} & 0 \\ -\omega \cos(lat) - \frac{v_e}{r_e(\cos(lat))^2} & 0 & \frac{v_e \tan(lat)}{r_e^2} & 0 & \frac{-\tan(lat)}{r_e} \\ 0 & 0 & 0 & 0 & 0 \\ 0 & 0 & k_3 & 0 & 0 \end{bmatrix} \tag{33}$$

$$\mathbf{F}_{P2} = \begin{bmatrix} 0 & 0 & 0 & 0 & 0 & 0 \\ 0 & 0 & 0 & 0 & 0 & 0 \\ -1 & 0 & 0 & 0 & k_1 & 0 \\ \frac{v_n}{r_e} & 0 & -f_D & f_E & 0 & 0 \\ 2\omega\cos(lat) + \frac{v_e}{r_e} & f_D & 0 & -f_N & 0 & 0 \\ 0 & -f_E & f_N & 0 & -k_2 & 1 \\ 0 & 0 & -\omega\sin(lat) - \frac{v_e\tan(lat)}{r_e} & \frac{v_n}{r_e} & 0 & 0 \\ 0 & \omega\sin(lat) + \frac{v_e\tan(lat)}{r_e} & 0 & \omega\cos(lat) + \frac{v_e}{r_e} & 0 & 0 \\ 0 & \frac{-v_n}{r_e} & -\omega\cos(lat) - \frac{v_e}{r_e} & 0 & 0 & 0 \\ 0 & 0 & 0 & 0 & \frac{-1}{\tau_b} & 0 \\ 0 & 0 & 0 & 0 & -k_3 & 0 \end{bmatrix} \tag{34}$$

The INS sensor errors and temporal variations are modeled as First Order Gauss Markov (FOGM) processes. A FOGM process $X(t)$ has an exponential autocorrelation function that is defined in Equation 35[6].

$$R_X(\tau) = \sigma^2 e^{-\beta|\tau|} \tag{35}$$

where σ and τ are the standard deviation and time constant of the process respectively.

The dynamics noise for this model is defined as

$$E[\mathbf{w}\mathbf{w}^T] = \mathbf{Q}$$

$$\mathbf{Q} = diag([\mathbf{0}_{1\times3} \quad \mathbf{VRW}_{1\times3} \quad \mathbf{ARW}_{1\times3} \quad B \quad 0 \quad \mathbf{A}_{1\times3} \quad \mathbf{G}_{1\times3} \quad \mathbf{T}_{1\times3}])_{20\times20} \tag{36}$$

$$B = \frac{2\sigma_b^2}{\tau_b} \tag{37}$$

$$A = \frac{2\sigma_a^2}{\tau_a} \tag{38}$$

$$G = \frac{2\sigma_g^2}{\tau_g} \tag{39}$$

$$T = \frac{2\sigma_{TV}^2}{\tau_{TV}} \tag{40}$$

where

VRW is the noise strength of the velocity random walk in the INS

ARW is the noise strength of the angular random walk in the INS

σ_b is the standard deviation of the barometer error

σ_a is the standard deviation of the accelerometer error

σ_g is the standard deviation of the gyroscope error

σ_{TV} is the standard deviation of the temporal variations

B, $\mathbf{A}$, $\mathbf{G}$, and $\mathbf{T}$ are the driving noise strengths of the barometer, accelerometer, gyroscope, and temporal variation error states respectively

For simplicity, the VRW, the ARW, the accelerometer, the gyroscope, and the temporal variations are assumed to have the same driving noise strength in each axis. This is why each of these appears three times in $\mathbf{Q}$.

Measurement Function.

The measurement function is a non-linear function of the states as well as inputs from the INS. The measurement function used is the standard EKF measurement function as shown in Equation 41. Using an EKF allows for the linearization of the measurement function about the propagated estimate of each state's trajectory.

Equation 41 shows the measurement model for the body-frame measurements.

$$\mathbf{z}_k = \mathbf{h}[\mathbf{x_k}] + \mathbf{v_k} \tag{41}$$

$$\mathbf{z}_k = \begin{bmatrix} B_{x,k} \\ B_{y,k} \\ B_{z,k} \end{bmatrix}_{Body\,Frame} \tag{42}$$

The measurement function, $\mathbf{h}$, defines how the states relate to the magnetic anomaly field vector measurements and performs two main functions: map-matching and coordinate frame transformation. The coordinate-frame transformation is defined as a rotation from the nav frame to the body frame.

The measurement function matches the INS reading of latitude and longitude (lat_{INS} and lon_{INS}) combined with the states lat_ϵ and lon_ϵ at time t_k to the map of each vector component of the magnetic anomaly field. This is done using the mapping functions g_x, g_y, and g_z. The mapping functions return the full vector measurement that we expect to see at the filter estimated location. We also expect to see the

effects of the temporal variations in the measurement, so the three TV_ϵ states are added to their respective vector components. This expected measurement is in the world frame, because the filter matches the location to nav-frame anomaly field vector maps. The nav-frame expected measurement must be rotated to the same frame as the actual vector sensor measurement. The expected measurement is rotated using the rotation matrix $\mathbf{C_n^b}$, which is the rotation matrix from the INS ($\mathbf{C_{n,INS}^b}$) corrected using the tilt error states ϵ_x, ϵ_y, and ϵ_z.

$$\mathbf{h}[\mathbf{x}_k] = \begin{bmatrix} h_{x,k} \\ h_{y,k} \\ h_{z,k} \end{bmatrix} = \mathbf{C_{n,k}^b} \begin{bmatrix} g_x(lat_{INS,k} + lat_{\epsilon,k}, lon_{INS,k} + lon_{\epsilon,k}) + TV_{\epsilon,k}^x \\ g_y(lat_{INS,k} + lat_{\epsilon,k}, lon_{INS,k} + lon_{\epsilon,k}) + TV_{\epsilon,k}^y \\ g_z(lat_{INS,k} + lat_{\epsilon,k}, lon_{INS,k} + lon_{\epsilon,k}) + TV_{\epsilon,k}^z \end{bmatrix} \tag{43}$$

$\mathbf{C_n^b}$ is the corrected rotation matrix calculated by applying a small angle correction to the rotation matrix from the INS ($\mathbf{C_{n,INS}^b}$). The angle matrix ϵ is used to solve for the rotation matrix, $\mathbf{A}$, that satisfies $\mathbf{C_n^b} = \mathbf{C_{n,INS}^b A}$.

The components of ϵ at time k are the estimated tilt error angles, ϵ_x, ϵ_y, and ϵ_z. The magnitude of ϵ is given by

$$\epsilon = \sqrt{\epsilon_x^2 + \epsilon_y^2 + \epsilon_z^2} \tag{44}$$

and

$$[\epsilon]_\times = \begin{bmatrix} 0 & -\epsilon_z & \epsilon_y \\ \epsilon_z & 0 & -\epsilon_x \\ -\epsilon_y & \epsilon_x & 0 \end{bmatrix} \tag{45}$$

$\mathbf{A}$ is expressed in terms of the angle vector ϵ in Equation 46 and a full derivation of this process may be found in [39].

$$\mathbf{A} = \mathbf{I_{3\times 3}} - \frac{\sin(\epsilon)}{\epsilon}[\epsilon]_\times + \frac{1 - \cos\epsilon}{\epsilon^2}[\epsilon]_\times{}^2 \tag{46}$$

Equation 47 applies the correction to the INS' rotation matrix.

$$\mathbf{C_n^b} = \mathbf{C_{n,INS}^b A} \tag{47}$$

The measurement Jacobian is defined as:

$$\mathbf{H}_k \triangleq \frac{\partial \mathbf{h}(\mathbf{x}, k)}{\partial \mathbf{x}}\Big|_{\mathbf{x}=\hat{\mathbf{x}}_\mathbf{k}^-} \tag{48}$$

The partial derivative of each measurement with respect to every state must be calculated. The only states that show up in the measurement function are the horizontal position states ($lat_{\epsilon,k}$, and $lon_{\epsilon,k}$) within the mapping function, the tilt error states (ϵ_x, ϵ_y, and ϵ_z) within the small angle correction equation, and the temporal variation states ($TV^x_{\epsilon,k}$, $TV^y_{\epsilon,k}$, and $TV^z_{\epsilon,k}$). The partial derivatives in the columns corresponding to the states that are not listed are zeros.

$$\mathbf{H}_k = \begin{bmatrix} \frac{\partial h_{x,k}}{\partial lat_{\epsilon,k}} & \frac{\partial h_{x,k}}{\partial lon_{\epsilon,k}} & \cdots & \frac{\partial h_{x,k}}{\partial TV^z_{\epsilon,k}} \\ \frac{\partial h_{y,k}}{\partial lat_{\epsilon,k}} & \frac{\partial h_{y,k}}{\partial lon_{\epsilon,k}} & \cdots & \frac{\partial h_{x,k}}{\partial TV^z_{\epsilon,k}} \\ \frac{\partial h_{z,k}}{\partial lat_{\epsilon,k}} & \frac{\partial h_{z,k}}{\partial lon_{\epsilon,k}} & \cdots & \frac{\partial h_{z,k}}{\partial TV^z_{\epsilon,k}} \end{bmatrix}_{3\times 20} \tag{49}$$

$$= \begin{bmatrix} \mathbf{H}_{lat_\epsilon} & \mathbf{H}_{lon_\epsilon} & \mathbf{0}_{3\times 4} & \mathbf{H}_{\epsilon_x} & \mathbf{H}_{\epsilon_y} & \mathbf{H}_{\epsilon_z} & \mathbf{0}_{3\times 8} & \mathbf{H}_{TV} \end{bmatrix}_{3\times 20} \tag{50}$$

Equation 51 and 52 show how the first and second column of the measurement Jacobian were calculated. These columns contain the partial derivatives of $\mathbf{h}$ with respect to $lat_{\epsilon,k}$ and $lon_{\epsilon,k}$ respectively. There is no closed form solution for the spatial derivative of the maps within the $\boldsymbol{f}$ function, so they are obtained by finite

differencing.

$$\mathbf{H}_{lat_\epsilon} = \begin{bmatrix} \frac{\partial h_{x,k}}{\partial lat_{\epsilon,k}} \\ \frac{\partial h_{y,k}}{\partial lat_{\epsilon,k}} \\ \frac{\partial h_{z,k}}{\partial lat_{\epsilon,k}} \end{bmatrix} = \mathbf{C}^{\mathbf{b}}_{\mathbf{n,k}} \begin{bmatrix} g_x(lat_k + \frac{\delta lat}{2}, lon_k) - g_x(lat_k - \frac{\delta lat}{2}, lon_k)) \\ g_y(lat_k + \frac{\delta lat}{2}, lon_k) - g_y(lat_k - \frac{\delta lat}{2}, lon_k)) \\ g_z(lat_k + \frac{\delta lat}{2}, lon_k) - g_z(lat_k - \frac{\delta lat}{2}, lon_k)) \end{bmatrix} \tag{51}$$

$$\mathbf{H}_{lon_\epsilon} = \begin{bmatrix} \frac{\partial h_{x,k}}{\partial lon_{\epsilon,k}} \\ \frac{\partial h_{y,k}}{\partial lon_{\epsilon,k}} \\ \frac{\partial h_{z,k}}{\partial lon_{\epsilon,k}} \end{bmatrix} = \mathbf{C}^{\mathbf{b}}_{\mathbf{n,k}} \begin{bmatrix} g_x(lat_k, lon_k + \frac{\delta lon}{2}) - g_x(lat_k, lon_k - \frac{\delta lon}{2})) \\ g_y(lat_k, lon_k + \frac{\delta lon}{2}) - g_y(lat_k, lon_k - \frac{\delta lon}{2})) \\ g_z(lat_k, lon_k + \frac{\delta lon}{2}) - g_z(lat_k, lon_k - \frac{\delta lon}{2})) \end{bmatrix} \tag{52}$$

where

$$lat_k = lat_{INS,k} + lat_{\epsilon,k} \tag{53}$$

$$lon_k = lon_{INS,k} + lon_{\epsilon,k} \tag{54}$$

The variables δlat and δlon can be chosen to be any small number. For the results presented in this research, a δlat and δlon of 0.5 m (converted to degrees latitude and degrees longitude respectively) is used.

In Equation 50, the columns containing the partial derivatives of $\mathbf{h}$ with respect to the tilt states have a closed form solution. Each column was calculated separately, so will be presented below one column at a time. The column corresponding to the

ϵ_x state is shown in Equation 55.

$$\mathbf{H}_{\epsilon_x} = \begin{bmatrix} \frac{\partial h_{x,k}}{\partial \epsilon_{x,k}} \\ \frac{\partial h_{y,k}}{\partial \epsilon_{x,k}} \\ \frac{\partial h_{z,k}}{\partial \epsilon_{x,k}} \end{bmatrix} = \frac{\partial}{\partial \epsilon_{x,k}} \left(\mathbf{C}^{\mathbf{b}}_{\mathbf{n,INS}} \mathbf{A}(\epsilon_{\mathbf{k}}) \begin{bmatrix} g_x(lat_k, lon_k) + TV^x_{\epsilon,k} \\ g_y(lat_k, lon_k) + TV^y_{\epsilon,k} \\ g_z(lat_k, lon_k) TV^z_{\epsilon,k} \end{bmatrix} \right) \tag{55}$$

$$= \mathbf{C}^{\mathbf{b}}_{\mathbf{n,INS}} \left(\frac{\partial \mathbf{A}(\epsilon_{\mathbf{k}})}{\partial \epsilon_{x,k}} \right) \begin{bmatrix} g_x(lat_k, lon_k) + TV^x_{\epsilon,k} \\ g_y(lat_k, lon_k) + TV^y_{\epsilon,k} \\ g_z(lat_k, lon_k) + TV^z_{\epsilon,k} \end{bmatrix} \tag{56}$$

In order to differentiate the measurement function with respect to any of the tilt error states, the matrix $\mathbf{C}^{\mathbf{b}}_{\mathbf{n}}$ in Equation 43 is replaced with $\mathbf{C}^{\mathbf{b}}_{\mathbf{n,INS}}\mathbf{A}$ as shown in Equation 47, because $\mathbf{A}$ is a function of these states. In order to calculate $\frac{\partial \mathbf{A_k}}{\partial \epsilon_{x,k}}$ from Equation 55, $\mathbf{A}$ was calculated symbolically in terms of the tilt error states as shown in Equations 44 through 46. $\mathbf{A}$ was then differentiated with respect to $\epsilon_{x,k}$ using a symbolic toolbox.

The same process is followed to obtain the columns corresponding to the $\epsilon_{y,k}$ and $\epsilon_{z,k}$ states.

$$\mathbf{H}_{\epsilon_y} = \begin{bmatrix} \frac{\partial h_{x,k}}{\partial \epsilon_{y,k}} \\ \frac{\partial h_{y,k}}{\partial \epsilon_{y,k}} \\ \frac{\partial h_{z,k}}{\partial \epsilon_{y,k}} \end{bmatrix} = \mathbf{C}^{\mathbf{b}}_{\mathbf{n,INS}} \frac{\partial \mathbf{A_k}}{\partial \epsilon_{y,k}} \begin{bmatrix} g_x(lat_k, lon_k) + TV^x_{\epsilon,k} \\ g_y(lat_k, lon_k) + TV^y_{\epsilon,k} \\ g_z(lat_k, lon_k) + TV^z_{\epsilon,k} \end{bmatrix} \tag{57}$$

$$\mathbf{H}_{\epsilon_z} = \begin{bmatrix} \frac{\partial h_{x,k}}{\partial \epsilon_{z,k}} \\ \frac{\partial h_{y,k}}{\partial \epsilon_{z,k}} \\ \frac{\partial h_{z,k}}{\partial \epsilon_{z,k}} \end{bmatrix} = \mathbf{C}^{\mathbf{b}}_{\mathbf{n,INS}} \frac{\partial \mathbf{A_k}}{\partial \epsilon_{z,k}} \begin{bmatrix} g_x(lat_k, lon_k) + TV^x_{\epsilon,k} \\ g_y(lat_k, lon_k) + TV^y_{\epsilon,k} \\ g_z(lat_k, lon_k) + TV^z_{\epsilon,k} \end{bmatrix} \tag{58}$$

$$\tag{59}$$

The columns of the measurement Jacobian corresponding to the three temporal vari-

ation states are shown in Equation 60.

$$\mathbf{H}_{TV} = \begin{bmatrix} \frac{\partial h_{x,k}}{\partial TV^x_{\epsilon,k}} & \frac{\partial h_{x,k}}{\partial TV^y_{\epsilon,k}} & \frac{\partial h_{x,k}}{\partial TV^z_{\epsilon,k}} \\ \frac{\partial h_{y,k}}{\partial TV^x_{\epsilon,k}} & \frac{\partial h_{y,k}}{\partial TV^y_{\epsilon,k}} & \frac{\partial h_{y,k}}{\partial \epsilon,k^z} \\ \frac{\partial h_{z,k}}{\partial TV^x_{\epsilon,k}} & \frac{\partial h_{z,k}}{\partial TV^y_{\epsilon,k}} & \frac{\partial h_{z,k}}{\partial TV^z_{\epsilon,k}} \end{bmatrix} = \mathbf{C}^{\mathbf{b}}_{\mathbf{n},\mathbf{k}} \, \mathbf{I}_{\mathbf{3}\times\mathbf{3}} \tag{60}$$

All of these columns are combined into the complete measurement Jacobian, $\mathbf{H}_k$, as in Equation 50 to be evaluated each time step, k, given the current state estimates.

Finally, the covariance of the white noise measurement error, $\mathbf{v}$, is given by:

$$E[\mathbf{v}\mathbf{v}^T] = \mathbf{R}_{3\times3} \tag{61}$$

where the measurement noise strength for each measurement in $\mathbf{z}_k$ is assumed to be equivalent.

3.2 Navigation Filter Using Tensor Measurements

The second navigation system will use tensor measurements of the anomaly field as well as inputs from an INS to estimate position and attitude of the vehicle. In this section, the filter states will be introduced as well as the dynamics model and measurement function.

Filter States.

Using tensor measurements allows for simplification of the dynamics model. The temporal variations were not included in the dynamics model because the gradient sensors used to measure the full tensor nearly eliminate any temporal and regional affects on the measurements.

The tensor magnetic navigation filter estimates seventeen states as opposed to the

vector magnetic navigation filter's twenty states. The states estimate INS errors and are equivalent to the first 17 states of the vector measurement state vector in section 3.1. The state vector is

$$\mathbf{x}_k = [lat_\epsilon \quad lon_\epsilon \quad alt_\epsilon \quad v_\epsilon^N \quad v_\epsilon^E \quad v_\epsilon^D \quad \epsilon_x \quad \epsilon_y \quad \epsilon_z \quad h_\epsilon^a \\ a_\epsilon \quad acc_\epsilon^x \quad acc_\epsilon^y \quad acc_\epsilon^z \quad g_\epsilon^x \quad g_\epsilon^y \quad g_\epsilon^z]^T$$

System Dynamics.

The same dynamics model is used in the tensor measurement filter with the exception of the last three rows and columns of $\mathbf{F}$ in Equation 29, which correspond to the temporal variation states. These rows and columns are omitted in the tensor measurement dynamics matrix.

As with the vector navigation model, the driving noise of the sensors are modeled as FOGM processes. The dynamics driving noise is the same as in Equation 36 with the exception of the last three rows and columns, which are omitted because the tensor measurement filter does not model the temporal variations.

Measurement Function.

The measurement function when using tensor measurements is of the same form as the EKF in Equation 21. The measurement vector $\mathbf{z}_k$ is shown in Equation 62.

$$\mathbf{z}_k = \begin{bmatrix} B_{xx,k} \\ B_{yx,k} \\ B_{zx,k} \\ B_{yy,k} \\ B_{zy,k} \end{bmatrix}_{Body\ Frame} \tag{62}$$

The measurement vector contains the five unique tensor components needed to completely describe the tensor. The filter requires the tensor measurements to be in full 3×3 matrix form at some points and 5×1 vector form at others. To deal with this transformation, the function M is defined in Equation 63. This function transforms a vector of size (5×1) to a symmetric, traceless matrix of size (3×3).

$$\mathbf{u}_T = M(\mathbf{u}_V) \tag{63}$$

where

$$\mathbf{u}_V = \begin{bmatrix} u_{11} \\ u_{12} \\ u_{13} \\ u_{22} \\ u_{23} \end{bmatrix} \tag{64}$$

$$\mathbf{u}_T = \begin{bmatrix} u_{11} & u_{12} & u_{13} \\ u_{12} & u_{22} & u_{23} \\ u_{13} & u_{23} & -(u_{11} + u_{22}) \end{bmatrix} \tag{65}$$

The inverse (M') transforms a symmetric, traceless matrix of size (3×3) to a vector of size (5×1) containing its five unique components as shown in Equation 66.

$$\mathbf{u}_V = M'(\mathbf{u}_T) \tag{66}$$

where

$$\mathbf{u}_T = \begin{bmatrix} u_{11} & u_{12} & u_{13} \\ u_{21} & u_{22} & u_{23} \\ u_{31} & u_{32} & u_{33} \end{bmatrix} \tag{67}$$

$$\mathbf{u}_V = \begin{bmatrix} u_{11} \\ u_{12} \\ u_{13} \\ u_{22} \\ u_{23} \end{bmatrix} \tag{68}$$

As with the vector measurement function, the tensor measurement function performs the map-matching and coordinate frame transformation required. The measurement function matches each of the five unique tensor measurements to their respective maps using the mapping functions g_{xx}, g_{yx}, $g_{zx}\, g_{yy}$, and g_{zy}. These five mapping functions return the full tensor measurement that we expect to see at the filter estimated location in the nav frame. Unlike the vector measurements, the effect of the temporal variations in the tensor measurements is negligible because the majority of their effects are canceled out when the spatial gradient is measured. Thus, we do not need to add the estimated effects of temporal variations into our expected measurement. The expected measurement returned from the mapping function is in the nav frame. It must be rotated into the same frame as the actual tensor sensor measurement as shown in Equation 7. The expected measurement is rotated using the rotation matrix $\mathbf{C}_{\mathbf{n}}^{\mathbf{b}}$ which is calculated by using Equations 44 through 47. Equation 73 shows the full

tensor measurement function.

$$lat_k = lat_{INS,k} + lat_{\epsilon,k} \tag{69}$$

$$lon_k = lon_{INS,k} + lon_{\epsilon,k} \tag{70}$$

$$\mathbf{g}_V(lat_k, lon_k) = \begin{bmatrix} g_{xx}(lat_k, lon_k) \\ g_{yx}(lat_k, lon_k) \\ g_{zx}(lat_k, lon_k) \\ g_{yy}(lat_k, lon_k) \\ g_{zy}(lat_k, lon_k) \end{bmatrix} \tag{71}$$

$$\mathbf{g}_T(lat_k, lon_k) = M(\mathbf{g}_V(lat_k, lon_k)) \tag{72}$$

$$\mathbf{h}[\mathbf{x}_k] = \mathbf{h}_k = \begin{bmatrix} h_{xx,k} \\ h_{yx,k} \\ h_{zx,k} \\ h_{yy,k} \\ h_{zy,k} \end{bmatrix} = M'(\mathbf{C}^{\mathbf{b}}_{\mathbf{n},\mathbf{k}}\, \mathbf{g}_T(lat_k, lon_k)\, \mathbf{C}^{\mathbf{b}}_{\mathbf{n},\mathbf{k}}{}^T) \tag{73}$$

The only states that show up in the measurement function used in this case are the horizontal position states ($lat_{\epsilon,k}$ and $lon_{\epsilon,k}$) within the mapping functions and the tilt error states (ϵ_x, ϵ_y, and ϵ_z) within the small angle correction equation. The partial

derivatives in the columns corresponding to states that are not listed are zeros.

$$\mathbf{H}_k = \begin{bmatrix} \frac{\partial h_{xx,k}}{\partial lat_{\epsilon,k}} & \frac{\partial h_{xx,k}}{\partial lon_{\epsilon,k}} & \cdots & \frac{\partial h_{xx,k}}{\partial g^z_{\epsilon,k}} \\ \frac{\partial h_{yx,k}}{\partial lat_{\epsilon,k}} & \frac{\partial h_{yx,k}}{\partial lon_{\epsilon,k}} & \cdots & \frac{\partial h_{yx,k}}{\partial g^z_{\epsilon,k}} \\ \vdots & \vdots & \ddots & \vdots \\ \frac{\partial h_{zy,k}}{\partial lat_{\epsilon,k}} & \frac{\partial h_{zy,k}}{\partial lon_{\epsilon,k}} & \cdots & \frac{\partial h_{zy,k}}{\partial g^z_{\epsilon,k}} \end{bmatrix}_{5\times 17} \tag{74}$$

$$= \begin{bmatrix} \mathbf{H}_{lat_\epsilon} & \mathbf{H}_{lon_\epsilon} & \mathbf{0}_{3\times 4} & \mathbf{H}_{\epsilon_x} & \mathbf{H}_{\epsilon_y} & \mathbf{H}_{\epsilon_z} & \mathbf{0}_{3\times 8} \end{bmatrix}_{5\times 17} \tag{75}$$

$\mathbf{H}_{lat_\epsilon}$ and $\mathbf{H}_{lon_\epsilon}$ are calculated using finite differencing as with the vector measurement Jacobian shown in Equations 51 and 52.

$\mathbf{H}_{\epsilon_x}$, $\mathbf{H}_{\epsilon_y}$, and $\mathbf{H}_{\epsilon_z}$ are calculated using the product rule, which is defined in Equation 76, where q and w are arbitrary differentiable functions. Equations 78 through 80 show the substitutions needed to find $\mathbf{H}_{\epsilon_x}$ using the product rule.

$$\frac{\partial(q\,w)}{\partial \epsilon_x} = \frac{\partial q}{\partial \epsilon_x} w + q \frac{\partial w}{\partial \epsilon_x} \tag{76}$$

$$\mathbf{H}_{\epsilon_x} = \frac{\partial \mathbf{h}}{\partial \epsilon_x} = M'\Big(\frac{\partial(q\,w)}{\partial \epsilon_x}\Big) \tag{77}$$

$$qw = M(\mathbf{h}_k) = \mathbf{C}^{\mathbf{b}}_{\mathbf{n},\mathbf{k}} \mathbf{g}_T(lat_k, lon_k)\, {\mathbf{C}^{\mathbf{b}}_{\mathbf{n},\mathbf{k}}}^T \tag{78}$$

$$q = \mathbf{C}^{\mathbf{b}}_{\mathbf{n},\mathbf{k}} = \mathbf{C}^{\mathbf{b}}_{\mathbf{n},\mathbf{INS}} \mathbf{A}_k \tag{79}$$

$$w = \mathbf{g}_T(lat_k, lon_k)\, {\mathbf{C}^{\mathbf{b}}_{\mathbf{n},\mathbf{k}}}^T = \mathbf{g}_T(lat_k, lon_k)\, (\mathbf{C}^{\mathbf{b}}_{\mathbf{n},\mathbf{INS}} \mathbf{A}_k)^T \tag{80}$$

The functions q and w are then differentiated with respect to ϵ_x in Equations 81 and 82 respectively and substituted back into Equation 76 to get the final $\mathbf{H}_{\epsilon_x}$ in Equation

84.

$$\frac{\partial q}{\partial \epsilon_x} = \mathbf{C}^{\mathbf{b}}_{\mathbf{n},\mathbf{INS}} \frac{\partial \mathbf{A}_k}{\partial \epsilon_x} \tag{81}$$

$$\frac{\partial w}{\partial \epsilon_x} = \mathbf{g}_T(lat_k, lon_k) \left(\mathbf{C}^{\mathbf{b}}_{\mathbf{n},\mathbf{INS}} \frac{\partial \mathbf{A}_k}{\partial \epsilon_x} \right)^T \tag{82}$$

$$\frac{\partial (q\, w)}{\partial \epsilon_x} = \mathbf{C}^{\mathbf{b}}_{\mathbf{n},\mathbf{INS}} \frac{\partial \mathbf{A}_k}{\partial \epsilon_x} \mathbf{g}_T(lat_k, lon_k) \left(\mathbf{C}^{\mathbf{b}}_{\mathbf{n},\mathbf{INS}} \mathbf{A}_k \right)^T + \mathbf{C}^{\mathbf{b}}_{\mathbf{n},\mathbf{INS}} \mathbf{A}_k \mathbf{g}_T(lat_k, lon_k) \left(\mathbf{C}^{\mathbf{b}}_{\mathbf{n},\mathbf{INS}} \frac{\partial \mathbf{A}_k}{\partial \epsilon_x} \right)^T \tag{83}$$

$$\mathbf{H}_{\epsilon_x} = M' \Big(\frac{\partial (q\, w)}{\partial \epsilon_x} \Big) \tag{84}$$

$\mathbf{H}_{\epsilon_y}$ and $\mathbf{H}_{\epsilon_z}$ are calculated using the same process:

$$\frac{\partial (q\, w)}{\partial \epsilon_y} = \mathbf{C}^{\mathbf{b}}_{\mathbf{n},\mathbf{INS}} \frac{\partial \mathbf{A}_k}{\partial \epsilon_y} \mathbf{g}_T(lat_k, lon_k) \left(\mathbf{C}^{\mathbf{b}}_{\mathbf{n},\mathbf{INS}} \mathbf{A}_k \right)^T + \mathbf{C}^{\mathbf{b}}_{\mathbf{n},\mathbf{INS}} \mathbf{A}_k \mathbf{g}_T(lat_k, lon_k) \left(\mathbf{C}^{\mathbf{b}}_{\mathbf{n},\mathbf{INS}} \frac{\partial \mathbf{A}_k}{\partial \epsilon_y} \right)^T \tag{85}$$

$$\mathbf{H}_{\epsilon_y} = M' \Big(\frac{\partial (q\, w)}{\partial \epsilon_y} \Big) \tag{86}$$

$$\frac{\partial (q\, w)}{\partial \epsilon_z} = \mathbf{C}^{\mathbf{b}}_{\mathbf{n},\mathbf{INS}} \frac{\partial \mathbf{A}_k}{\partial \epsilon_z} \mathbf{g}_T(lat_k, lon_k) \left(\mathbf{C}^{\mathbf{b}}_{\mathbf{n},\mathbf{INS}} \mathbf{A}_k \right)^T + \mathbf{C}^{\mathbf{b}}_{\mathbf{n},\mathbf{INS}} \mathbf{A}_k \mathbf{g}_T(lat_k, lon_k) \left(\mathbf{C}^{\mathbf{b}}_{\mathbf{n},\mathbf{INS}} \frac{\partial \mathbf{A}_k}{\partial \epsilon_z} \right)^T \tag{87}$$

$$\mathbf{H}_{\epsilon_z} = M' \Big(\frac{\partial (q\, w)}{\partial \epsilon_z} \Big) \tag{88}$$

$\frac{\partial \mathbf{A}_k}{\partial \epsilon_x}$, $\frac{\partial \mathbf{A}_k}{\partial \epsilon_y}$, and $\frac{\partial \mathbf{A}_k}{\partial \epsilon_z}$ are calculated with a symbolic toolbox.

All of these columns are combined into the the complete measurement Jacobian, $\mathbf{H}_k$, as in Equation 75, to be evaluated at each time step, k, given the current state estimates.

The covariance of the white noise measurement error, $\mathbf{v}$, is following:

$$E[\mathbf{v}\mathbf{v}^T] = \mathbf{R}_{5\times 5} \tag{89}$$

where the measurement noise strength for each measurement in $\mathbf{z}_k$ is assumed to be equivalent.

3.3 Truth Trajectories

Four different truth trajectories were used in the simulations. The different trajectories are used to demonstrate the difference in filter performance with varying vehicle velocities and positions. The actual boat trajectory used is characterized by low velocities and the actual aerial trajectory is characterized by high velocities.

Additionally, the geographic location of the trajectory may affect filter performance. For example, the frequency content of the magnetic anomaly field at sea-level over deep seas is generally much lower than over shallow seas (e.g. over the continental shelf off the western coast of the U.S.) and may lead to degraded filter performance. To investigate the effect of geographic location on the navigation filter, the latitude and longitude of the truth trajectories may be shifted to alternate geographic locations. This is possible because actual vector and tensor magnetic field measurements were not recorded during the course of the trajectories, so the flight and ship path are not tied to the actual geographic location.

The trajectories included in the simulation are following:

1. Actual 1 hour boat trajectory directly off the western coast of the U.S.
2. Actual 1 hour aerial trajectory directly off the western coast of the U.S.
3. Actual 1 hour aerial trajectory over the continental United States
4. Actual 25 hour boat trajectory over the deep sea

Figure 12 shows the geographic location of the four trajectories. Trajectory 1 and Trajectory 4 are both mapped by the orange path as Trajectory 1 is equivalent to the first hour of Trajectory 4.

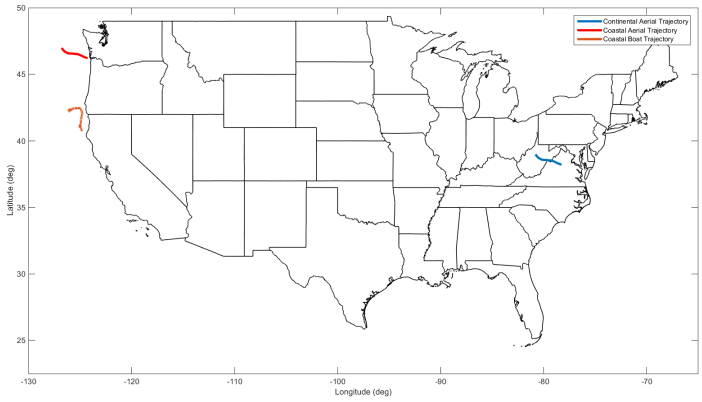

Figure 12. Map of Trajectories

The GPS position solution paired with the on-board sensors was used to generate the truth trajectories. While the truth data is not directly available to the navigation filter, it is used to calculate the amount of error present in the navigation filter solution and analyze overall filter performance. It is also used to generate simulated magnetic vector and tensor measurements as well as simulated INS solutions.

3.4 Generating Vector and Tensor Maps

The maps used for a majority of this research are segments from the North American Magnetic Anomaly Database compiled by the U.S. Geological Survey (USGS). This is a database of aerial magnetic data collected and pieced together over the continental United States and extending slightly over both coasts to cover shallow seas. [1]. Figure 13 shows the scalar anomaly field content collected over the entire North American continent.

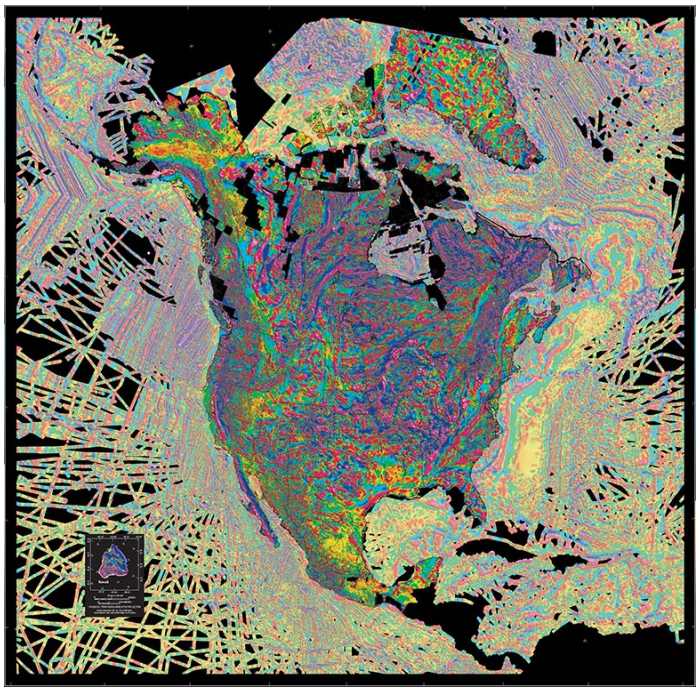

Figure 13. Scalar Magnetic Anomaly Content from NAMAD Data [1]

The following figure shows a contour map of the scalar magnetic anomaly map used for the trajectories directly off the western coast of the United States.

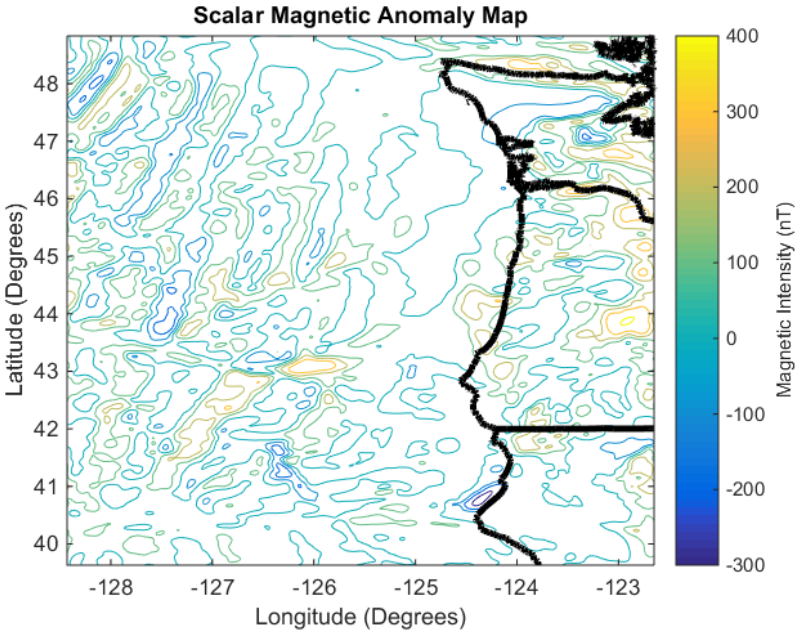

Figure 14. Scalar Magnetic Intensity Contour Map from NAMAD Data

A Fourier method was used as in [5] to transform the scalar anomaly field into the vector components of the anomaly field. The individual directional components were found using the following equations:

$$\mathcal{F}[B_x] = \mathcal{F}[\Delta T]\mathcal{F}[\psi_x] \tag{90}$$

$$\mathcal{F}[B_y] = \mathcal{F}[\Delta T]\mathcal{F}[\psi_y] \tag{91}$$

$$\mathcal{F}[B_z] = \mathcal{F}[\Delta T]\mathcal{F}[\psi_z] \tag{92}$$

where

$$\mathcal{F}[\psi_x] = \frac{i\,k_x}{|k|\hat{f}_z + i(k_x\hat{f}_x + k_y\hat{f}_y)} \tag{93}$$

$$\mathcal{F}[\psi_y] = \frac{i\,k_y}{|k|\hat{f}_z + i(k_x\hat{f}_x + k_y\hat{f}_y)} \tag{94}$$

$$\mathcal{F}[\psi_z] = \frac{|k|}{|k|\hat{f}_z + i(k_x\hat{f}_x + k_y\hat{f}_y)} \tag{95}$$

$$\Delta T = \text{total field anomaly measured in an ambient field}$$

$$(\hat{f}_x, \hat{f}_y, \hat{f}_z) = \text{unit vector in the direction of the ambient field}$$

$$\hat{f}_x = \cos(I)\cos(D) \tag{96}$$

$$\hat{f}_y = \cos(I)\sin(D) \tag{97}$$

$$\hat{f}_z = \sin(I) \tag{98}$$

where $\mathcal{F}$ denotes the Fourier transform, k, k_x, and k_y are the wave numbers and I and D are the inclination and declination angles from the IGRF.

The inverse Fourier Transform of Equations 90 through 92 gives the individual vector component maps used in the vector measurement navigation filter. These maps contain magnetic data in nT.

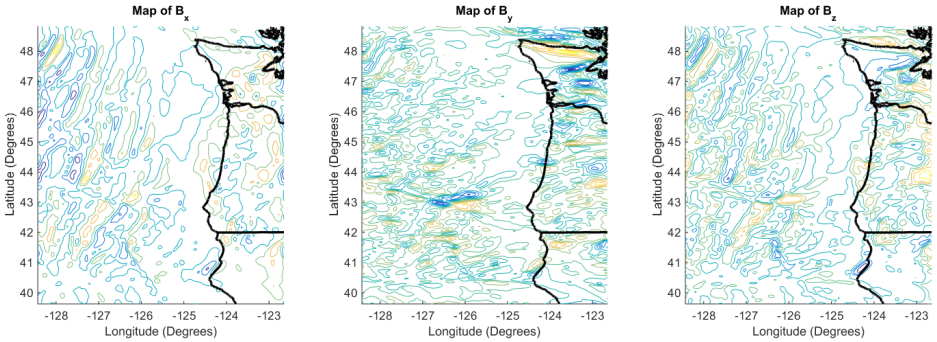

Figure 15. Contour Maps of Magnetic Anomaly Field Vector Components

Calculating the spatial gradient of these vector component maps gives the five unique gradient maps of the full magnetic field tensor used in the tensor measurement navigation filter. These maps contain individual gradient values in nT/km and examples are shown in Figure 16.

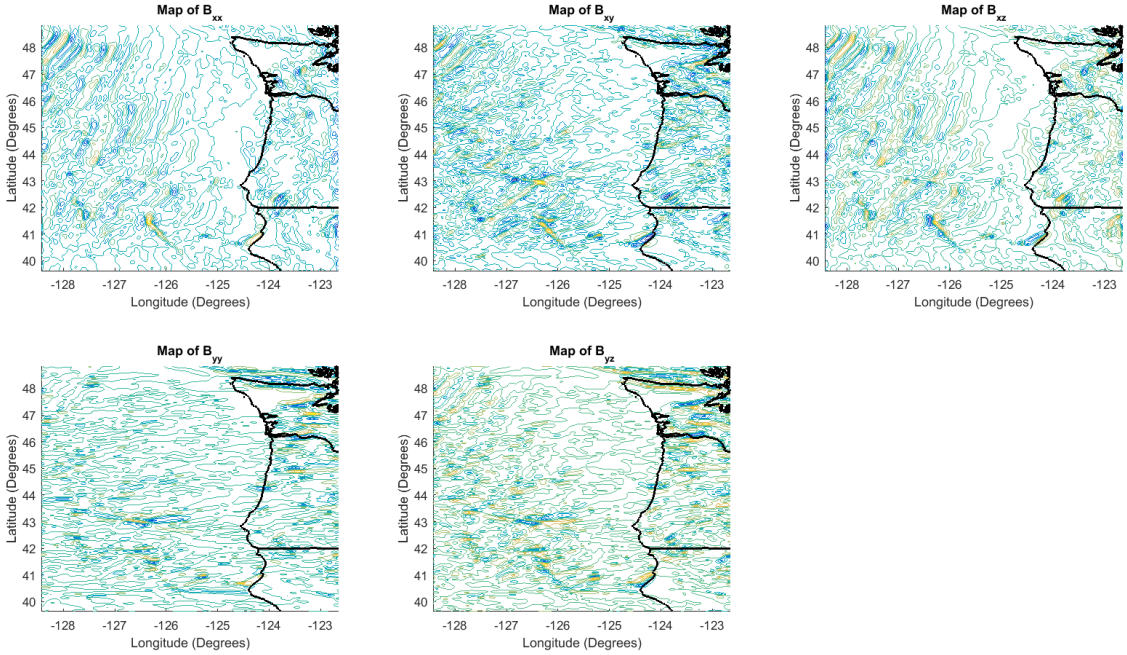

Figure 16. Contour Maps of Unique Magnetic Anomaly Field Tensor Components

Two simulation cases were run using maps generated from a source other than the NAMAD. For these cases the Enhanced Magnetic Model (EMM) was used to

evaluate the vector maps. Similar to the IGRF, the EMM is a spherical harmonic model. However, the EMM captures the magnetic anomaly field up to degree 790 as opposed to the IGRF capturing up to degree 13 as described in Chapter II [29]. The EMM is compiled from satellite, marine, aeromagnetic and ground magnetic surveys and resolves magnetic anomalies down to a 51 km wavelength [29]. Only capturing wavelengths down to 51 km leaves the EMM with a much lower resolution than the NAMAD. The EMM maps are not able to capture the high frequency content of the crustal field, which is what is primarily captured in the NAMAD maps.

While the maps generated from the EMM are of a lower resolution, they model the magnetic field globally and are not limited to North America as the NAMAD data is. The EMM maps will be referred to as global maps for this reason. Figure 17 shows the global EMM magnetic field data for the z directional component of the magnetic vector field. Vector component maps are directly resolved from the EMM. Figure 18 shows the contour maps of each vector field component generated from the EMM that were used for the simulation.

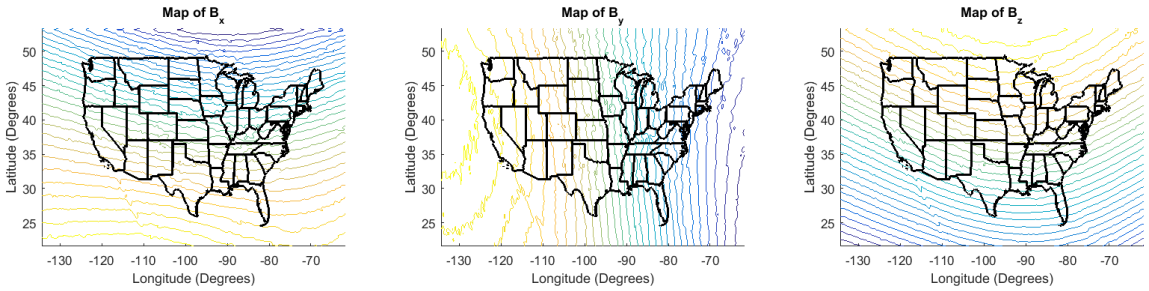

Figure 18. Contour Maps of Magnetic Anomaly Field Vector Components Resolved From the EMM

The spatial gradients of these vector maps give maps of the five unique tensor components used in the simulations. Figure 19 shows contour maps of the five unique tensor components resolved from the EMM data that was used for the simulation.

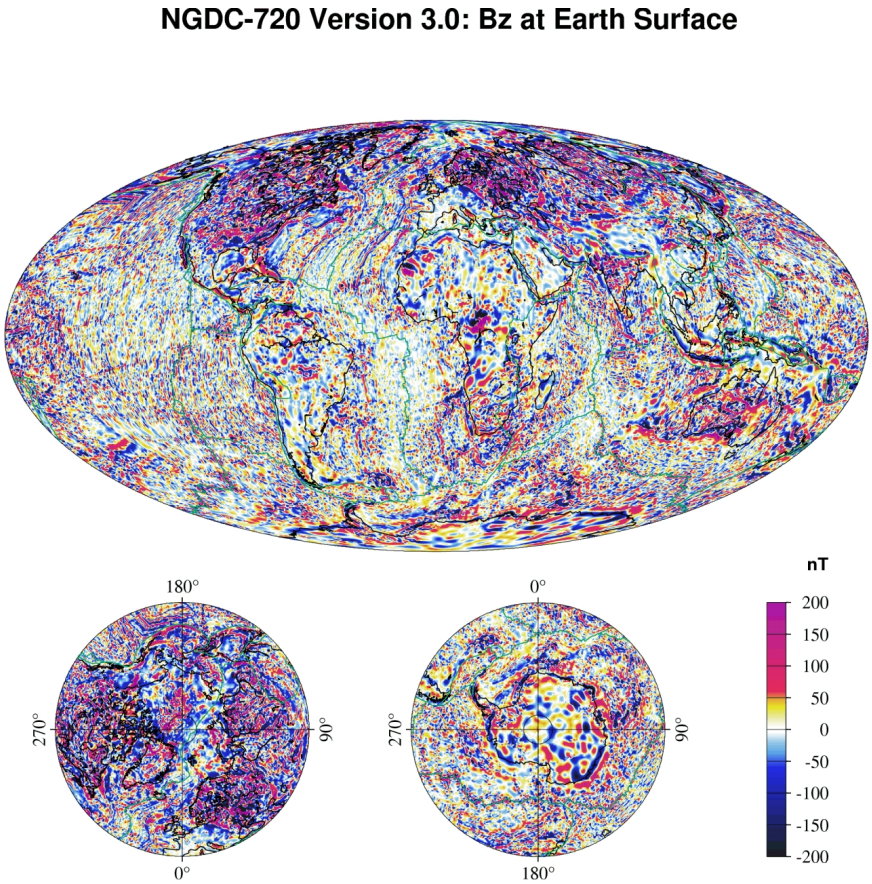

Figure 17. Vector Component Magnetic Field Content from EMM Data [29]

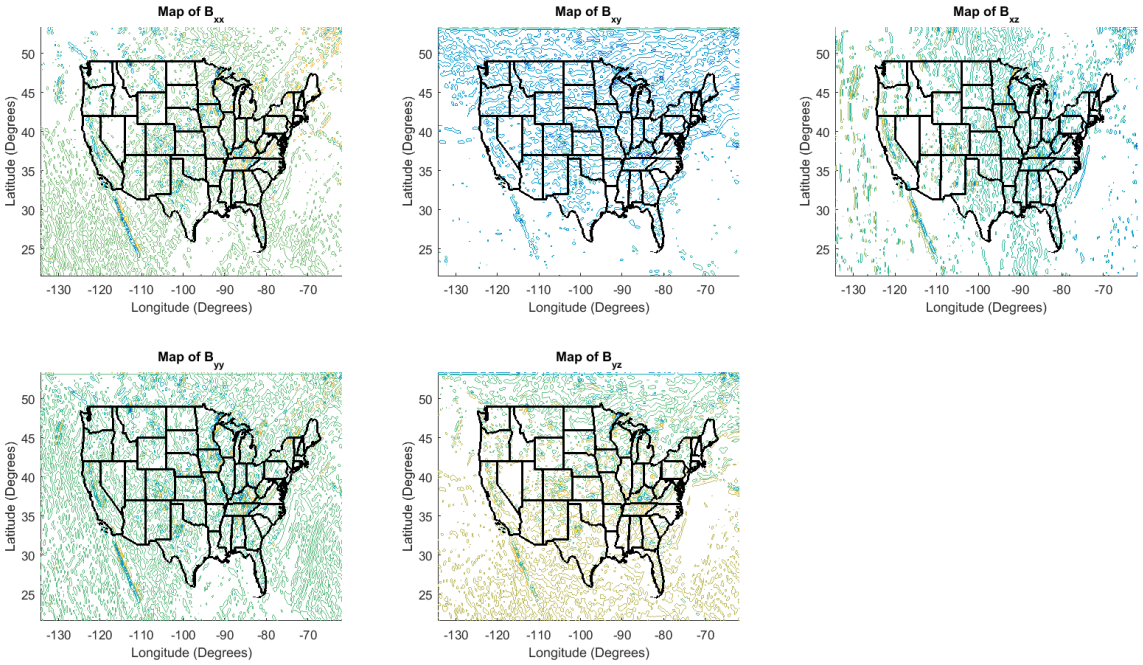

Figure 19. Contour Maps of Unique Magnetic Anomaly Field Tensor Components

3.5 Generating Simulated Measurements

Vector and Tensor measurements were not collected for the actual ship and aerial trajectories used. For the simulation, these measurements were generated using the process outlined below:

1. To generate both vector and tensor measurements, uncorrupted magnetic field values are calculated by entering the truth trajectory values for latitude and longitude into the same mapping functions found in the respective measurement models.

2. Vector measurements are corrupted with measurement biases that are modeled as FOGM processes to represent the magnetometer measurement error. A σ value of 3 nT and a τ value of 600 seconds were chosen for this simulation framework. If tensor measurements are being generated, measurement biases are not added.

3. These corrupted vector or tensor measurements are rotated into the body frame using the rotation matrix given in the truth trajectory.

4. For both vector and tensor measurements, white Gaussian noise with a covariance of $R = \sigma^2$ is added.

3.6 Generating Simulated INS Errors

This simulation framework requires the INS solution as opposed to raw INS data. To create the realistic INS solution, a 17-state Pinson error model was used to generate realistic INS errors throughout the entire truth trajectory. The truth trajectory position was then corrupted with the simulated INS position errors to get realistic INS position solutions. The true rotation matrix was also corrupted with the simulated INS tilt errors to get realistic INS solutions for rotation matrices. These simulated INS position and rotation matrix solutions are then used in the measurement functions of both navigation filters. Simulation parameters used to generate INS errors for a tactical-grade, navigation-grade, and 10X-grade INS are shown in Tables 1 through 3. The 10X-grade INS model is characterized by having position and angular drift noise strengths (VRW and ARW) ten times less than the navigation-grade INS model noise strengths.

Table 1. Simulation Parameters Chosen for Tactical-Grade INS Cases

Simulation Parameter	Chosen Value
VRW_σ	$0.3\,m/s^2\sqrt{Hz}$
ARW_σ	$6.06 \times 10^{-7}\,rad/s\sqrt{Hz}$
σ_g	$7.27 \times 10^{-6}\,rad/s$
τ_g	$3600\,s$
σ_a	$0.5 \times 10^{-3}\,m/s^2$
τ_a	$3600\,s$
σ_b	$10\,m$
τ_b	$3600\,s$

Table 2. Simulation Parameters Chosen for Navigation-Grade INS Cases

Simulation Parameter	Chosen Value
VRW_σ	$0.001\,m/s^2\sqrt{Hz}$
ARW_σ	$9.70 \times 10^{-9}\,rad/s\sqrt{Hz}$
σ_g	$1.45 \times 10^{-8}\,rad/s$
τ_g	$3600\,s$
σ_a	$25 \times 10^{-6}\,m/s^2$
τ_a	$3600\,s$
σ_b	$10\,m$
τ_b	$3600\,s$

Table 3. Simulation Parameters Chosen for 10X-Grade INS Cases

Simulation Parameter	Chosen Value
VRW_σ	$0.0001\, m/s^2\sqrt{Hz}$
ARW_σ	$9.70 \times 10^{-10}\, rad/s\sqrt{Hz}$
σ_g	$1.45 \times 10^{-9}\, rad/s$
τ_g	$3600\, s$
σ_a	$25 \times 10^{-7}\, m/s^2$
τ_a	$3600\, s$
σ_b	$10\, m$
τ_b	$3600\, s$

Examples of the simulated position and angular drift for the tactical-grade INS modeled are shown below in Figures 20 through 23 respectively. These figures show the predicted standard deviation for the position and angular drift as well as examples of the error generated for use in the simulations.

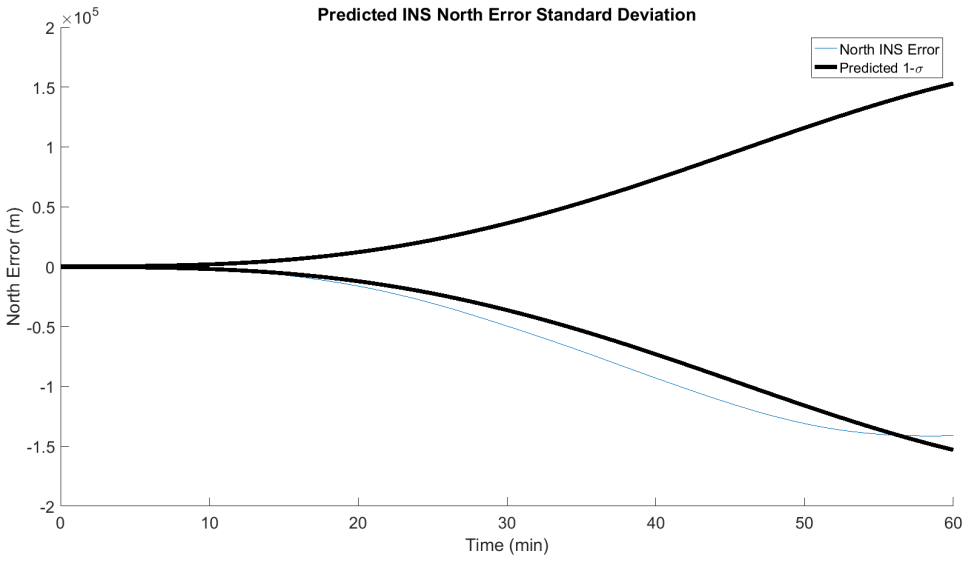

Figure 20. Generated North INS Error Using Tactical-Grade INS Model

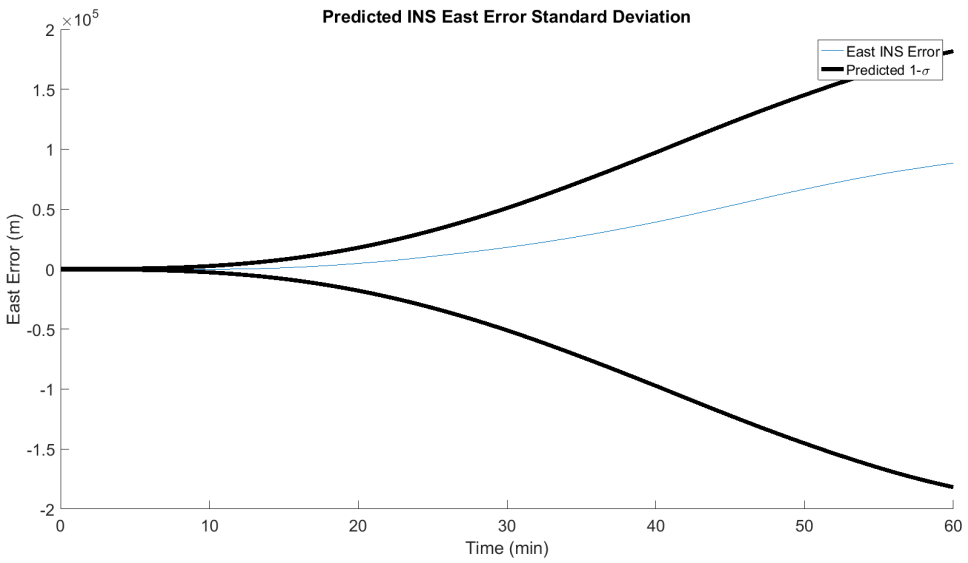

Figure 21. Generated East INS Error Using Tactical-Grade INS Model

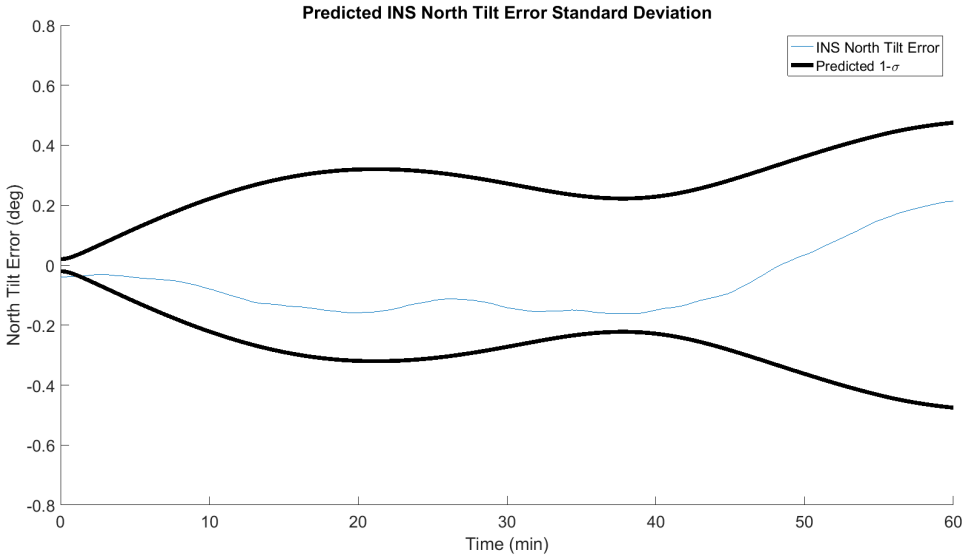

Figure 22. Generated North Tilt INS Error Using Tactical-Grade INS Model

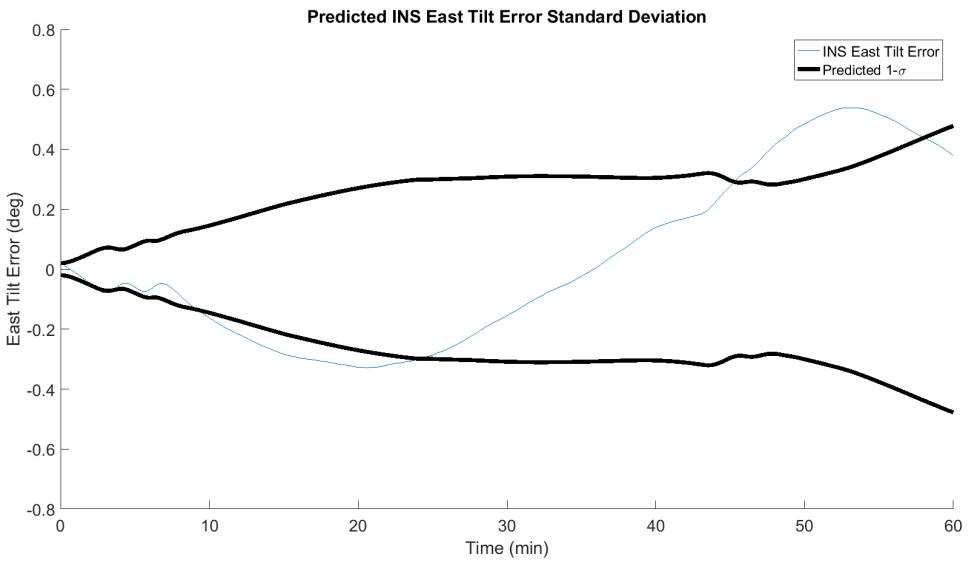

Figure 23. Generated East Tilt INS Error Using Tactical-Grade INS Model

When the simulation parameters are changed to model the navigation-grade INS, the simulated position and angular drifts are less than when the tactical-grade INS model was used. The predicted standard deviation of these position and angular errors are shown in Figures 24 through 27. It is clear that when the navigation-grade INS was simulated, the estimated standard deviation of position drift grew to approximately 4.5 km within the hour, while the tactical-grade INS simulated position drift standard deviation reached almost 200 km. This pattern is consistent with the position and angular drift specifications of an actual tactical and navigation-grade INS [10].

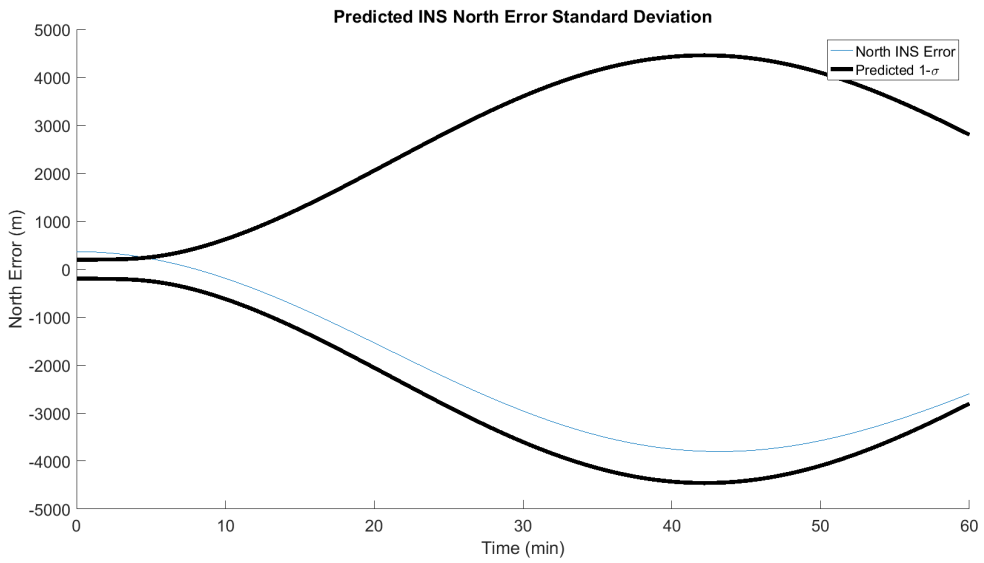

Figure 24. Generated North INS Error Using Navigation-Grade INS Model

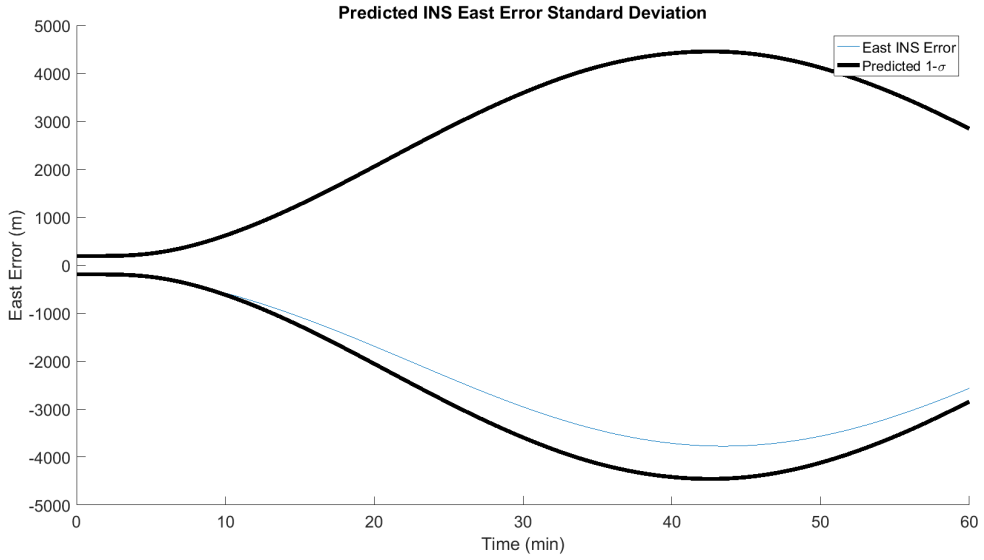

Figure 25. Generated East INS Error Using Navigation-Grade INS Model

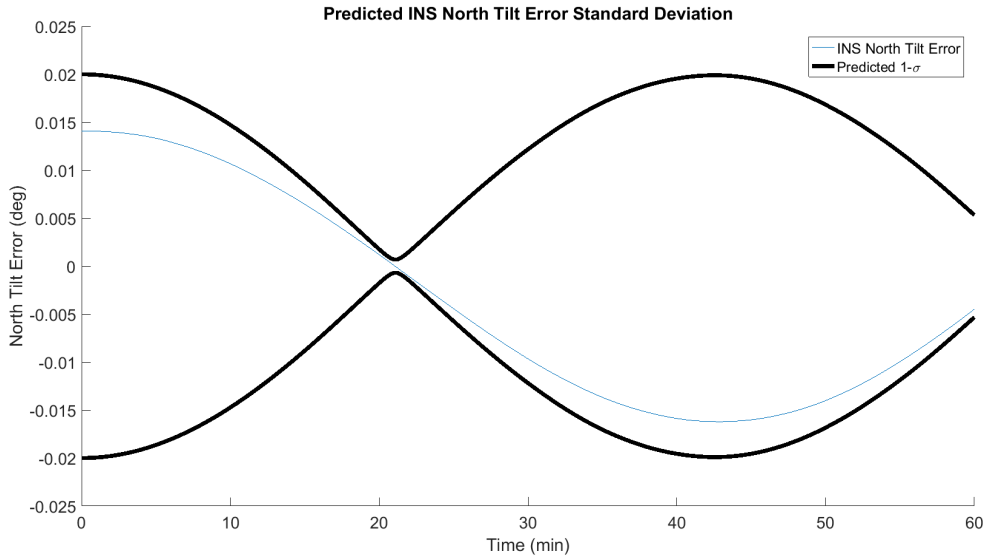

Figure 26. Generated North Tilt INS Error Using Navigation-Grade INS Model

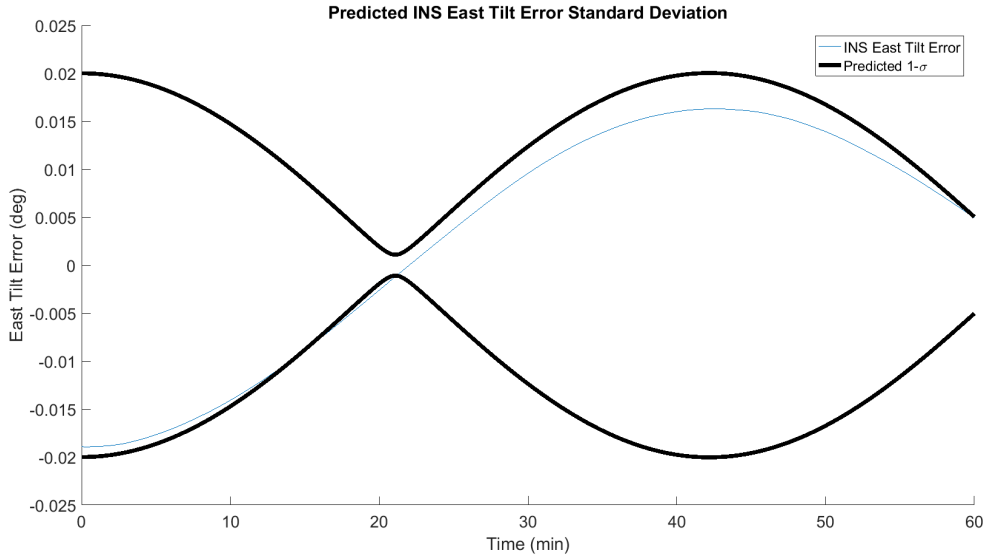

Figure 27. Generated East Tilt INS Error Using Navigation-Grade INS Model

IV. Results

The performance of the navigation systems introduced in the previous chapter are presented in Chapter IV. All simulation cases are listed and the metric used to evaluate filter performance is introduced. Each trajectory is then analyzed separately and the navigation accuracies and filter behavior for each navigation system combination are compared. Conclusions are drawn regarding the navigation system combination that gives the best navigation accuracies.

4.1 Simulation Cases

The specific cases investigated during this simulation case study are outlined in Table 4. Each case is characterized by the type of measurement, the truth trajectory, and the grade of INS used for navigation. Table 4 shows the specifics for each case. For simplicity, each specific case will be referred to by an abbreviation of the measurement type used within the navigation system (e.g. "VEC" for vector measurements and "TEN" for tensor measurements) combined with an abbreviation of the quality of INS used in the navigation system (e.g. "TACT" for tactical-grade INS and "NAV" for navigation-grade INS and "10X" for 10X-grade INS). For example, case 2 in Table 4 below will be referred to as the VEC-NAV case for the coastal boat trajectory and case 7 will be referred to as the TEN-TACT case for the coastal airplane trajectory.

For all cases, the initial position uncertainty was set to 200 m, the initial velocity uncertainty to 0.01 m/s and initial attitude uncertainty to 0.02 degrees. For all cases, a measurement noise covariance of $\mathbf{R}$ was used to generate measurements and a dynamics noise covariance of $\mathbf{Q}$ was used to generate INS data. For filter tuning, in the vector measurement cases, the filter's measurement model was given a value of $2\mathbf{R}$ and for the tensor measurement cases, the measurement model was given a value of

Table 4. List of Simulation Cases

Case	Trajectory	Measurement Type	INS Quality
1	Coastal Boat	Vector	Tactical
2	Coastal Boat	Vector	Navigation
3	Coastal Boat	Tensor	Tactical
4	Coastal Boat	Tensor	Navigation
5	Coastal Aerial	Vector	Tactical
6	Coastal Aerial	Vector	Navigation
7	Coastal Aerial	Tensor	Tactical
8	Coastal Aerial	Tensor	Navigation
9	Continental Aerial	Vector	Tactical
10	Continental Aerial	Vector	Navigation
11	Continental Aerial	Tensor	Tactical
12	Continental Aerial	Tensor	Navigation
13	Deep-Sea Boat	Vector	10X
14	Deep-Sea Boat	Tensor	10X
15	Global Model Boat	Vector	10X
16	Global Model Boat	Tensor	10X

$10\mathbf{R}$. In the vector measurement cases, the filter's dynamics model was given a value of $2\mathbf{Q}$, while the tensor dynamics model was given a value of $10\mathbf{Q}$. This increased the stability of the filters, because the filter was expecting a noisier measurement than it was actually receiving. Setting the measurement covariances within the filter two or ten times greater than the covariance of the simulated measurements kept the filter from becoming over-confident in some cases. The tensor measurement filter required a greater multiple because bias error states were not modeled and the filter tended to become over-confident more often than in the vector measurement filter.

4.2 DRMS Error

The Distance Root Mean Square (DRMS) error is the metric used to measure filter performance for each simulation case. Monte Carlo simulations were run to evaluate the average DRMS error of the navigation filter in each case. This was used to compare filter performance between the different scenarios. The CRLB DRMS

Error was also calculated to get an idea of how the navigation filter is performing compared to its own theoretical optimal performance. Equations 99 and 100 define the EKF DRMS error and CRLB DRMS error calculations respectively[28].

$$\text{DRMS Error} = \sqrt{\frac{\sum_{k=1}^{n}(d_k)^2}{n}} \tag{99}$$

$$\text{CRLB DRMS Error} = \sqrt{\frac{\sum_{k=1}^{n}(\sigma_N^2 + \sigma_E^2)}{n}} \tag{100}$$

where

n = number of time steps in the trajectory

d_k = Euclidian distance between horizontal truth position and filter solution

σ_N and σ_E are the CRLB standard deviations for the horizontal position states

4.3 Coastal Boat Trajectory Results

This section outlines the simulation results for the cases 1 through 4 that used the boat's truth trajectory off the west coast of the U.S. The trajectory was one hour long and had an average velocity of approximately 6 m/s.

Figure 28 shows the path of the ship over the three vector component maps of the magnetic field.

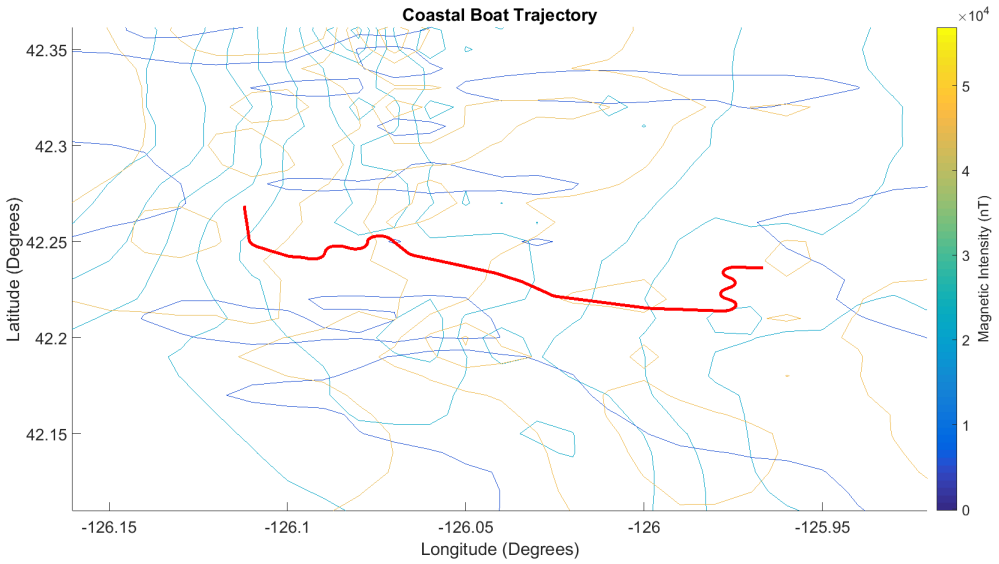

Figure 28. Boat Trajectory Overlayed Onto Vector Field Maps

An example of the corrupted vector and tensor measurements generated for this trajectory are shown in Figures 29 and 30 respectively. The measurements were corrupted with zero-mean White Gaussian noise with a covariance of 1 nT^2 for the vector measurements and 0.1 $\frac{\text{nT}^2}{\text{km}^2}$ for the tensor measurements.

Table 5. DRMS Results for U.S. Western Coast Boat Trajectory

Case	Measurement Type	INS Quality	DRMS Error	CRLB DRMS Error
1	Vector	Tact	420.54 m	342.39 m
2	Vector	Nav	185.00 m	241.39 m
3	Tensor	Tact	755.48 m	136.21 m
4	Tensor	Nav	35.94 m	49.36 m

Table 6. Filter Error in North and East Tilt Error States for U.S. Western Coast Boat Trajectory

Case	North Tilt Filter Error	East Tilt Filter Error
VEC-TACT	0.07 deg	0.11 deg
VEC-NAV	9×10^{-4} deg	3×10^{-3} deg
TEN-TACT	Unstable	Unstable
TEN-NAV	1.2×10^{-3} deg	1.9×10^{-3} deg

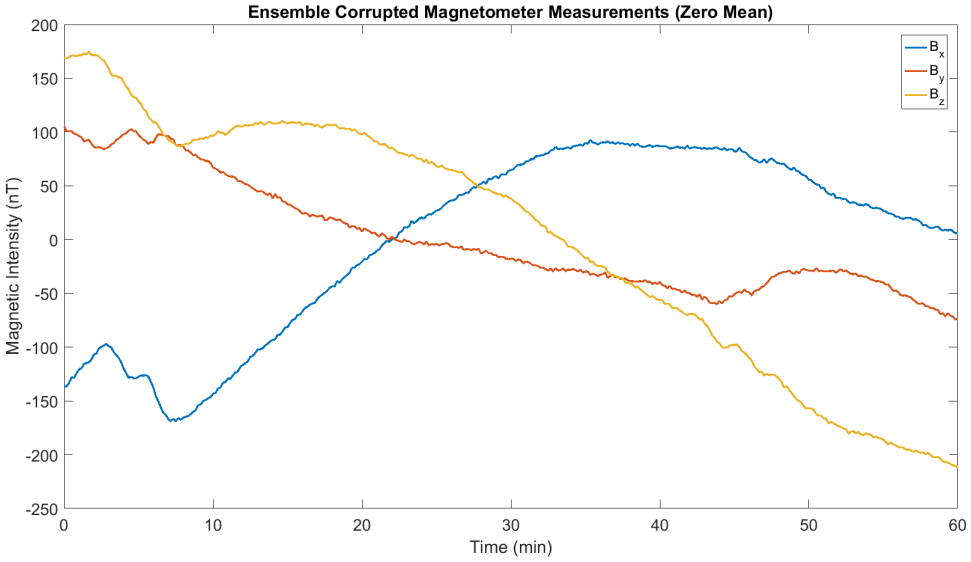

Figure 29. Corrupted World-Frame Vector Magnetometer Measurements for the VEC-TACT and VEC-NAV Cases

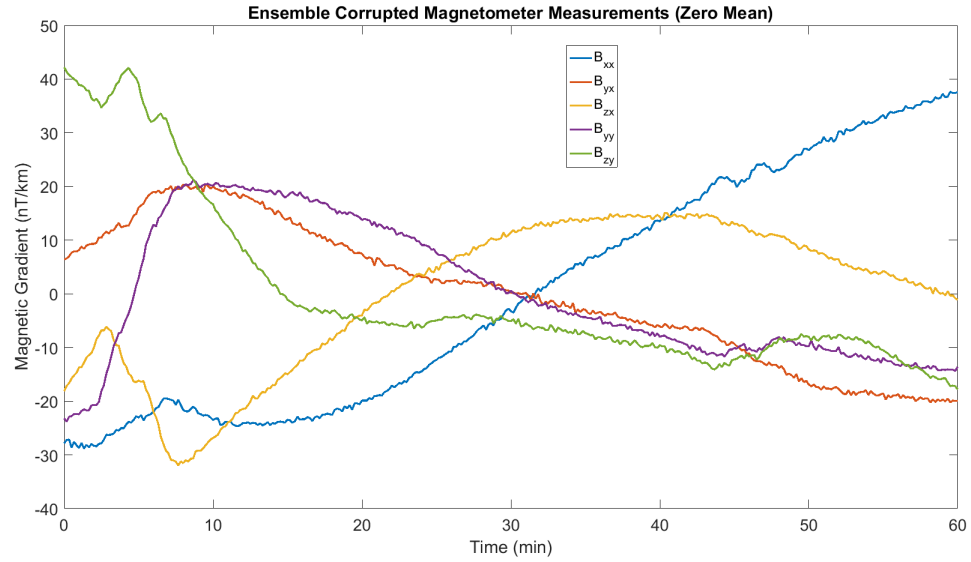

Figure 30. Corrupted World-Frame Magnetic Tensor Measurements for the TEN-TACT and TEN-NAV Cases

CRLB Trend.

The CRLB DRMS errors shown in Table 5 display the trend that should be expected from the EKF DRMS Error results. The VEC-NAV case out-performed the VEC-TACT case with 101 m less position error and the TEN-NAV case out-performed TEN-TACT with 86.85 m less position error. From this we can expect to see the navigation filter paired with a navigation-grade INS to out-perform the same filter paired with a tactical-grade INS. Additionally, the TEN-TACT and TEN-NAV cases, where tensor measurements were used, out-performed the VEC-TACT and VEC-NAV cases, where vector measurements were used.

Monte Carlo Simulation Results.

Figures 31 through 34 show the results of a 500 run Monte Carlo simulation for the VEC-TACT and VEC-NAV cases in the horizontal position states. Results from the Monte Carlo simulations for cases VEC-TACT and VEC-NAV reflect the expected trend from the CRLB results. With a DRMS Error of 185.00 m, the filter paired with the navigation-grade INS in the VEC-NAV case out-performed the filter paired with the tactical-grade INS in the VEC-TACT case by 235.54 m. Both filters were stable, with no divergent runs. While the position error in the VEC-TACT case increases to an average of 1.5 km approximately thirty minutes into the trajectory, the filter is able to lock back down on position and does not continue to drift as the un-aided INS would. In the VEC-NAV case, we do not see the same increase in error at 30 minutes, and the filter remains locked on to the true position with steady error throughout the entire trajectory. Figures 31 through 34 show the standard deviation of the Monte Carlo error, which tends to be slightly lower than the CRLB. The CRLB is the theoretical lowest possible state covariance, however, because of the tuning that was described previously (the filters being given a multiple of $\mathbf{R}$ and $\mathbf{Q}$), it is possible

for Monte Carlo DRMS error to be slightly lower than the DRMS error of the CRLB. The CRLB is expecting greater measurement noise than is actually present in the corrupted measurements. The CRLB and the filter models are both given the same tuning parameters, so while the filter was able to out-perform the CRLB DRMS error in simulation, the filter predicted covariance matches, but does not exceed, the CRLB.

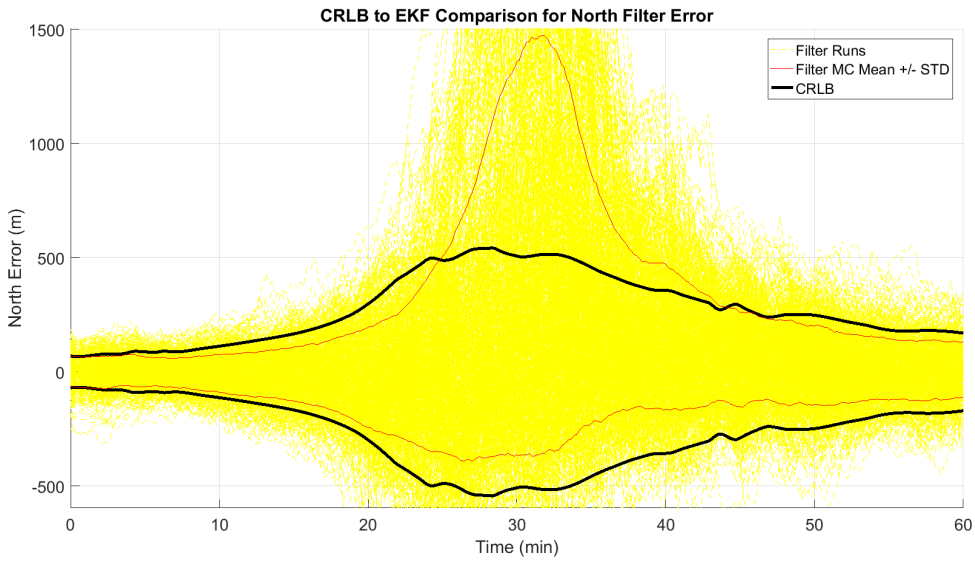

Figure 31. EKF Error in North Position State for the VEC-TACT Case

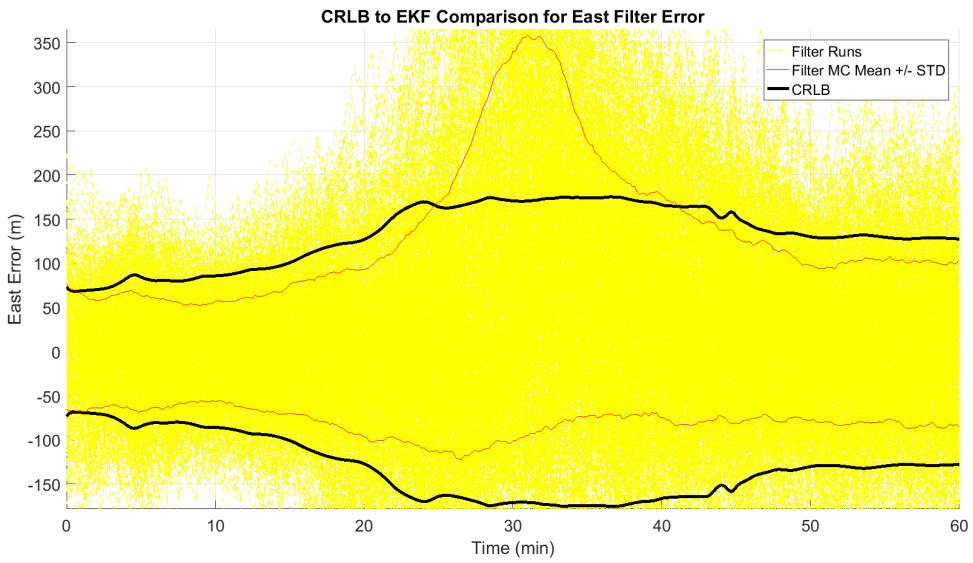

Figure 32. EKF Error in East Position State for the VEC-TACT Case

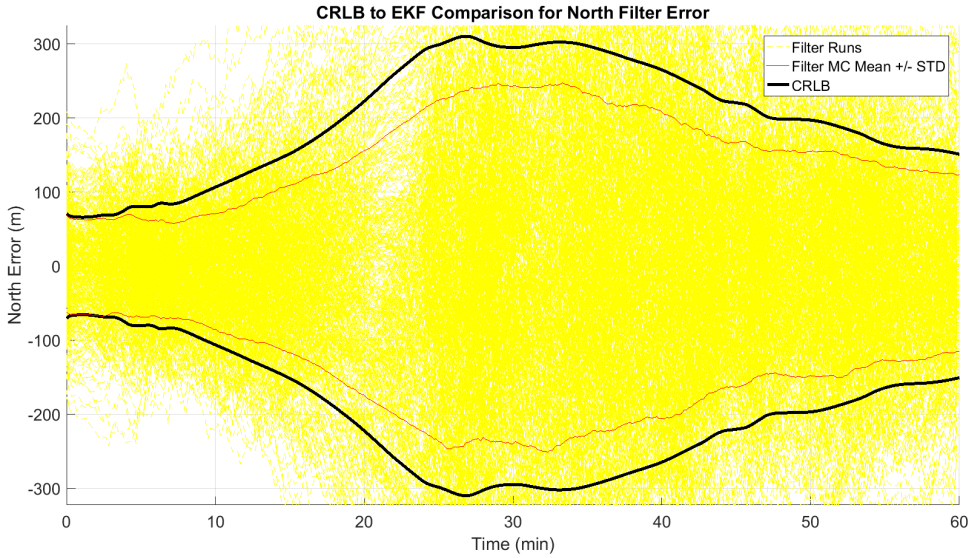

Figure 33. EKF Error in North Position State for the VEC-NAV Case

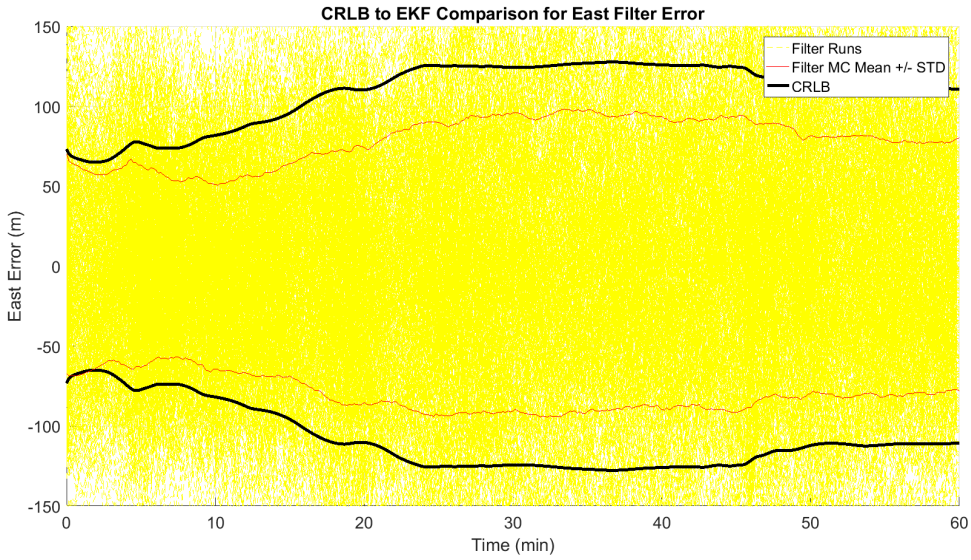

Figure 34. EKF Error in East Position State for the VEC-NAV Case

The filter predicted covariance more closely matches the CRLB, as shown in Figure 35 and 36. The DRMS error for the single runs plotted in Figure 35 and 36 were 238.25 m and 152.64 m respectively.

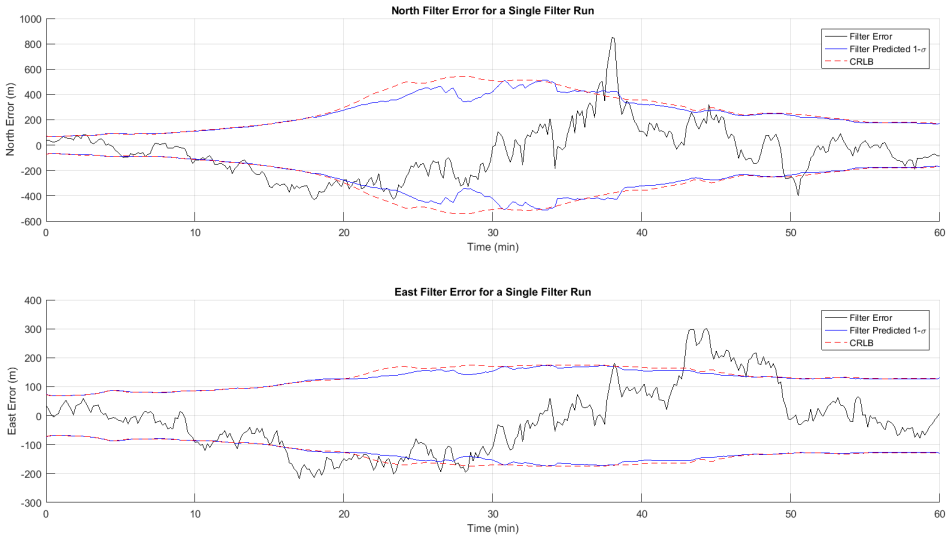

Figure 35. EKF Error in Horizontal Position States for a Single Run - VEC-TACT

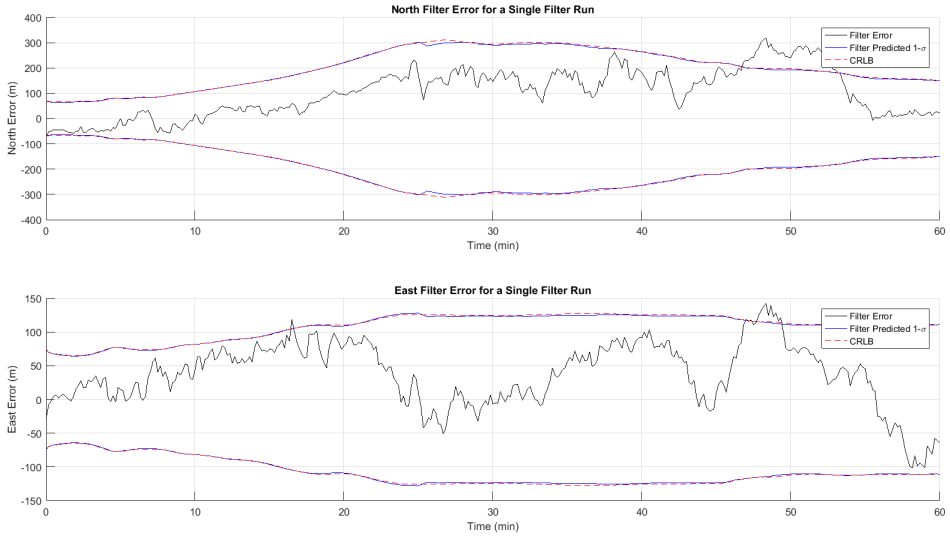

Figure 36. EKF Error in Horizontal Position States for a Single Run - VEC-NAV

While the TEN-TACT and TEN-NAV cases reflect this same trend of the navigation-grade INS out-performing the tactical grade INS, the TEN-TACT case, where tensor measurements were used demonstrated a DRMS error of 755.48 m. This error is greater than the filter in the VEC-TACT case, which also uses a tactical grade INS, but was only using three vector measurements as opposed to five tensor measurements. This does not agree with the CRLB DRMS error results. While the filter in the TEN-TACT case did not diverge, the position error plots in Figures 37 and 38 display abnormal filter behavior and may be due to filter tuning.

This same trend occurred for the TEN-TACT case during the coastal and continental aerial trajectories as well. The tensor measurement navigation filter often diverged in Monte Carlo simulation when paired with a tactical grade INS. This was not a problem when the navigation-grade INS was paired with the tensor measurement filter for all TEN-NAV cases. The Monte Carlo position error plots for the TEN-TACT and TEN-NAV cases during the coastal boat trajectory are shown in Figures 37 through 40.

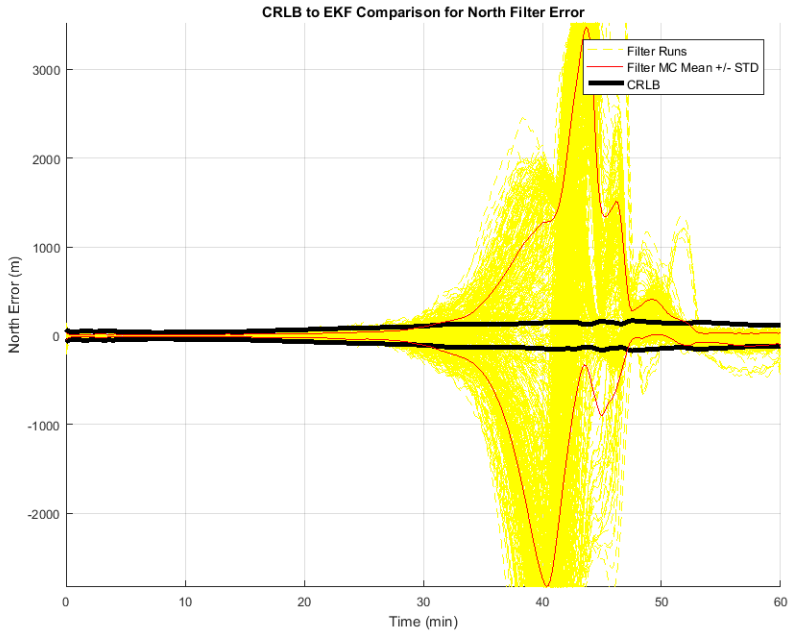

Figure 37. EKF Error in North Position State for TEN-TACT Case

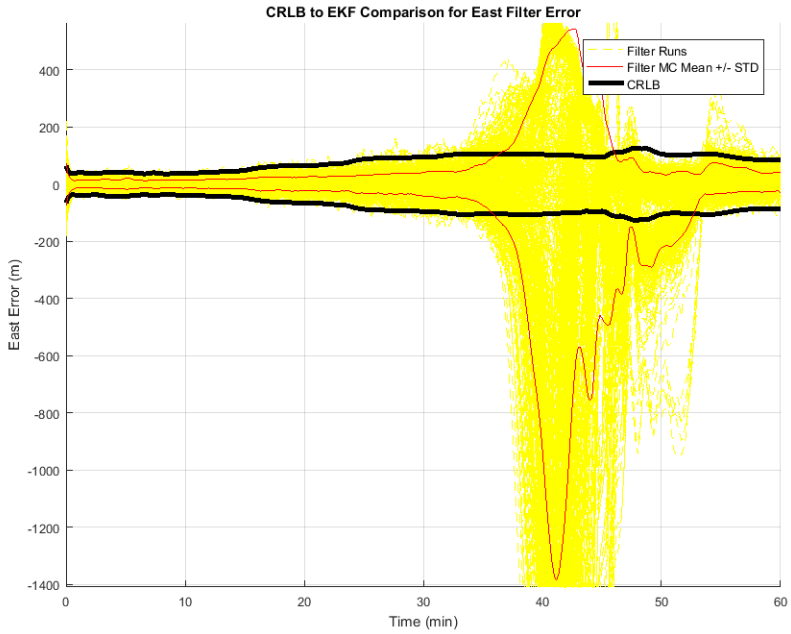

Figure 38. EKF Error in East Position State for TEN-TACT Case

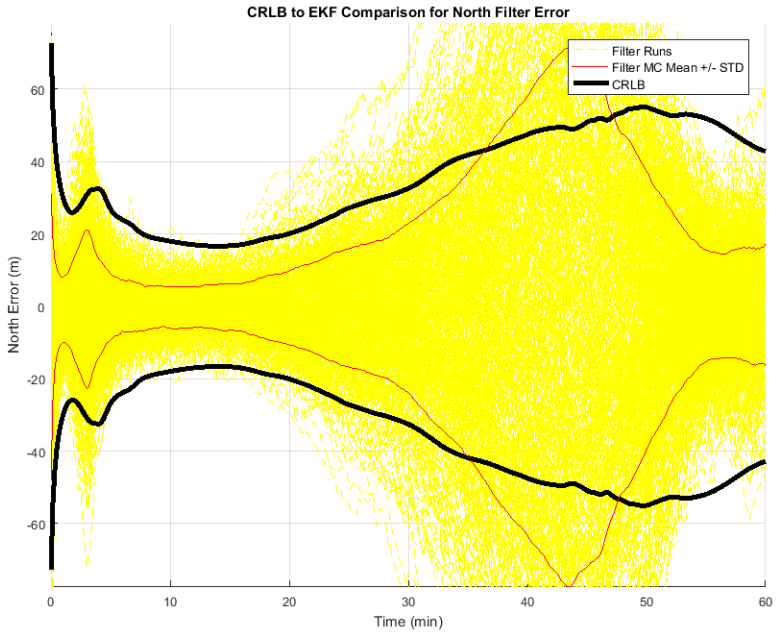

Figure 39. EKF Error in North Position State for TEN-NAV Case

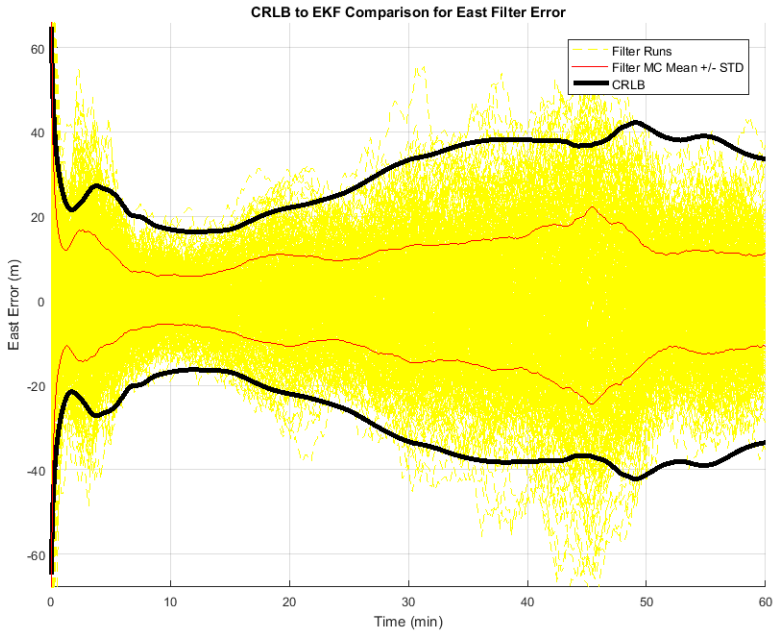

Figure 40. EKF Error in East Position State for TEN-NAV Case

The navigation filter in the VEC-NAV and TEN-NAV cases were able to greatly improve upon the unaided navigation-grade INS position error drift that we would expect to be approximately 1 nmi/h (or 1,852 meters per hour) [10]. Additionally, the VEC-TACT case was able to improve drastically upon the drift expected from an unaided tactical-grade INS (approximately 10 nmi/h [10]).

Aside from the accuracy of the position solution, the ability of the filter to accurately estimate the tilt error states is also examined. Their use in the measurement function to correct the INS rotation matrix makes their accuracy imperative. Accurate estimates of the tilt error states allow for higher accuracy resolution of the roll, pitch, and yaw of the vehicle throughout the trajectory.

The tilt error states for the TEN-NAV case are shown for a single filter run in Figures 41 through 43. The DRMS error for this single run was 40.15 m.

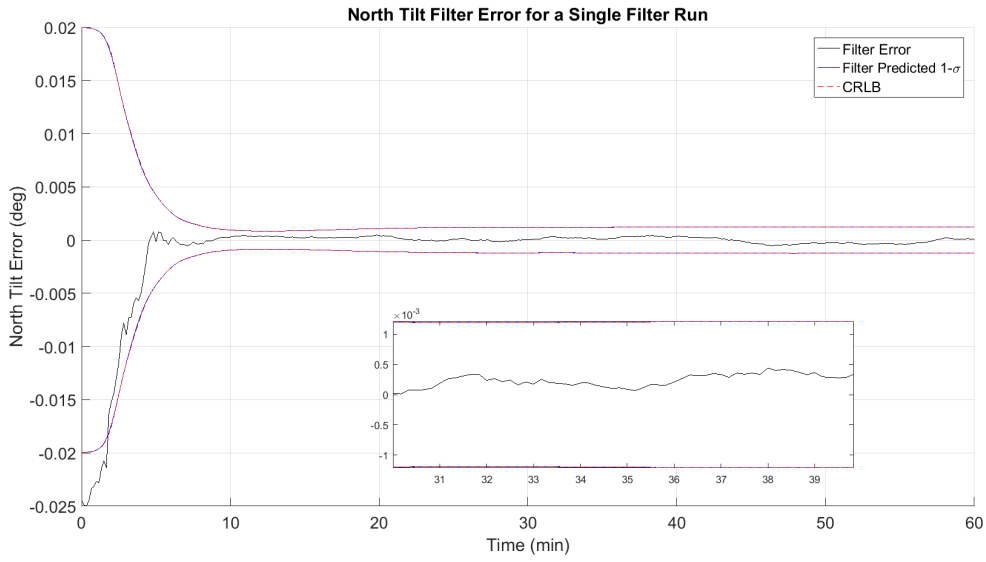

Figure 41. EKF Error in North Tilt Error States for the TEN-NAV Case

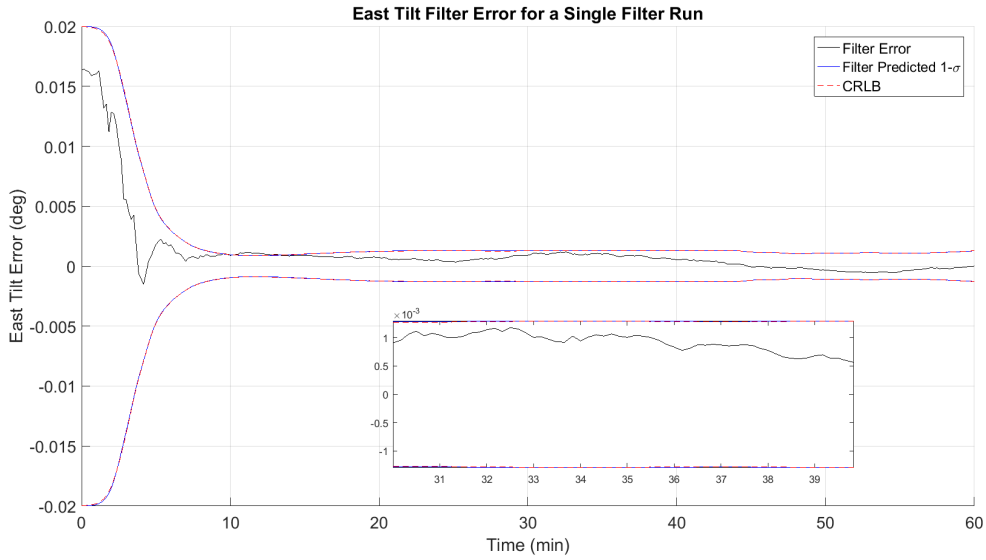

Figure 42. EKF Error in East Tilt Error States for the TEN-NAV Case

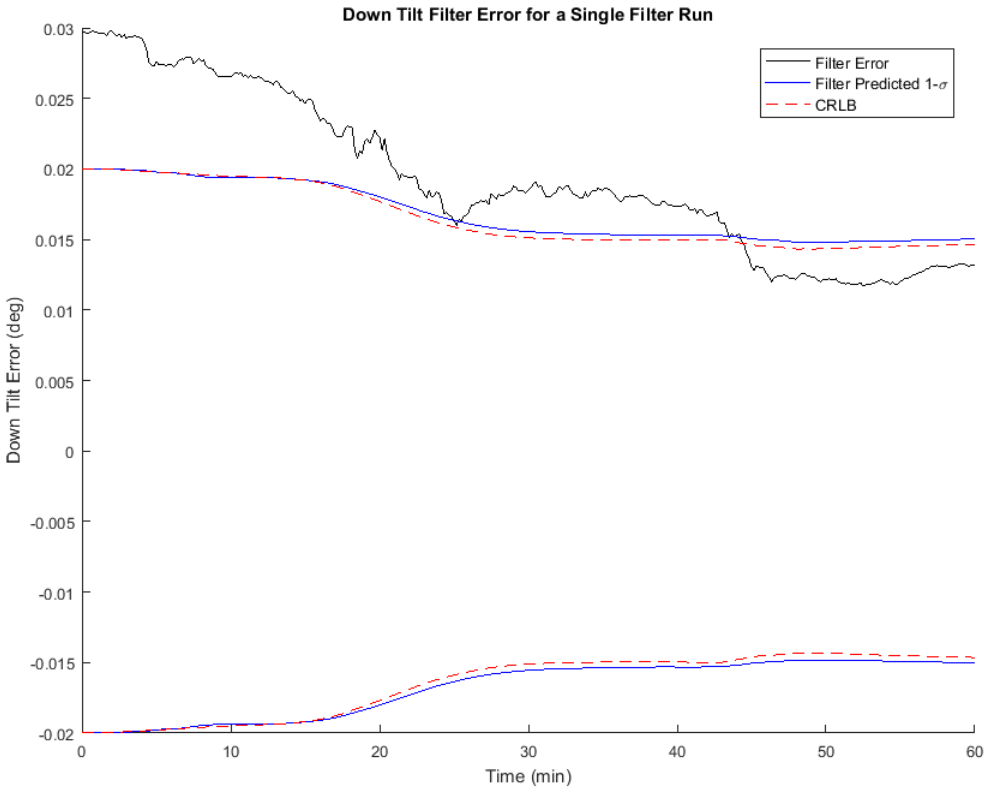

Figure 43. EKF Error in Down Tilt Error States for the TEN-NAV Case

For the VEC-NAV case, where vector measurements were used, the tilt error states displayed the same stability as in the TEN-NAV case. The steady state values of filter error for the north and east tilt error states are listed in Table 6.

When a tactical grade INS was used, it is clear that the tilt error state estimates are stable, but are less accurate overall than in the VEC-NAV case. The tilt error states for the single run of the VEC-TACT case are shown in Figure 44. The tactical-grade INS did not give as much observability of the tilt error states as the navigation-grade INS.

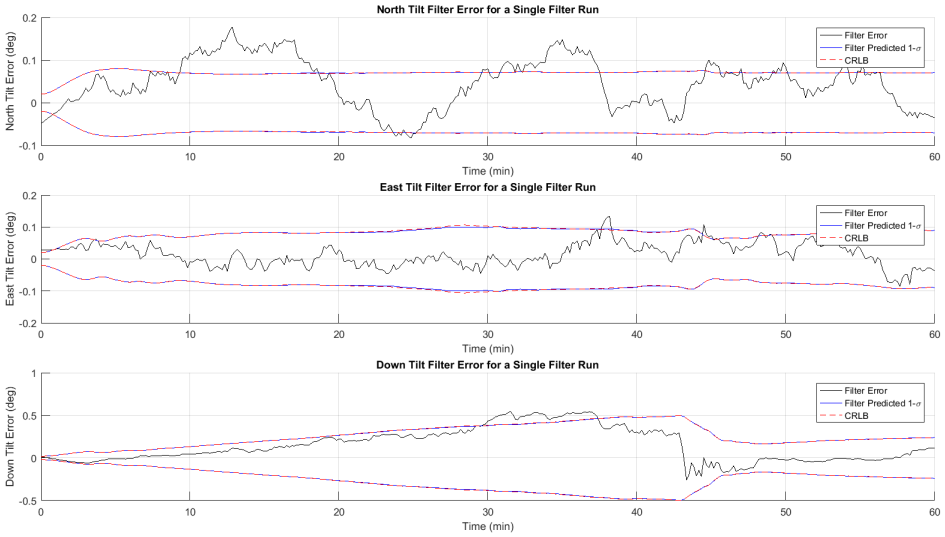

Figure 44. EKF Error in Tilt Error States for the VEC-TACT Case

4.4 Coastal Airplane Trajectory Results

The trajectory used for cases 5 through 8 was a one-hour airplane trajectory with an average velocity of 62.85 m/s. Figure 45 shows the path of the airplane over the three vector component maps of the magnetic field. An example of the vector and tensor measurements generated for these cases are shown in Figures 46 and 47.

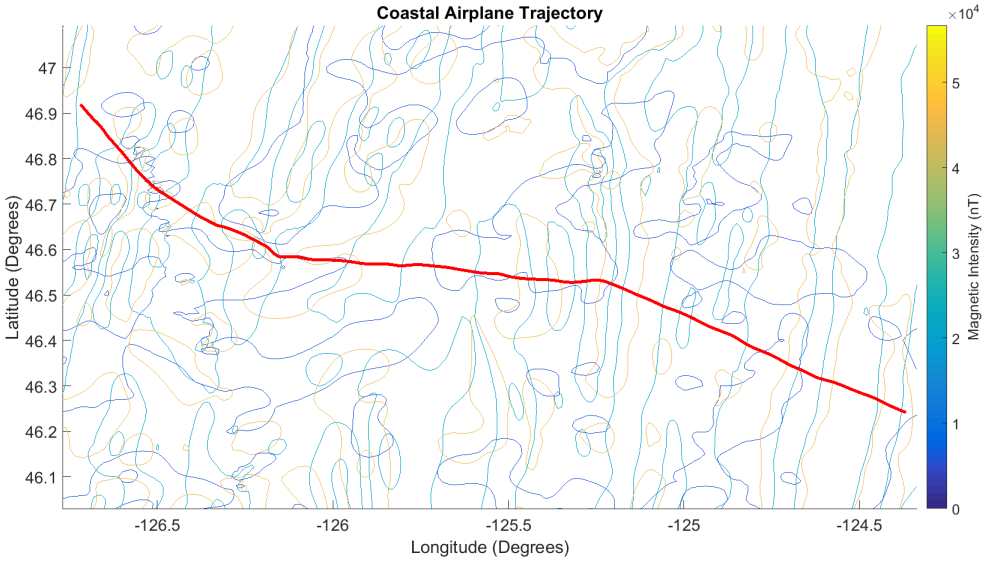

Figure 45. Airplane Trajectory Overlayed Onto Vector Field Maps

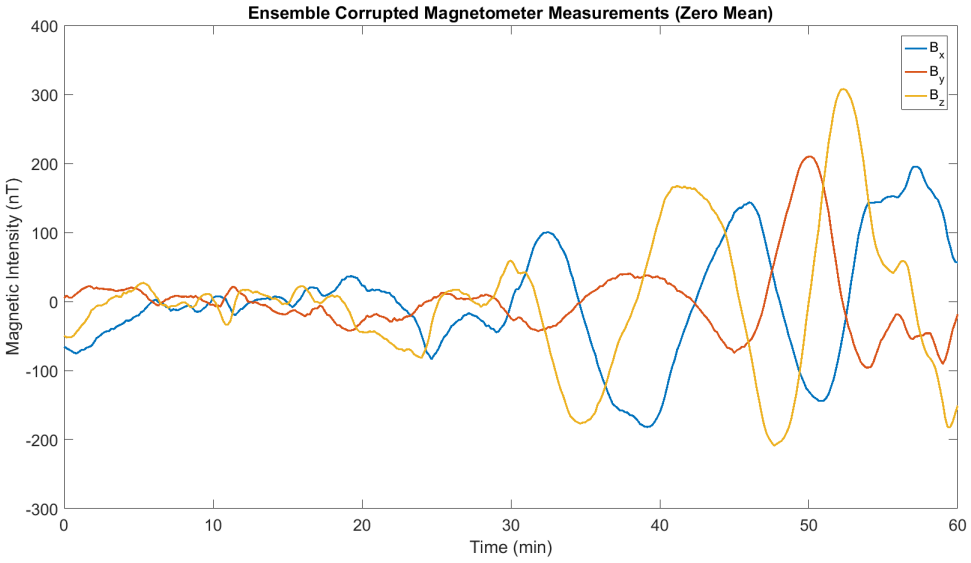

Figure 46. Corrupted World-Frame Vector Magnetometer Measurements for the VEC-TACT and VEC-NAV Cases

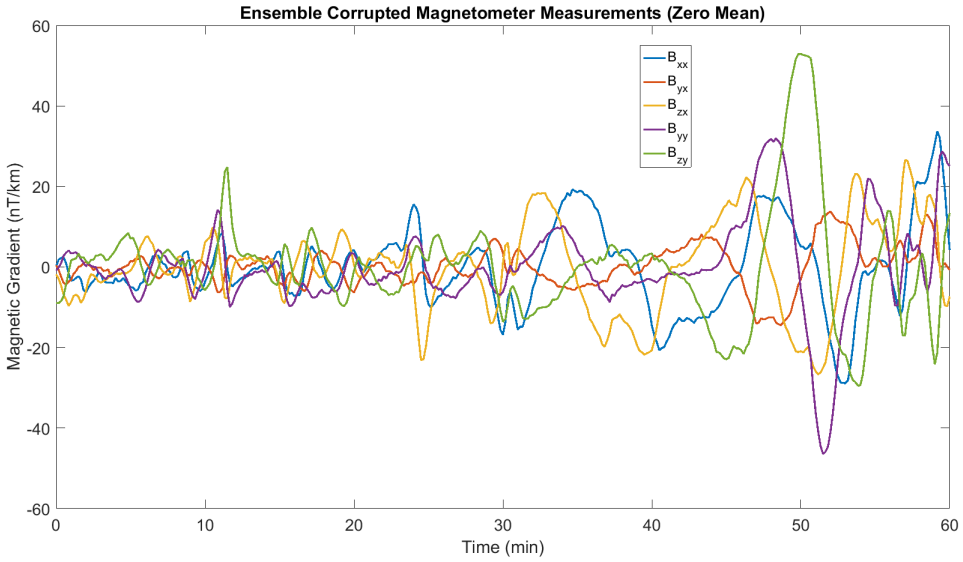

Figure 47. Corrupted World-Frame Magnetic Tensor Measurements for the TEN-TACT and TEN-NAV Cases

Table 7. DRMS Results for U.S. West Coast Aerial Trajectory

Case	Measurement Type	INS Quality	DRMS Error	CRLB DRMS Error
5	Vector	Tact	254.96 m	315.26 m
6	Vector	Nav	103.43 m	128.18 m
7	Tensor	Tact	Filter Diverged	252.46 m
8	Tensor	Nav	61.07 m	85.97 m

Table 8. Filter Error in North and East Tilt Error States for U.S. West Coast Aerial Trajectory

Case	North Tilt Filter Error	East Tilt Filter Error
VEC-TACT	0.07 deg	0.1 deg
VEC-NAV	1×10^{-3} deg	1×10^{-3} deg
TEN-TACT	Unstable	Unstable
TEN-NAV	6×10^{-4} deg	1×10^{-3} deg

The CRLB results show that we expect the TEN-TACT case to have improved filter performance over the VEC-TACT case. And similarly, we expect to see the

TEN-NAV case perform better than the VEC-NAV case. The CRLB DRMS Error for the filters paired with a navigation-grade INS is lower than the same filters paired with a tactical-grade INS.

As mentioned previously, the tensor measurement filter was unstable when a tactical-grade INS was used and the EKF DRMS results for the TEN-TACT case reflect this. However, the vector measurement filter paired with the tactical-grade INS remained stable for a majority of the runs (0.4% of filter runs diverged). Figures 48 and 49 show the filter error in the horizontal position states for a 500-run Monte Carlo simulation of the VEC-TACT case.

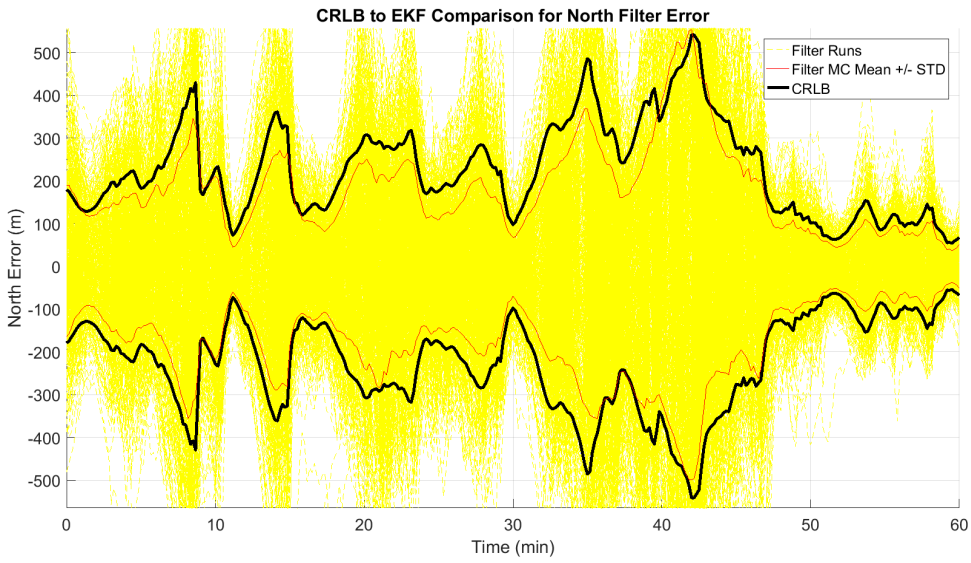

Figure 48. EKF Error in North Position State for the VEC-TACT Case

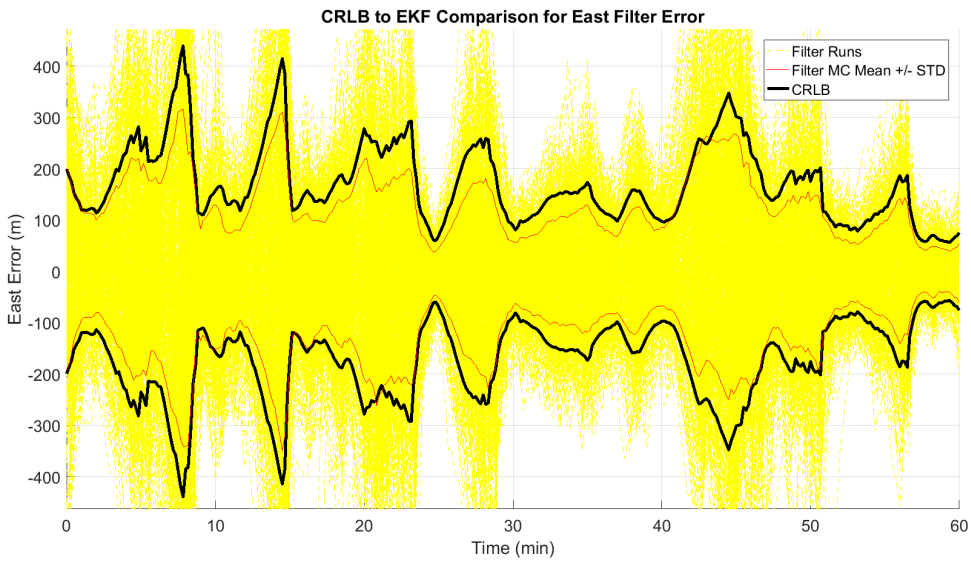

Figure 49. EKF Error in East Position State for the VEC-TACT Case

With the instability of the filter in the TEN-TACT case, the mean error of the Monte Carlo runs appears to grow without bound, and is considered divergent. As with the VEC-NAV and TEN-NAV cases during the coastal boat trajectory described earlier, the VEC-NAV and TEN-NAV cases during the coastal aerial trajectory also show stable filter performance. The Monte Carlo simulation results for the VEC-NAV and TEN-NAV cases during the coastal aerial trajectory are shown in Figures 50 through 53.

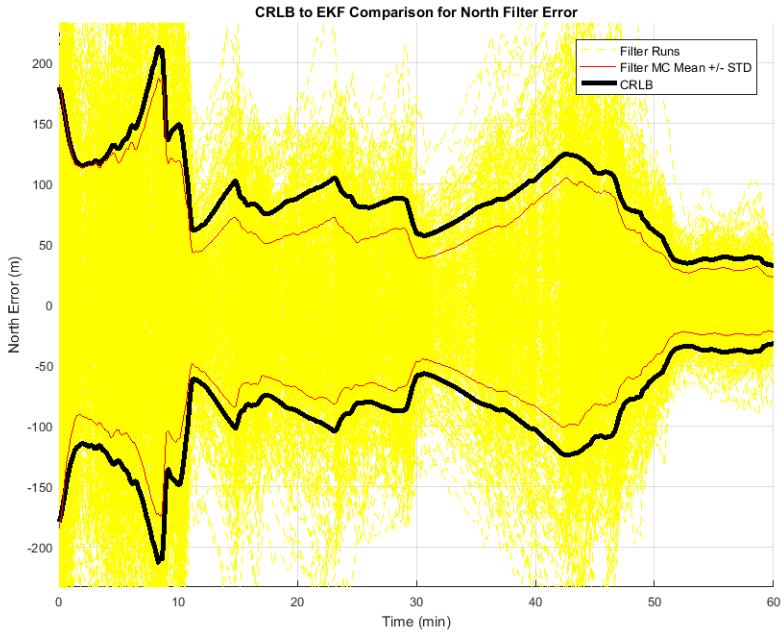

Figure 50. EKF Error in North Position State for the VEC-NAV Case

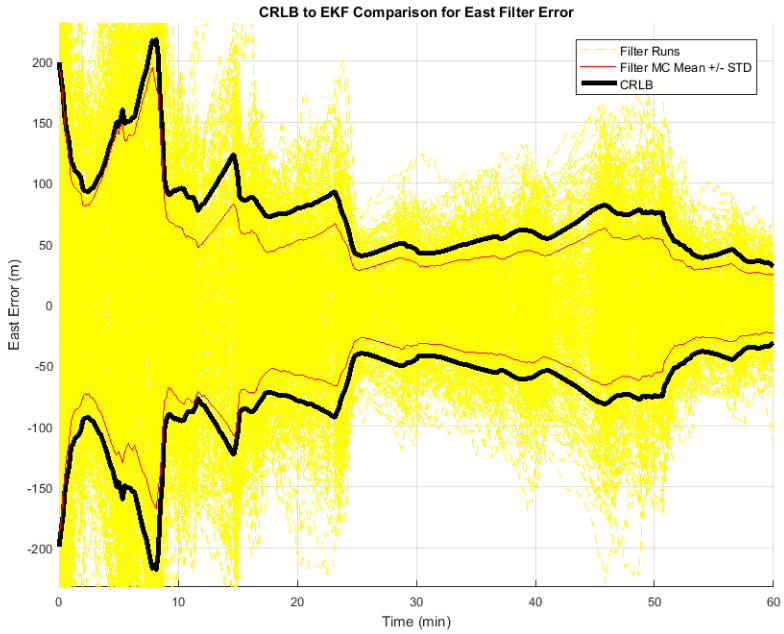

Figure 51. EKF Error in East Position State for the VEC-NAV Case

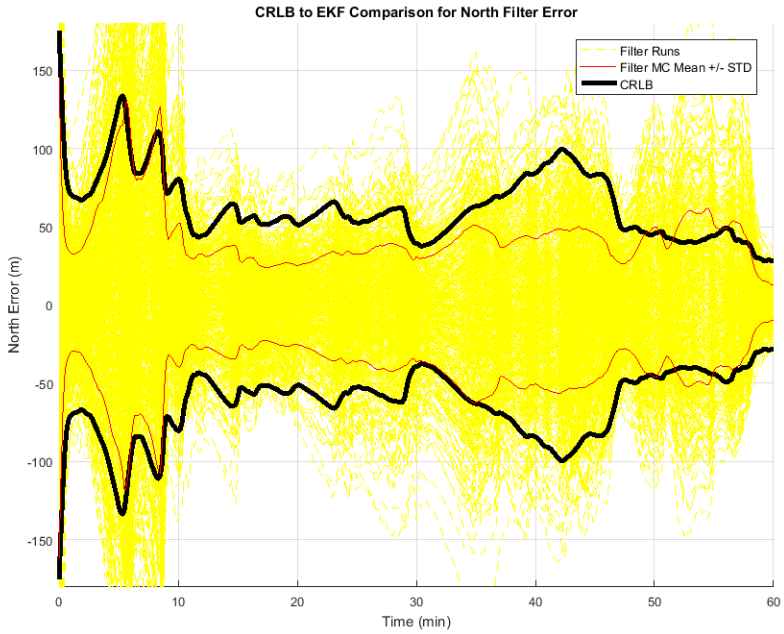

Figure 52. EKF Error in North Position State for the TEN-NAV Case

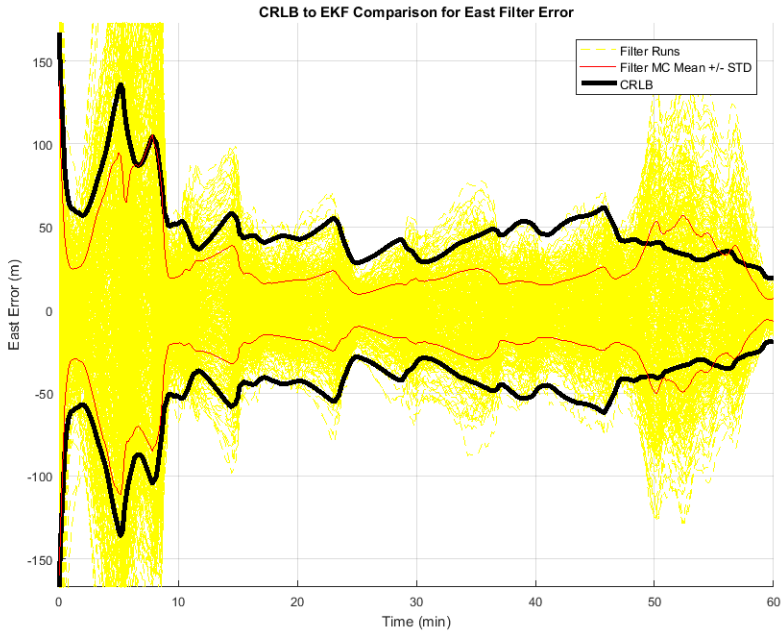

Figure 53. EKF Error in East Position State for the TEN-NAV Case

The tilt error states for the TEN-TACT case, where a majority of the Monte Carlo runs diverged, remained at the CRLB until approximately thirty minutes into the trajectory, where the filter error began to grow unbounded.

Changing the grade of INS to navigation (as in the TEN-NAV case) as opposed to tactical, we were able to achieve filter stability. The Monte Carlo simulation error for the north and east tilt error states for the TEN-NAV case are shown below.

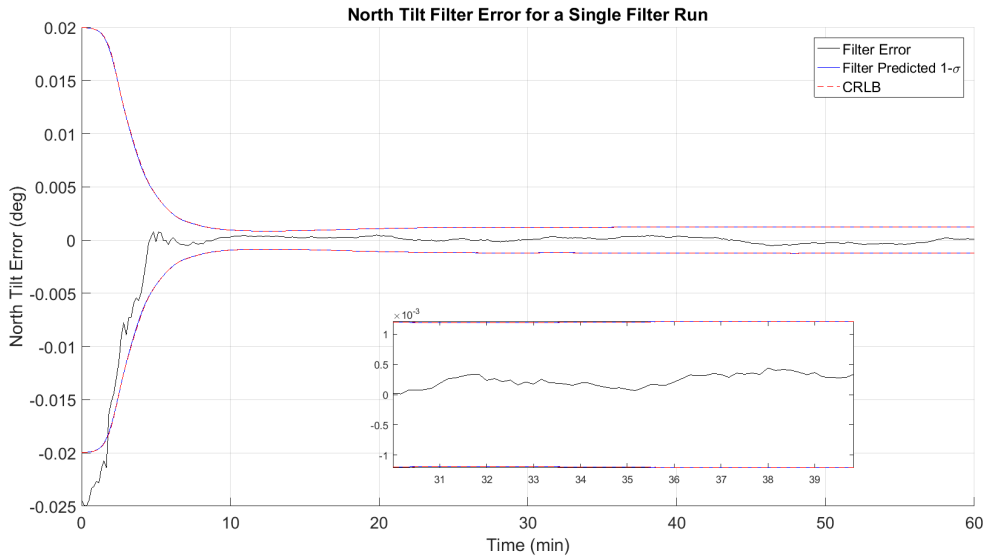

Figure 54. EKF Error in North Tilt Error States for the TEN-NAV Case

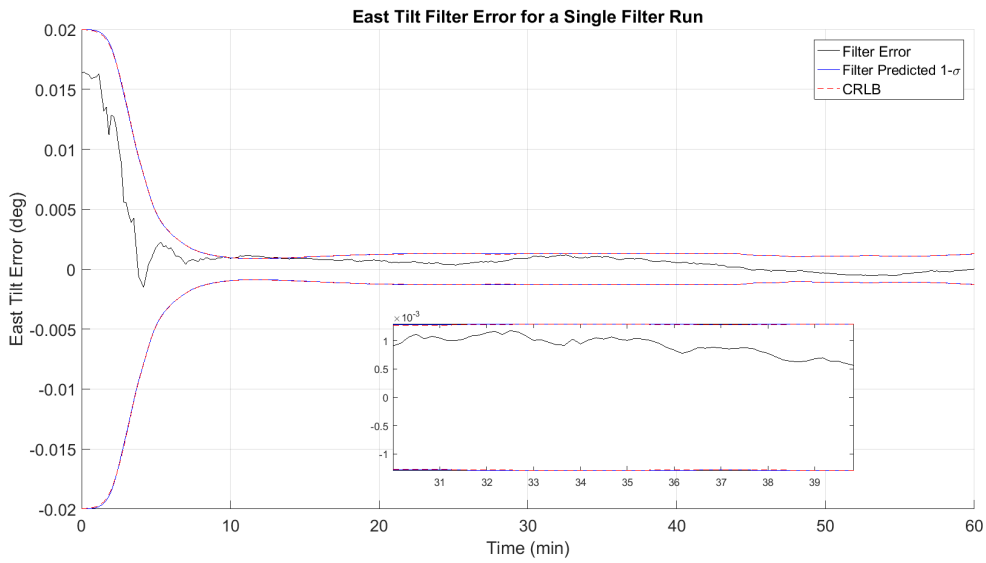

Figure 55. EKF Error in East Tilt Error States for the TEN-NAV Case

4.5 Continental Airplane Trajectory Results

The trajectory from cases 5 through 8 was moved over land as shown in Figure 12 for use in cases 9 through 12. Figure 56 shows the path of the airplane over the three vector component maps of the magnetic field. Examples of measurements generated at this location are shown in Figures 57 and 58. While the vector measurements are a steadily varying signal over the course of the trajectory, the tensor components show extreme variations for the first ten minutes of the trajectory and settle out for the remainder. As the airplane moved northwest as shown in Figure 56, it is clear where the high frequency content of the magnetic field drops down to low frequencies.

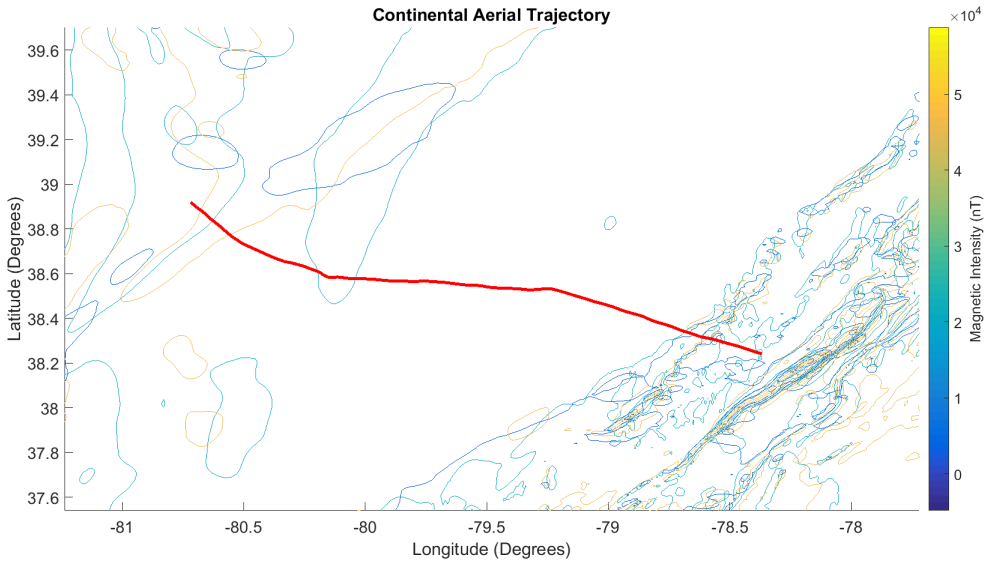

Figure 56. Airplane Trajectory Overlayed Onto Vector Field Maps

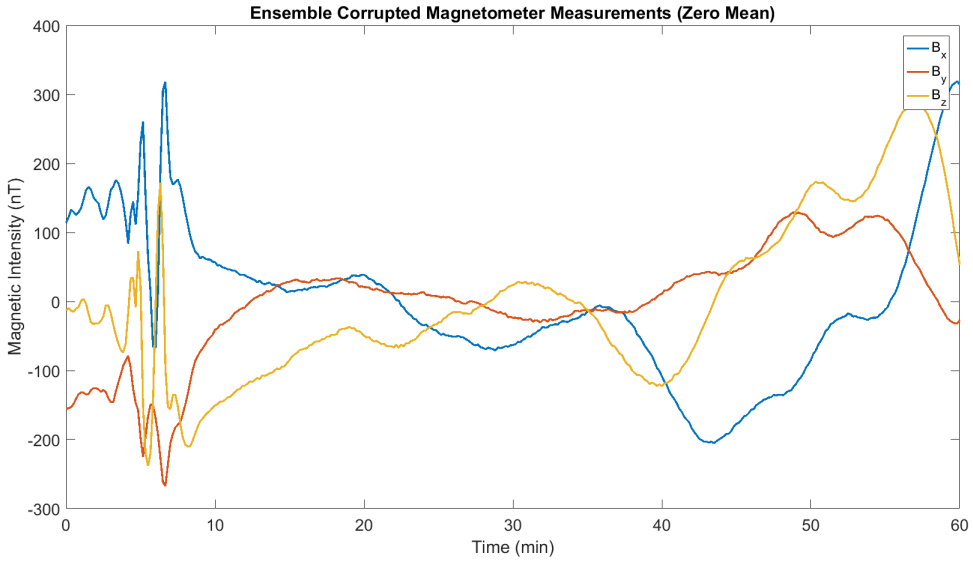

Figure 57. Corrupted World-Frame Vector Magnetometer Measurements for the VEC-TACT and VEC-NAV Cases

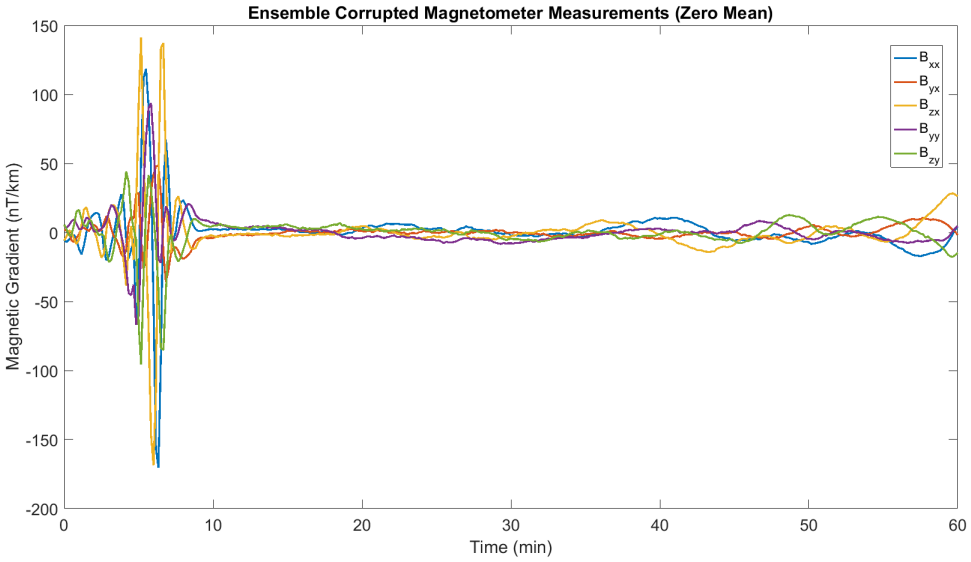

Figure 58. Corrupted World-Frame Magnetic Tensor Measurements for the TEN-TACT and TEN-NAV Cases

Table 9. DRMS Results for U.S. Continental Aerial Trajectory

Case	Measurement Type	INS Quality	DRMS Error	CRLB DRMS Error
9	Vector	Tact	514.53 m	549.13 m
10	Vector	Nav	141.17 m	182.7 m
11	Tensor	Tact	Filter Diverged	502.85 m
12	Tensor	Nav	205.95 m	136.24 m

Table 10. Filter Error in North and East Tilt Error States for U.S. Continental Aerial Trajectory

Case	North Tilt Filter Error	East Tilt Filter Error
VEC-TACT	0.12 deg	0.1 deg
VEC-NAV	8×10^{-4} deg	1.4×10^{-3} deg
TEN-TACT	Unstable	Unstable
TEN-NAV	8×10^{-4} deg	3×10^{-3} deg

The tensor measurement filter paired with a tactical-grade INS (the TEN-TACT case) remained as unstable as with previous trajectories. Looking closely at when the

filter diverges leads us to believe that the instability of the filter is compounded by the fact that the measurements remain fairly constant and unchanging after the ten minute mark.

Figure 59 shows the filter error for the horizontal position states during a single filter run of the TEN-TACT case as well as the filter predicted covariance. The filter predicted covariance becomes low (over-confident) during the time that the tensor measurements are reflecting the rich signal at ten minutes. The filter confidently locks onto an incorrect position solution at this point judging by the steadily increasing error and continuing overly-confident covariance.

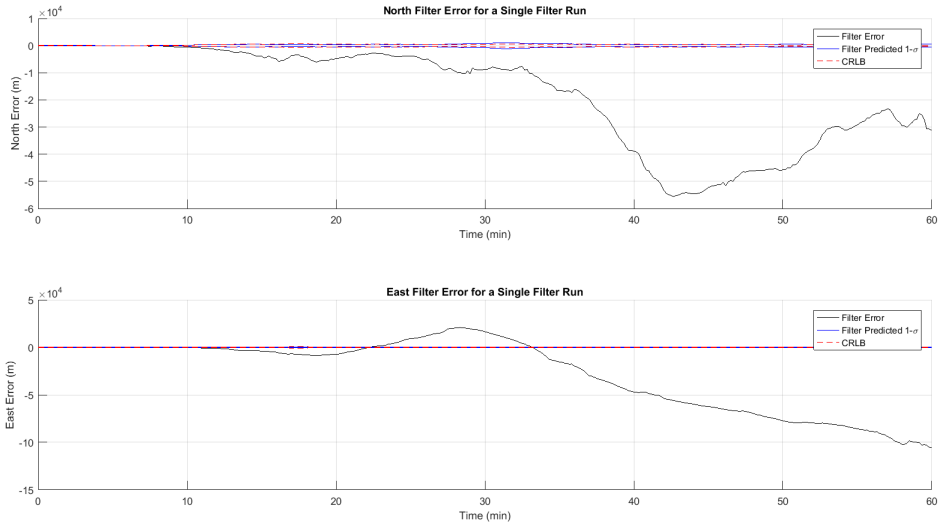

Figure 59. EKF Error in Horizontal Position States for a Single Run - TEN-TACT Case

When a navigation-grade INS was used in the TEN-NAV case, the position error decreased and the filter was relatively stable during the Monte Carlo simulation. The Monte Carlo error for the horizontal position states for the TEN-NAV case are shown in Figures 60 and 61.

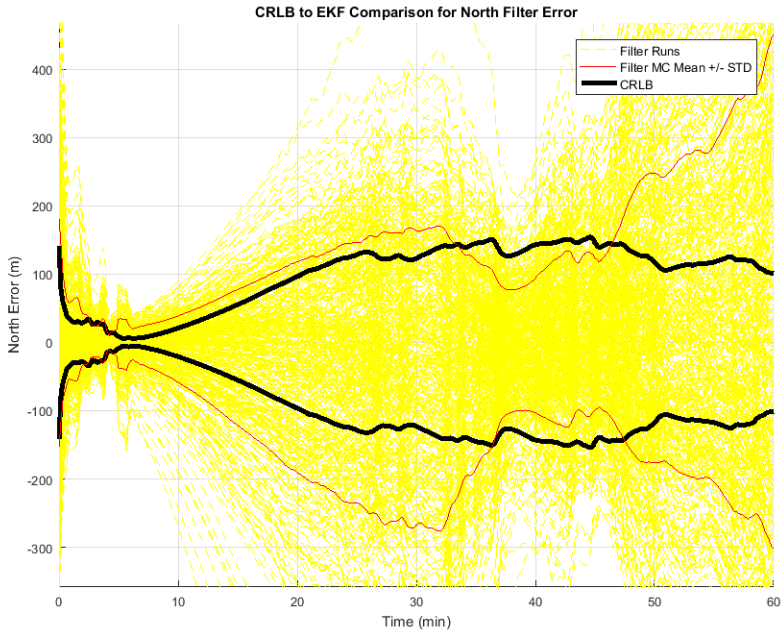

Figure 60. EKF Error in North Position State for the TEN-NAV Case

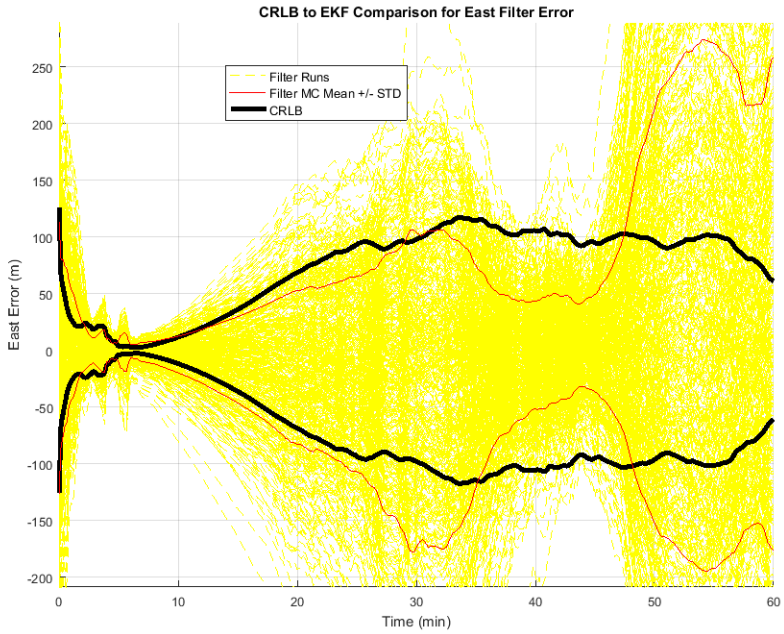

Figure 61. EKF Error in East Position State for the TEN-NAV Case

For a single run with a navigation-grade INS, the TEN-NAV filter had the same decrease in filter-predicted covariance right before ten minutes, but became less confident as the measurements became less rich. The filter did not lock onto the incorrect position solution because of its over-confidence as it did in the TEN-TACT case.

The behavior of the tilt error states in the TEN-TACT and TEN-NAV cases parallel the behavior of their position states. Figures 62 shows the filter error in the tilt error states and filter predicted covariance for a single run of the TEN-TACT case while Figures 63 through 65 show the filter error in the tilt error states for the TEN-NAV case. In the TEN-TACT case, the filter incorrectly locked on to a tilt error solution, whereas in the TEN-NAV case, the filter was able to clamp down on the correct north and east tilt error solution. For the down tilt error state, the filter estimate shifted while the measurements were rich and the filter was confident. The estimate stayed locked on to the same incorrect solution for the rest of the trajectory.

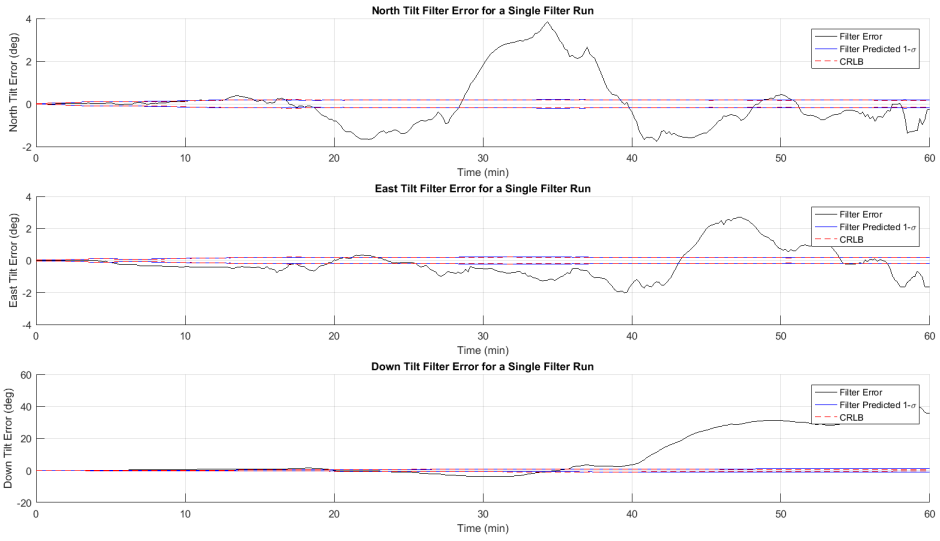

Figure 62. EKF Error in Tilt Error States for a Single Run - TEN-TACT Case

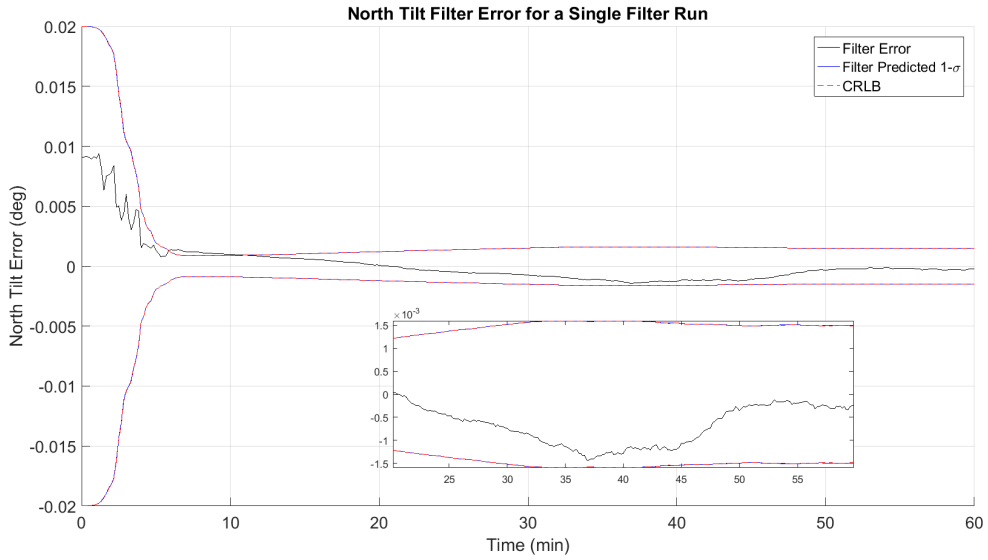

Figure 63. EKF Error in North Tilt Error States for a Single Run - TEN-NAV Case

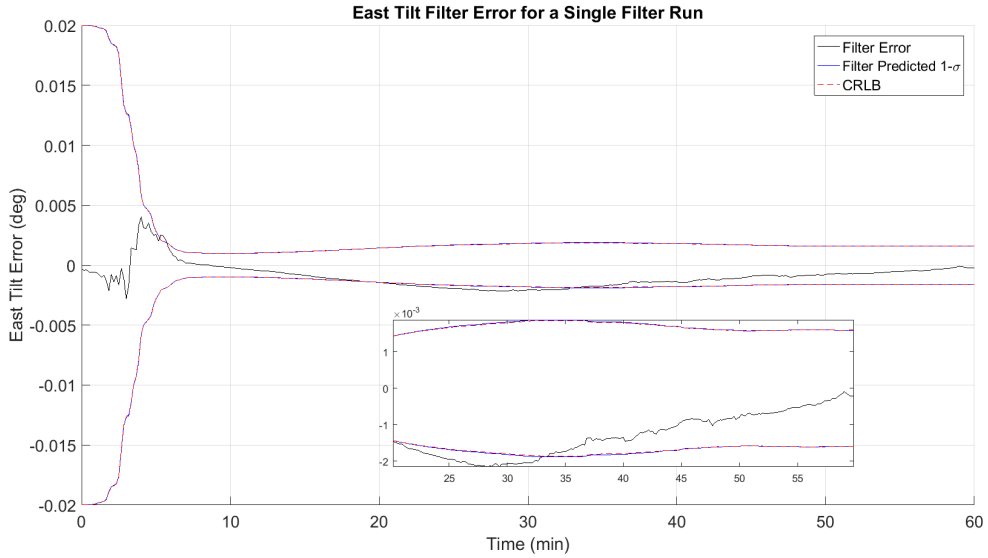

Figure 64. EKF Error in East Tilt Error States for a Single Run - TEN-NAV Case

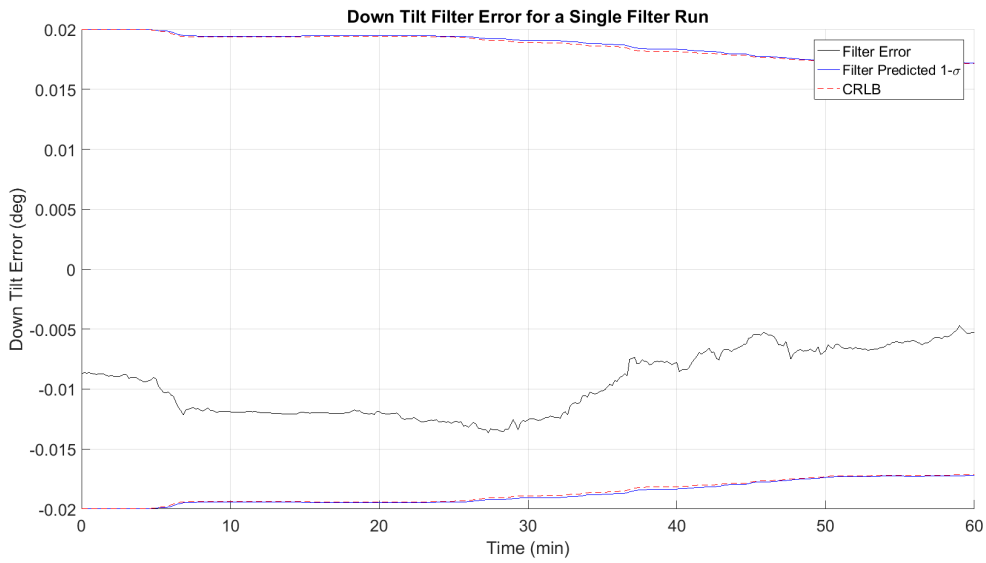

Figure 65. EKF Error in Down Tilt Error States for a Single Run - TEN-NAV Case

The VEC-TACT and VEC-NAV cases behaved similarly during the continental airplane trajectory as they did during the coastal airplane trajectory. The VEC-TACT filter during the continental airplane trajectory was relatively stable with only 4% of filter runs diverging, but was improved upon by pairing the filter with a navigation-grade INS. When the vector measurement filter was paired with the nav-grade INS in the VEC-NAV case, it was able to out-perform the tensor measurement filter the TEN-NAV case. The VEC-NAV case had a Monte Carlo simulation DRMS Error of 65.78 m less than the TEN-NAV case. This is most likely a result of the tensor measurements behavior around ten minutes. The Monte Carlo error for position states and tilt error states in the VEC-NAV case are shown in Figures 66 through 68.

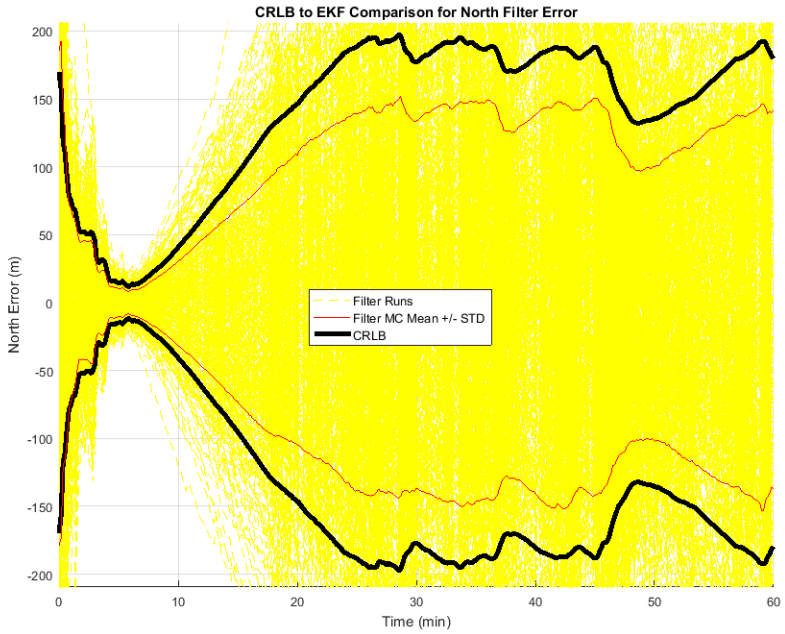

Figure 66. EKF Error in North Position State for the VEC-NAV Case

Figure 67. EKF Error in East Position State for the VEC-NAV Case

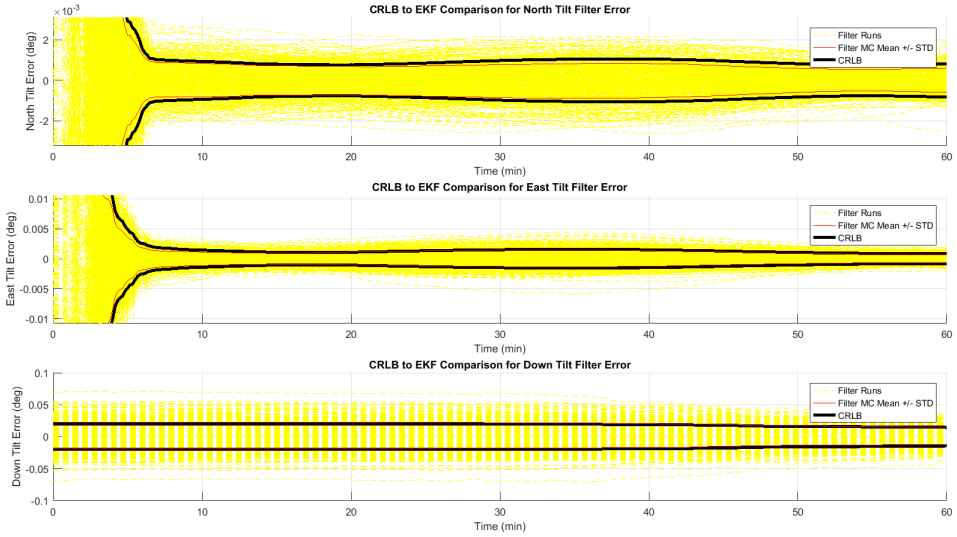

Figure 68. EKF Error in Tilt Error States for the VEC-NAV Case

4.6 Deep-Sea Boat Trajectory Results

The trajectory used in cases 13 and 14 was a 25 hour long boat trajectory in the same location as the coastal boat trajectory used in cases 1 through 4. The trajectory remained the same, but the maps used to navigate were altered to be more realistic for a location with an ocean-depth of 6000 m. A Fourier method was used to upward continue the anomaly map to an altitude of 6000 m. At this height, the frequency content of the map is much lower [5], and we expect to see a signal that is not as ideal for magnetic navigation. This high-altitude map was used to generate the vector and tensor maps via the Fourier method described previously.

For both cases (VEC-10X and TEN-10X), a 10X-grade INS was used. A military ship navigating for longer trajectories (such as the 25 hour trajectory used here) would likely have a high-quality INS on board, and we model a higher-quality INS with the 10X-grade INS as described in Table 3. This INS is modeled to have a position error of approximately 1 nmi after 24 hours [10].

Figure 69 shows the path of the ship over the three vector component maps of the magnetic field. An example of the corrupted vector and tensor measurements generated for this trajectory are shown in Figures 70 and 71 respectively. The measurements were corrupted with zero-mean White Gaussian noise with a covariance of 27 nT^2 for the vector case and 0.8 $\frac{\mathrm{nT}^2}{\mathrm{km}^2}$ for the tensor case. The noise strengths were chosen to triple the measurement error of all previous cases. Greater measurement noise is expected in these cases, given the possible effects of the deep ocean on the Earth's magnetic field at sea-level.

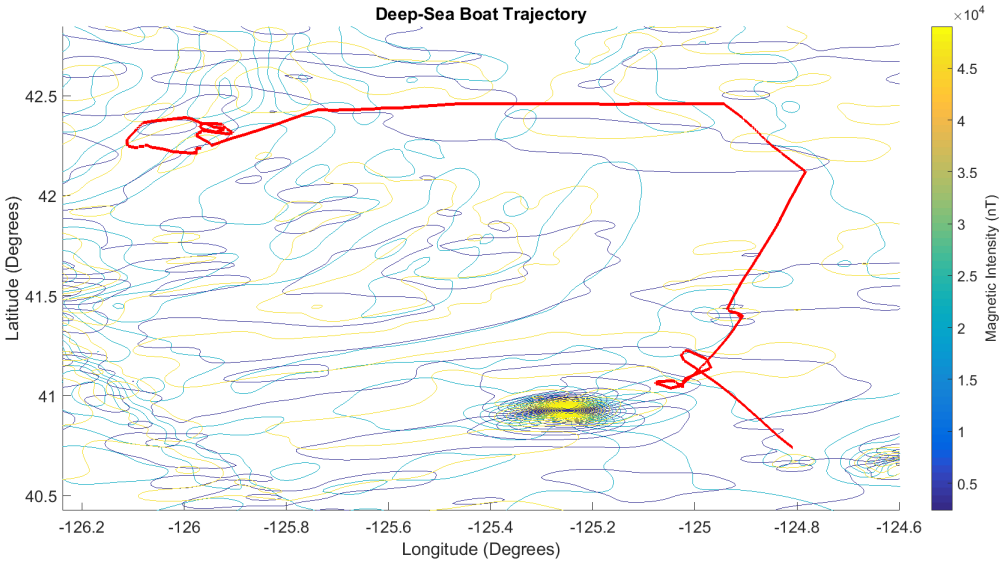

Figure 69. Boat Trajectory Overlayed Onto Vector Field Maps

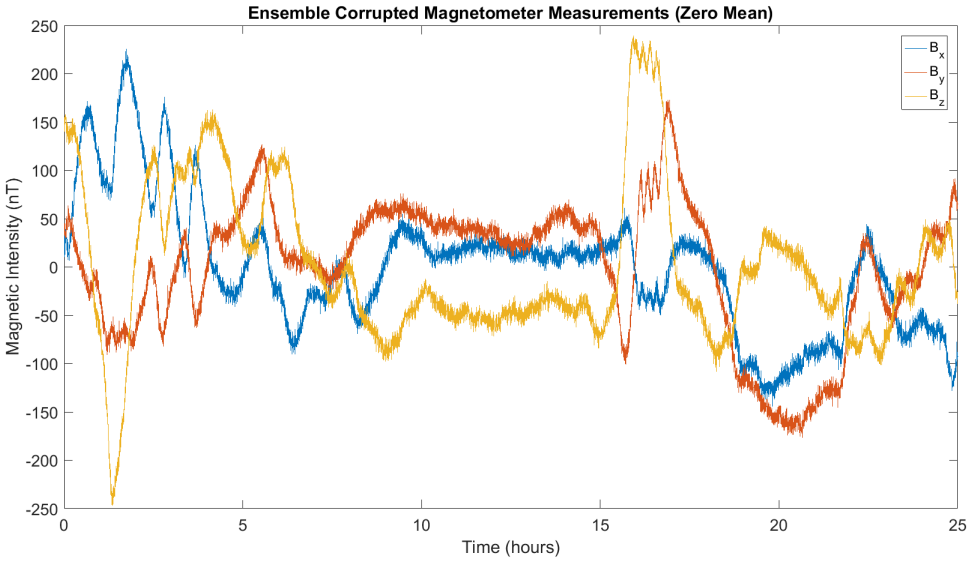

Figure 70. Corrupted World-Frame Vector Magnetometer Measurements for the VEC-10X Case

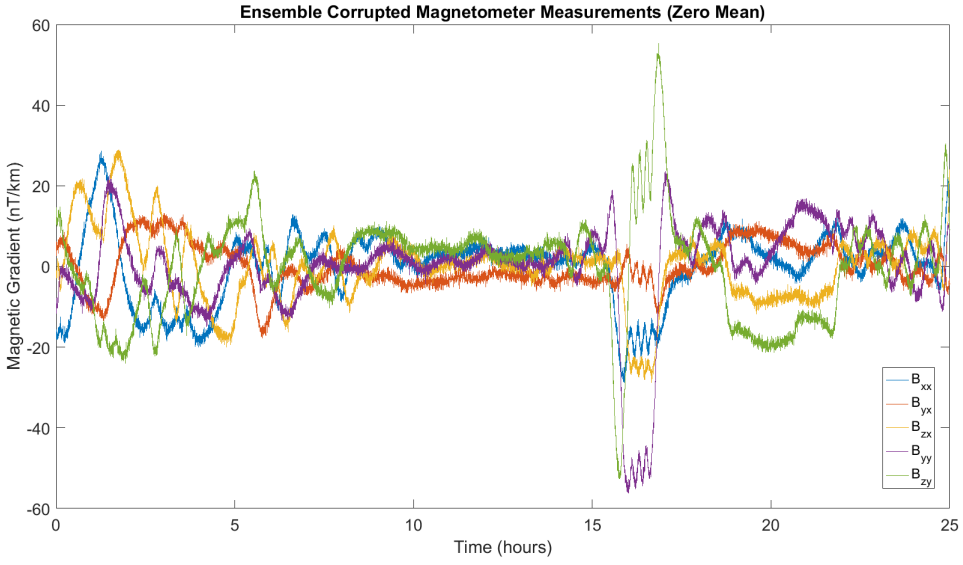

Figure 71. Corrupted World-Frame Magnetic Tensor Measurements for the TEN-10X Case

Table 11. DRMS Results for Deep-Sea Boat Trajectory

Case	Measurement Type	INS Quality	DRMS Error	CRLB DRMS Error
13	Vector	10X	194.90 m	249.23 m
14	Tensor	10X	185.52 m	169.21 m

Table 12. Filter Error in North and East Tilt Error States for Deep-Sea Boat Trajectory

Case	North Tilt Filter Error	East Tilt Filter Error
VEC-10X	2.6 $\times 10^{-4}$ deg	3 $\times 10^{-4}$ deg
TEN-10X	3.4 $\times 10^{-4}$ deg	4 $\times 10^{-4}$ deg

From Table 11, it is clear that both navigation systems were able to cut the drift of the INS down from the expected 1 nmi over the 25 hour trajectory to approximately 200 m. The TEN-10X case only had approximately 10 m less DRMS error than the VEC-10X case for the 500 run Monte Carlo simulation. The position error states for a single run of the TEN-10X case are shown below:

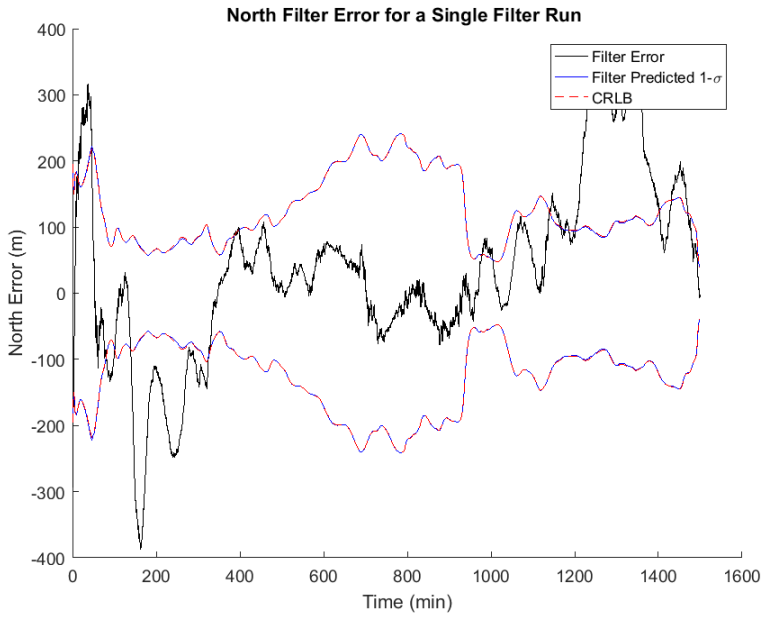

Figure 72. EKF Error in North Position State for a Single Run - TEN-10X Case

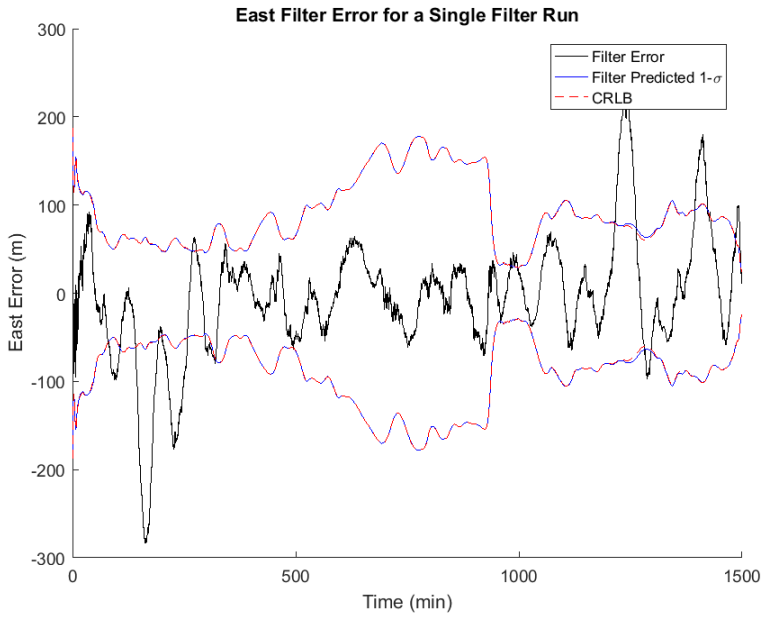

Figure 73. EKF Error in East Position State for a Single Run - TEN-10X Case

In both the VEC-10X and TEN-10X cases, the tilt error states remained minimal. Throughout the entire 25 hour trajectory, using these navigation systems, we would have an accurate attitude solution in addition to the relatively low DRMS errors. The error plots for the tilt error states in a single filter run of the TEN-10X case are shown in Figure 74 through 76. These plots show that the TEN-10X filter was able to retain an accurate orientation solution throughout the entire trajectory.

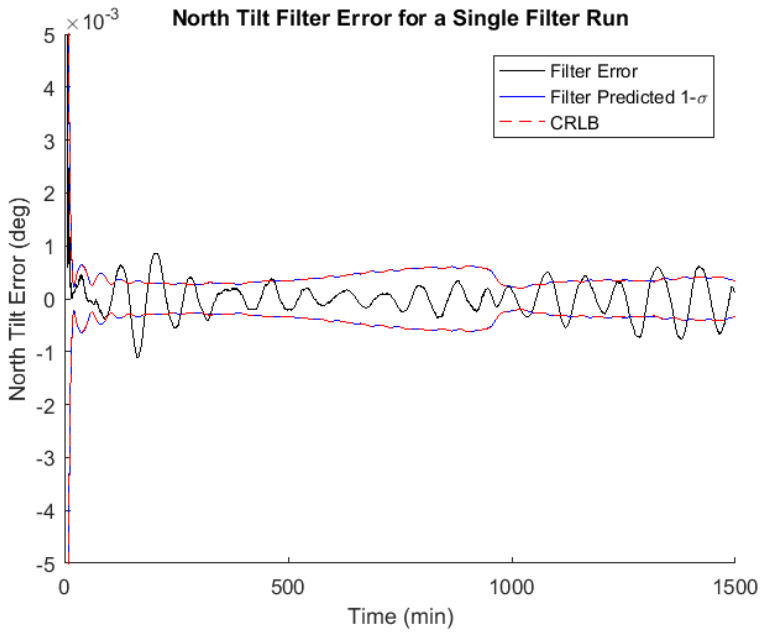

Figure 74. EKF Error in North Tilt Error State for the TEN-10X Case

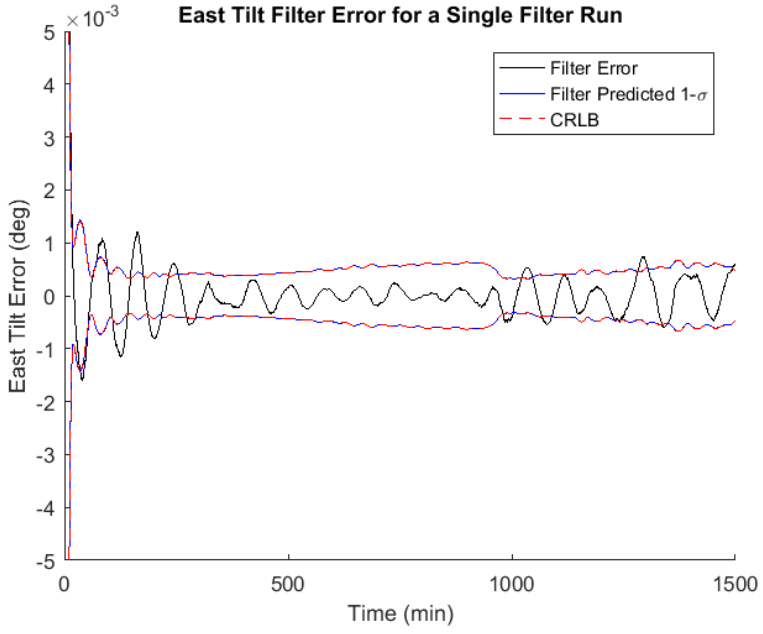

Figure 75. EKF Error in East Tilt Error State for the TEN-10X Case

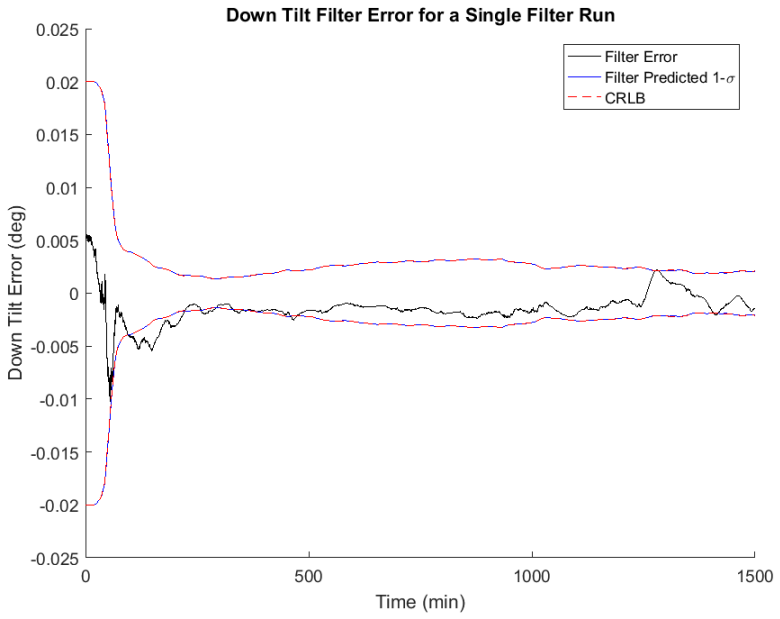

Figure 76. EKF Error in Down Tilt Error State for the TEN-10X Case

4.7 Boat Trajectory Results Using a Global Model

The 25-hour boat trajectory was also used for cases 15 and 16. With the deep-sea boat trajectory above, the navigation systems were paired with simulated lower-frequency maps and were still able to perform. For the next two cases, the VEC-10X and TEN-10X navigation systems were paired with maps generated from the global EMM model. The trajectory used in these cases was shifted over an area of the continental United States to match the EMM map data available at the time of the simulation. These cases demonstrated the navigation accuracies possible for both the VEC-10X and TEN-10X navigation systems paired with low-frequency global model maps.

Figure 77 shows the path of the ship over the three vector component maps of the magnetic field. Examples of corrupted vector and tensor measurements generated for the 25-hour boat trajectory using the global model maps are shown in Figures 78

and 79 respectively. The measurements for these two cases were also corrupted with white Gaussian noise with a covariance of 27 nT^2 for the vector case and 0.8 $\frac{\text{nT}^2}{\text{km}^2}$ for the tensor case.

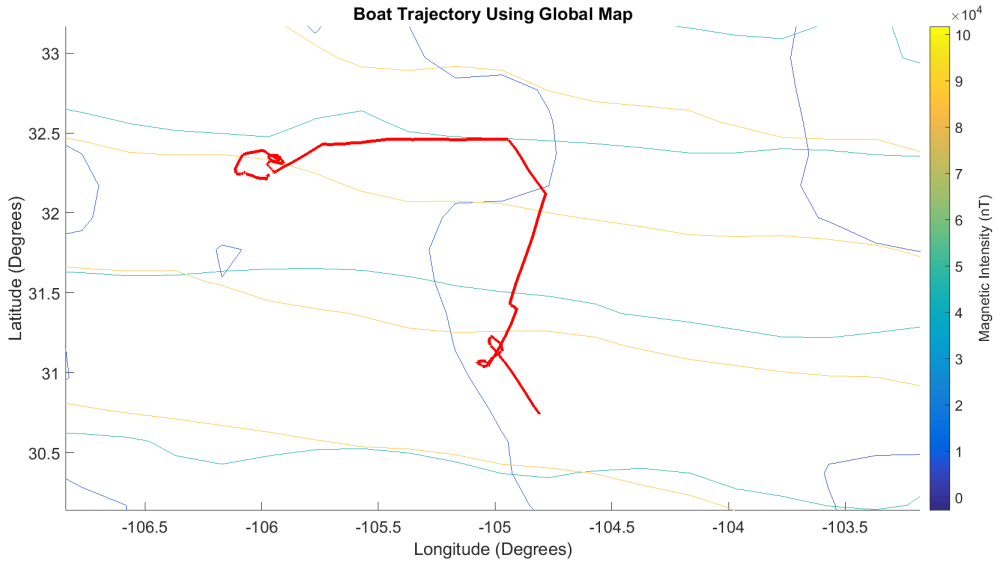

Figure 77. Boat Trajectory Overlayed Onto Vector Field Maps

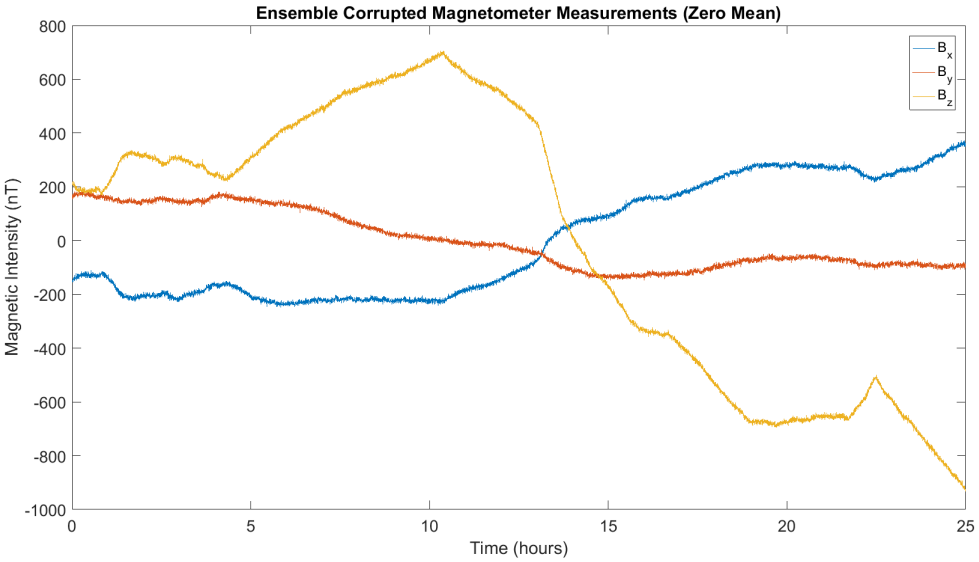

Figure 78. Corrupted World-Frame Vector Magnetometer Measurements for the VEC-10X Case

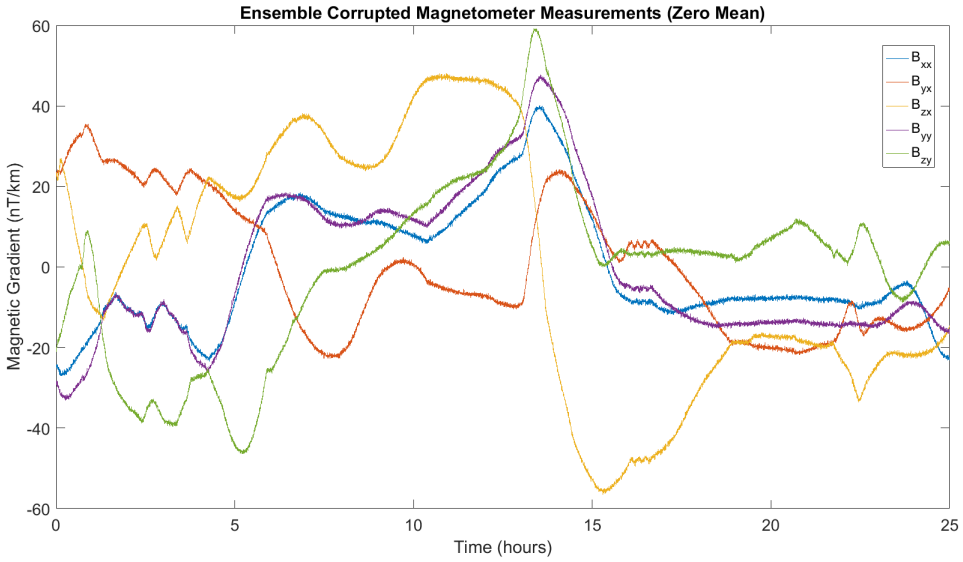

Figure 79. Corrupted World-Frame Magnetic Tensor Measurements for the TEN-10X Case

Table 13. DRMS Results for Boat Trajectory Using a Global Model

Case	Measurement Type	INS Quality	DRMS Error	CRLB DRMS Error
15	Vector	10X	219.28 m	275.9 m
16	Tensor	10X	38.10 m	94.98 m

Table 14. Filter Error in North and East Tilt Error States for Boat Trajectory Using a Global Model

Case	North Tilt Filter Error	East Tilt Filter Error
VEC-10X	4×10^{-4} deg	5×10^{-4} deg
TEN-10X	8.8×10^{-5} deg	2×10^{-4} deg

From Tables 13 and 14, it is clear that both navigation systems improved upon the expected unaided drift of the INS. The TEN-10X filter was able to achieve navigation accuracies of 38 m using the global map and steady state tilt errors down to 8.8×10^{-5} degrees. Figures 80 and 81 below show the north and east filter error for a single run using the TEN-10X navigation system.

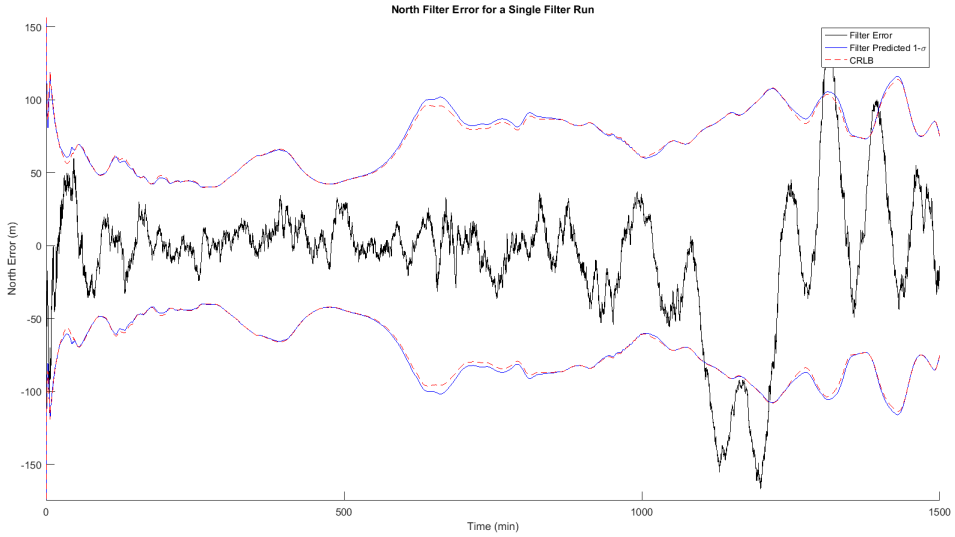

Figure 80. EKF Error in North Position State for the TEN-10X Case

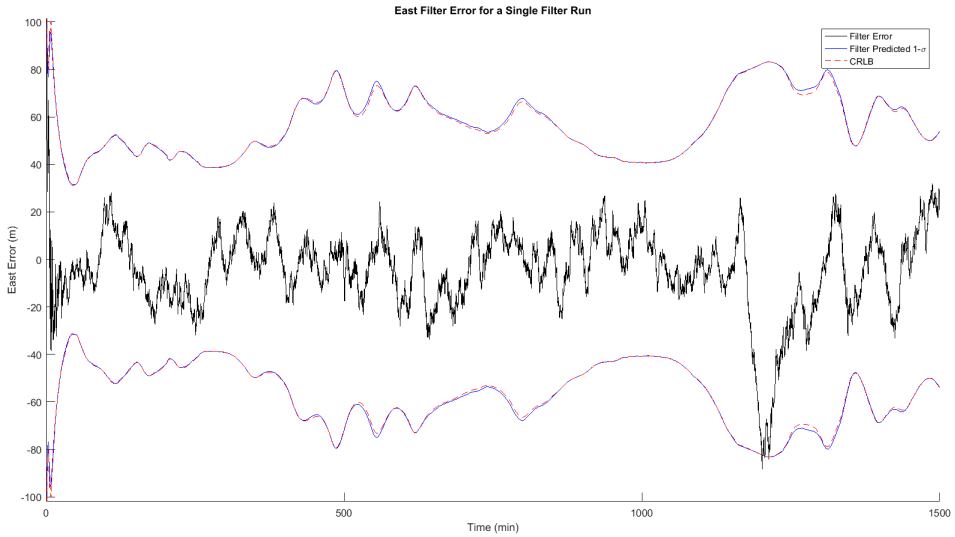

Figure 81. EKF Error in East Position State for the TEN-10X Case

The error in the north and east tilt error states for this same filter run are shown below in Figures 82 and 83.

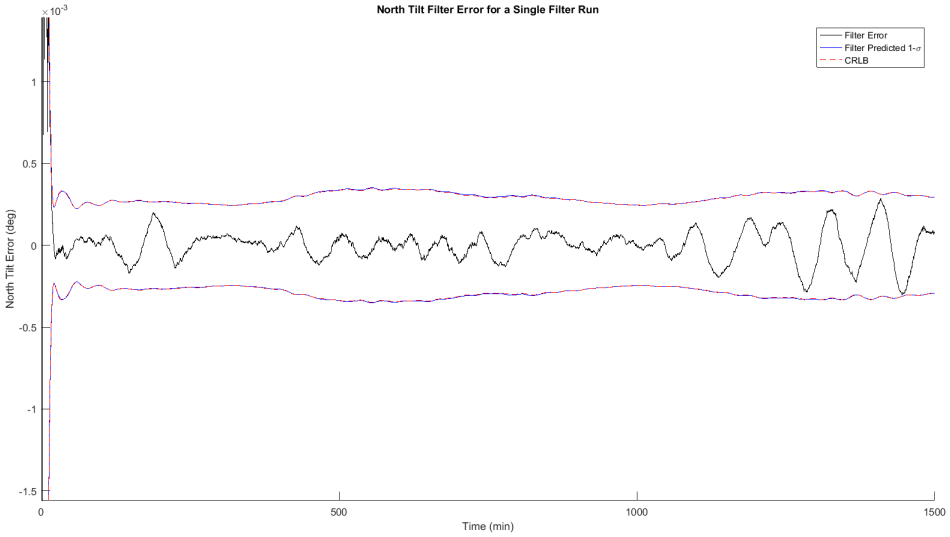

Figure 82. EKF Error in North Tilt Error State for the TEN-10X Case

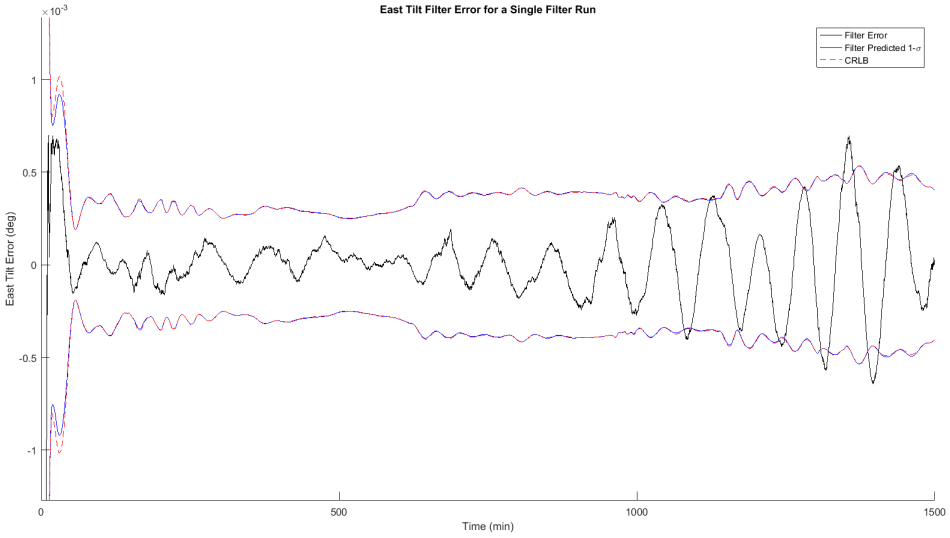

Figure 83. EKF Error in East Tilt Error State for the TEN-10X Case

These are promising results given the global availability of the EMM-720 model. These cases demonstrate that we are able to navigate anywhere around the globe using the navigation systems presented in this research paired with low-resolution

global model maps. When the VEC-10X and TEN-10X navigation systems are used in simulation, we are not limited by the low resolution of the available global model.

4.8 DRMS Error for all Cases

Table 15 lists the Monte Carlo simulation DRMS error for each case. It reflects the results presented above, but allows for comparison between the navigation system results for different trajectories.

Table 15. DRMS Error Results for all Simulation Cases

Case	Trajectory	Meas Type	INS Quality	DRMS Error
1	Coastal Boat	Vector	Tactical	420.54 m
2	Coastal Boat	Vector	Navigation	185.00 m
3	Coastal Boat	Tensor	Tactical	755.48 m
4	Coastal Boat	Tensor	Navigation	35.94 m
5	Coastal Aerial	Vector	Tactical	254.96 m
6	Coastal Aerial	Vector	Navigation	103.43 m
7	Coastal Aerial	Tensor	Tactical	Filter Diverged
8	Coastal Aerial	Tensor	Navigation	61.07 m
9	Continental Aerial	Vector	Tactical	514.53 m
10	Continental Aerial	Vector	Navigation	141.17 m
11	Continental Aerial	Tensor	Tactical	Filter Diverged
12	Continental Aerial	Tensor	Navigation	205.95 m
13	Deep-Sea Boat	Vector	10X	194.90 m
14	Deep-Sea Boat	Tensor	10X	185.52 m
15	Global Model Boat	Vector	10X	219.28 m
16	Global Model Boat	Tensor	10X	38.10 m

V. Conclusion

Through simulation, this research was able to prove the viability of using vector or tensor measurements of the magnetic anomaly field in a navigation system as an alternative to GPS navigation. Several variables were evaluated in the sixteen simulation cases and findings for these are listed below.

Trajectory Position and Velocity.

The velocity of the trajectory did not have a great affect on filter performance during simulations. This may be due to the fact that more signals are being brought into filter with vector and tensor measurements, so despite the measurements coming in more slowly, the higher number of signals allows the filter to accurately resolve a position and attitude solution. The navigation system was able to obtain navigation accuracies of 35.94 m over a one hour low-velocity boat trajectory and 61.07 m over a one hour high-velocity aerial trajectory.

Measurement Types.

The simulations demonstrate that navigation accuracy increases with an increasing number of measurements coming into the filter. As long as the filter was paired with a nav-grade INS, the navigation filter when using tensor measurements was able to achieve the lowest DRMS error (specifically in the coastal boat TEN-NAV case) and was able to consistently perform better than when using vector measurements. These are promising results, because the use of tensor measurements essentially cancels out the effects of temporal variations in the measurements, which in turn reduces measurement errors in the navigation system. The ability to minimize measurement errors in a navigation system is critical to minimizing error in the position and attitude solutions.

The best case tensor filter results only occurred in combination with a navigation-grade INS. The tensor measurement filter was unstable in combination with a tactical-grade INS. Removing the temporal variation states from the model may actually have negatively impacted the filter. The filter was not expecting any bias errors because of the removal of these states; However, there may have been bias errors in the measurements due to other effects. This led to overconfidence in the filter estimates and in turn, filter divergence.

INS Quality.

The quality of INS used in simulations had a large impact on the overall filter performance. Generally, pairing the filters with a tactical-grade INS resulted in divergent runs. The filter performed best when paired with a navigation or 10X-grade INS. When paired with the 10X-grade INS, the navigation system was able to obtain navigation accuracies of 185 m DRMS over a 25 hour trajectory. This specific trajectory was over the deep ocean and used a map with lower frequency content. The TEN-10X filter was also able to obtain navigation accuracies of 38.10 m when paired with EMM global maps, which are of even lower frequency than the deep-sea NAMAD maps. We would expect the lack of signal in the map as well as lack of signal due to the low velocity of the ship to cause problems for the filter. The combination of the 10X-grade INS and the tensor measurements within the navigation system was able to overcome this challenge.

Map Resolution.

The simulations demonstrated that both navigation systems were able to perform with lower-resolution global maps from the EMM. When using either navigation system presented in this research, high navigation accuracy was not limited to navigation

using high resolution maps such as the NAMAD. For military applications, the results of this research open up the possibility of using magnetic navigation as an alternative to GPS navigation in any area of operations around the globe to estimate vehicle position and orientation accurately.

Future Work.

One aspect to consider for future work following this thesis, is running simulations on the navigation system with an alternate dynamics model. The EKF could possibly be improved when paired with the tactical grade INS and tensor measurements by introducing the error bias states back into the dynamics model. While the temporal variations are nearly canceled out in the tensor measurements, there could be more error from the effects of the vehicle than is modeled. More accurately modeling this error could improve filter performance, as the filter would place a more accurate amount of confidence in the measurements as opposed to the over-confidence that was displayed.

Another option for dealing with this filter instability would be to re-design the filter to use an MPF as opposed to the EKF to better deal with the non-linearity of the measurement function. This would require a large amount of processing power given the computational intensity of dealing with the particles, but also computing the measurement Jacobian for each particle at each time step. This filter would be expected to have the highest accuracy if effort is put forth into minimizing processing requirements.

Another consideration for future work following this thesis would be to move from simulation to real trials to assess the navigation system performance. While the trajectories used in the simulations were realistic, the performance of the navigation system using real measurements, maps, and trajectories could vary greatly depending

on the true accuracy of the measurements and maps. Vector magnetometers are a mature technology, however, they have not been widely used to conduct surveys and gather accurate vector magnetic anomaly maps. As these vector maps are not readily available, effort would go into obtaining accurate vector maps for the area traversed during real vehicle tests. The same is true for tensor maps however, the tensor measurement configuration is not as mature as the vector magnetometer and would require extensive calibration to ensure accurate tensor measurements. Once calibration is acceptable, the focus would be on collecting data to generate small tensor map tiles for real vehicle tests. Running trials with accurate maps and true measurements is the next step to determining if vector or tensor magnetic anomaly field measurements are a promising option as a GPS signal alternative.

Bibliography

1. Viki Bankey, Alejandro Cuevas, David Daniels, Carol A Finn, Israel Hernandez, Patricia Hill, Robert Kucks, Warner Miles, Mark Piulkington, Carter Roberts, and et al. `https://crustal.usgs.gov/projects/namad/#NAMAP`. Accessed: 2018-02-26.

2. Bartington Instruments. *Grad-13 Digital Three-Axis Gradiometer.*

3. Bartington Instruments. *Mag-03 Three-Axis Magnetic Field Sensors.*

4. Niclas Bergman. *On the Cramer-Rao bound for terrain-aided navigation.* Linköping University Electronic Press, 1997.

5. R.J. Blakely. *Potential Theory in Gravity and Magnetic Applications.* Stanford-Cambridge program. Cambridge University Press, 1996.

6. R.G. Brown and P.Y.C. Hwang. *Introduction to random signals and applied Kalman filtering.* Number v. 1. J. Wiley, 1992.

7. Aaron Canciani. *Absolute Positioning Using the Earth's Magnetic Anomoly Field.* PhD thesis, Air Force Institute of Technology, 2016.

8. E. Dorveaux, D. Vissiere, and N. Petit. On-the-field calibration of an array of sensors. *American Control Conference (ACC), 2010*, 2010.

9. Eric Dorveaux, David Vissière, Alain Pierre Martin, and Nicolas Petit. Iterative calibration method for inertial and magnetic sensors. *Proceedings of the IEEE Conference on Decision and Control*, pages 8296–8303, 2009.

10. Kenneth Gade. *Introduction to Inertial Navigation.* Norwegian Defense Research Establishment, 2005.

11. Geometrics. *G-822a Cesium Magnetometer*, 2005.

12. William J. Hinze, Ralph R. B. von Frese, R. Von Frese, and Afif H. Saad. *Gravity and Magnetic Exploration: Principles, Practices, and Applications*. Cambridge University Press, 2013.

13. Yu Huang, Lihua Wu, and Dequan Li. Theoretical Research on Full Attitude Determination Using Geomagnetic Gradient Tensor. *Journal of Navigation*, 68(05):951–961, 2015.

14. Daesung Jeon, Hoimyung Choi, and Jaehwan Kim. UKF data fusion of odometry and magnetic sensor for a precise indoor localization system of an autonomous vehicle. *2016 13th International Conference on Ubiquitous Robots and Ambient Intelligence, URAI 2016*, pages 47–52, 2016.

15. Tobias Karlsson. Terrain Aided Underwater Navigation using Bayesian Statistics. *Electrical Engineering*, 2002.

16. Naomi Kato and Toshihide Shigetomi. Underwater Navigation for Long-Range Autonomous Underwater Vehicles Using Geomagnetic and Bathymetric Information. *Advanced Robotics*, 23(7-8):787–803, 2009.

17. Shane T. Keenan, Dave Clark, Klye R. Blay, Keith Leslie, Cathy P. Foley, and Stephen Billings. Calibration and testing of a HTS tensor gradiometer for underwater UXO detection. *2011 International Conference on Applied Superconductivity and Electromagnetic Devices, ASEMD 2011*, pages 135–137, 2011.

18. Eunghyun Kim Eunghyun Kim and Hyo-Choong Bang Hyo-Choong Bang. Bias estimation of magnetometer using genetic algorithm. *2007 International Conference on Control, Automation and Systems*, 2007.

19. Kok-meng Lee and Min Li. Magnetic Tensor Sensor for Gradient-Based Localization of Ferrous Object in Geomagnetic Field. 52(8), 2016.

20. Kok Meng Lee, Min Li, and Chun Yeon Lin. Magnetic Tensor Sensor and Way-Finding Method Based on Geomagnetic Field Effects With Applications for Visually Impaired Users. *IEEE/ASME Transactions on Mechatronics*, 21(6):2694–2704, 2016.

21. Kok-Meng Lee, Min Li, and Chun-Yeon Lin. Magnetic Tensor Sensor and Way-Finding Method Based on Geomagnetic Field Effects With Applications for Visually Impaired Users. *IEEE/ASME Transactions on Mechatronics*, 21(6):2694–2704, 2016.

22. Zhongyan Liu, Hongfeng Pang, Mengchun Pan, and Chengbiao Wan. Calibration and Compensation of Geomagnetic Vector Measurement System and Improvement of Magnetic Anomaly Detection. *IEEE Geoscience and Remote Sensing Letters*, 13(3):447–451, 2016.

23. Steven Macintyre. Magnetic Field Measurement. In *The Measurement, Instrumentation and Sensors Handbook on CD-ROM*. 1999.

24. P.S. Maybeck. *Stochastic Models, Estimation and Control:*. Number v. 2 in Mathematics in Science and Engineering. Academic Press, 1982.

25. Ronald T. Merrill, M.W. McElhinny, and P.L. McFadden. *The Magnetic Field of the Earth: Paleomagnetism, the Core, and the Deep Mantle*. International geophysics series. Academic Press, 1998.

26. Marc Munschy and Simon Fleury. Scalar, vector, tensor magnetic anomalies: Measurement or computation? *Geophysical Prospecting*, 59(6):1035–1045, 2011.

27. Aboelmagd Noureldin, Tashfeen B. Karamat, and Jacques Georgy. *Fundamentals of inertial navigation, satellite-based positioning and their integration*. Springer-Verlag, 2013.

28. NovAtel. *GPS Position Accuracy Measures*, 2003.

29. National Oceanic and Atmospheric Administration. `https://www.ngdc.noaa.gov/geomag/EMM/`. Accessed: 2018-02-26.

30. Hong Feng Pang, Shi Tu Luo, Meng Chun Pan, Di Xiang Chen, Fei Lu Luo, and Qi Zhang. Bias and linearity measurement of three axis fluxgate magnetometers using high precise electromagnetic devices. In *2011 International Conference on Applied Superconductivity and Electromagnetic Devices, ASEMD 2011*, 2011.

31. Colin Reeves. Aeromagnetic Surveys. Principles, Practice & Interpretation. *Earthworks*, 2006.

32. Bagus Adiwiluhung Riwanto, Tuomas Tikka, Antti Kestila, and Jaan Praks. Particle Swarm Optimization with Rotation Axis Fitting for Magnetometer Calibration. *IEEE Transactions on Aerospace and Electronic Systems*, 2017.

33. M. Schneider, R. Stolz, S. Linzen, M. Schiffler, A. Chwala, M. Schulz, S. Dunkel, and H. G. Meyer. Inversion of geo-magnetic full-tensor gradiometer data. *Journal of Applied Geophysics*, 92:57–67, 2013.

34. Thomas Schön, Fredrik Gustafsson, and Per-Johan Nordlund. Marginalized Particle Filters for Mixed Linear / Nonlinear State-Space Models. *IEEE Transactions on Signal Processing*, 53(7):2279–2289, 2005.

35. Jason D Searcy and Henry J Pernicka. Magnetometer-Only Attitude Determination Using Novel Two-Step Kalman Filter Approach. *Journal of Guidance, Control, and Dynamics*, 35(6):1693–1701, 2012.

36. Jeremiah A. Shockley. *Ground Vehicle Navigation Using Magnetic Field Variation*. PhD thesis, Air Force Institute of Technology, 2012.

37. Maarten Speekenbrink. A tutorial on particle filters. *Journal of Mathematical Psychology*, 73:140–152, 2016.

38. William Storms, Jeremiah Shockley, and John Raquet. Magnetic field navigation in an indoor environment. In *2010 Ubiquitous Positioning Indoor Navigation and Location Based Service, UPINLBS 2010*, 2010.

39. D. Titterton and J.L. Weston. *Strapdown Inertial Navigation Technology*. Electromagnetics and Radar Series. Institution of Engineering and Technology, 2004.

40. David Vissière, Alain Martin, and Nicolas Petit. Using distributed magnetometers to increase IMU-based velocity estimation into perturbed area. *Proceedings of the IEEE Conference on Decision and Control*, pages 4924–4931, 2007.

41. JM Wilson, RJ Kline-Schoder, Marc A. Kenton, Paul H. Sorensen, and Odile H. Clavier. Passive navigation using local magnetic field variations. *2006 National Technical Meeting of The Institute of Navigation*, (January):770–779, 2006.

REPORT DOCUMENTATION PAGE

Form Approved
OMB No. 0704–0188

1. REPORT DATE *(DD–MM–YYYY)*	2. REPORT TYPE	3. DATES COVERED *(From — To)*
22–03–2018	Master's Thesis	Sept 2016 — Mar 2018

4. TITLE AND SUBTITLE

Navigation Using Vector and Tensor Measurements of the Earth's Magnetic Anomaly Field

5a. CONTRACT NUMBER

5b. GRANT NUMBER

5c. PROGRAM ELEMENT NUMBER

6. AUTHOR(S)

Mount, Lauren, A, Capt, USAF

5d. PROJECT NUMBER

17G125

5e. TASK NUMBER

5f. WORK UNIT NUMBER

7. PERFORMING ORGANIZATION NAME(S) AND ADDRESS(ES)

Air Force Institute of Technology
Graduate School of Engineering and Management (AFIT/EN)
2950 Hobson Way
WPAFB OH 45433-7765

8. PERFORMING ORGANIZATION REPORT NUMBER

AFIT-ENG-MS-18-M-049

9. SPONSORING / MONITORING AGENCY NAME(S) AND ADDRESS(ES)

Dr. Richard Willis
Office of Naval Research
875 N. Randolph Street, Suite 1425
Arlington, VA 22203
COMM 703-696-4214
richard.t.willis@navy.mil

10. SPONSOR/MONITOR'S ACRONYM(S)

ONR

11. SPONSOR/MONITOR'S REPORT NUMBER(S)

12. DISTRIBUTION / AVAILABILITY STATEMENT

DISTRIBUTION STATEMENT A:
APPROVED FOR PUBLIC RELEASE; DISTRIBUTION UNLIMITED.

13. SUPPLEMENTARY NOTES

This work is declared a work of the U.S. Government and is not subject to copyright protection in the United States

14. ABSTRACT

As a means to navigate in a GPS-denied environment, a navigation filter is presented that uses measurements of Earth's magnetic anomaly field to aid an inertial navigation system (INS). An Extended Kalman Filter (EKF) is used to match magnetometer measurements to a specific location on magnetic field maps. A simulation trade-study is presented to highlight the advantages of using vector or tensor measurements of the anomaly field to aid the filter as opposed to other signals, such as scalar measurements of the anomaly field.

15. SUBJECT TERMS

Magnetic Anomaly, Navigation, Alternative Navigation, GPS-Denied, Magnetic Fields

16. SECURITY CLASSIFICATION OF:			17. LIMITATION OF ABSTRACT	18. NUMBER OF PAGES	19a. NAME OF RESPONSIBLE PERSON
a. REPORT	b. ABSTRACT	c. THIS PAGE			Captain Aaron J. Canciani, AFIT/ENG
U	U	U	UU	129	19b. TELEPHONE NUMBER *(include area code)* (937) 255-3636, x4618; aaron.canciani.1@afit.edu